THE PHYSICAL SOCIETY

MEMOIRS

OF THE

COLLEGE OF SCIENCE

UNIVERSITY OF KYOTO

SERIES A

VOL. XXIX, No. 1

September, 1958

KYOTO

Digitized by the Internet Archive
in 2024

https://archive.org/details/memoirs-faculty-science-kyoto-phys-astro-geophys-chem_1958-09_29_1

1127 hm

Memoirs of the College of Science, University of Kyoto, Series A,
Vol. XXIX, No. 1, Article 1, 1958.

ON THE PERIODS OF SEISMIC WAVES OBSERVED IN LOCAL EARTHQUAKES

BY

Takeshi MIKUMO

(Received March 20, 1958)

ABSTRACT

The periods of body waves in local earthquakes as observed in Wakayama District were studied.

The periods of impulsive initial waves increase with an increase of travel-distance, but are not related to earthquake magnitude and other effects, within the range of our observation. The increasing rate of the period of the *P*-waves is more rapid than that of the *S*-waves. The reason for this was discussed.

The average periods of the *P*- and *S*-wave groups have a certain fixed value in every station, irrespective of focal distance, shock-magnitude, etc.. They may be attributed to free oscillations of superficial layer.

1. Introduction

The periods of the seismic waves observed at any station are presumably related to the conditions of the earthquake's origin, of the path of wave propagation, and of the observation points: that is, firstly, the emission mechanism of elastic waves at the focus, the earthquake magnitude or the dimension of focal region and the crustal structure near the origin; secondly, the nature of the medium, the structure of the crust and the focal distance, travelled by the earthquake-waves; and thirdly, the underground structure in the vicinity of the observation stations and the frequency response of the seismometer used. Because of these various factors the recorded seismograms should be complicated.

According to many investigations hitherto made, it is generally accepted that the seismic wave periods tend to increase with the increasing travel-distance and an increase in the magnitude of the earthquake, and that the predominant periods depend upon the thickness of the superficial layer near the station.

In 1954 and 1956, precise seismometric observations were carried out in the epicentral area of local shocks in Wakayama District for the purpose of studying the nature of micro-earthquakes (**1**). In this paper the relationship between the seismic wave periods, especially of body waves, obtained from the recorded seismograms in these observations, and the various factors mentioned in the following will be discussed: firstly, the focal distance; secondly, the earthquake magnitude, and thirdly, azimuthal distribution, and so forth.

2. Seismograms

The data used in the present analysis were 200 seismograms of 92 local earthquakes recorded at six stations; Idakiso, Wakanoura, Fuyuno, Nokami, Kainan and Yoro. All of these stations are situated in a metamorphic rock zone. Their positions were shown in the previous paper (**1**).

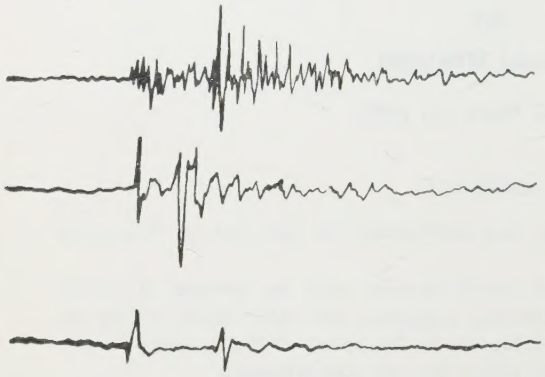

Fig. 1. Examples of seismograms.
(a) A-type, seismogram recorded at Nokami (No. 228)
(b) B-type, seismogram recorded at Wakanoura (No. 228)
(c) B-type, seismogram recorded at Yoro (No. 118)

In these observations, registration was made by direct connection of the electromagnetic seismometers of 0.45 sec in natural period with a galvanometer of 0.40 sec in free period. The paper speed of the oscillogram was about 5 mm/sec, and the time was marked every second on the seismogram by the JJY standard short-wave. The instruments used at all stations were of the same type. It is, therefore, possible to compare the seismograms at the respective stations with each other without taking into consideration the mutual differences of the characteristics of the instruments.

The recorded seismograms can be roughly divided into two classes; A and B, as shown in Fig. 1. In type-A, the initial motions of both *P*- and *S*-waves are followed by fairly regular oscillations similar to sinusoidal waves (i.e., the seismograms recorded at Idakiso and Nokami). In type-B, on the contrary, only the impulsive initial motions of the *P*- and *S*-waves are clearly recorded and are not followed by sinusoidal oscillations. In both cases the recorded times of the first zero of initial motion for both waves were measured, and the average periods for four or five oscillations of the *P*- and *S*-wave groups were read from seismograms of type-B. The periods of *S*-waves were measured only from clear records. Measurements of these periods were made mainly for the records of vertical component.

3. Periods of initial motion of *P*- and *S*-waves

(1) *Correction for recorded period*

It is difficult, in general, to take out the true wave-form of the initial motion of incident seismic waves from the recorded seismograms. Therefore, in order to deduce

it, the method of comparing the record calculated from the previously assumed form of incident wave with the real seismogram is usually adopted. Now, both our seismometer and galvanometer are critically damped and their natural periods are nearly equal. Hence, in this paper, the hypothetical record was calculated from the assumed incident wave, according to Kawasumi's method (**2**) based on Galitzin's results and

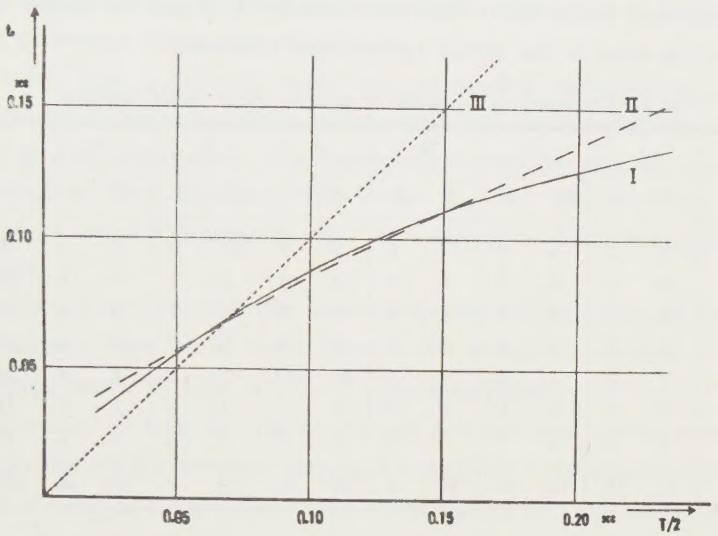

Fig. 2. Theoretical relations between the half-period of initial motion of incident waves and the time of first zero on the ercord, in the case of our seismometer-galvanometer connection.

T: the period of the incident wave
t_0: the time of first zero on record

to Tajime's method (**3**). Fig. 2 indicates the relation between the half-period of initial motion for the incident wave and the time of the first zero of waves recorded which could be obtained by calculation. The full line (I), broken line (II) and dotted line (III) in the figure correspond to the following three cases respectively assuming the incident wave to be of the form;

i) $f(t)=0$ for $t<0$ and $f(t)=\sin pt$ for $t\geqq 0$;
ii) $f(t)=0$ for $t<0$ and $f(t)=3\sin pt-\sin 3pt$ for $0\leqq pt\leqq\pi$;
iii) the stationary state in the first case.

As can be seen in Fig. 2, the recorded times of the first zero in the cases of i) and ii) make no appreciable difference in the range $0.05<T/2<0.17$ sec or $0.05<t_0<0.12$ sec, whichever form of the incident wave was assumed to be. In the present case, the recorded times of the first zero in 85% of our 163 seismograms, for the shocks of less than 5.0 sec in their $P\sim S$ times, are within the said range. Accordingly,

the half-period of initial wave was calculated from the recorded time of the first zero on the seismograms, assuming the form of incident wave to be a disturbance resembling to case ii) owing to the reasons which will be mentioned subsequently. The same procedure was pursued for the *S*-waves.

Table I shows the frequency distribution of the half-period of initial motion at each station, obtained by the above-described method. It should be further remarked that the measuring error of the period is less than 1/100 sec.

Table I. Frequency distribution of half-period of initial motion.

Station / Period	I		F		W		N		K		Y		Total	
	P	*S*	*P*	*S*	*P*	*S*	*P*	*S*	*P*	*S*	*P*	*S*	*P*	*S*
s s														
0.03 — 0.06	7	2	5	2	7	1	3	1	10	0	3	2	35	8
0.06 — 0.08	12	3	6	4	7	1	4	4	2	1	5	1	36	14
0.08 — 0.10	4	4	3	3	1	0	9	5	2	1	3	3	22	16
0.10 — 0.12	1	5	2	1	0	1	6	2	1	0	5	1	15	10
0.12 — 0.15	7	2	1	0	0	0	12	10	2	1	4	4	26	17
0.15 — 0.20	0	1	0	0	1	0	6	7	3	3	1	2	11	13
> 0.20	0	0	2	0	2	0	7	2	2	2	5	5	18	9
Total	31	17	19	10	18	3	47	31	22	8	26	18	163	87

(2) *Relation between the half-period of the initial motion and the focal distance*

The relationship between the period of seismic waves and the distance travelled by them, concerning distant earthquakes as well as near quakes, has been investigated by many researchers (**4**, **5**, **6**, **7**, **8**, **9**, **10**). There are, however, few investigations about the period of initial motion or of the very near shocks as recorded

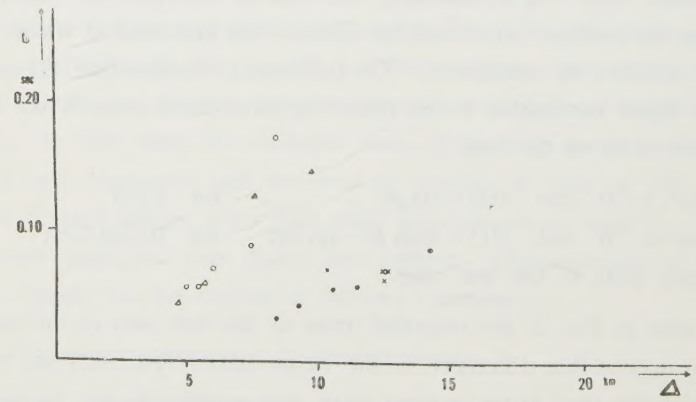

Fig. 3. Relation between the half-period of initial motion of *P*-wave and the hypocentral distance.

○: No. 218 ●: No. 230 △: No. 250 ×: No. 228

in this observation, and so the problem on the period of initial waves of such local shocks and their travel-distance will be treated here.

Firstly, as to several clearly recorded earthquakes (Nos. 218, 228, 230, 250) (**1**) the half-periods of initial motion of *P*-waves observed at the respective stations were plotted against their hypocentral distances, as shown in Fig. 3. This relation is not uniquely determined for all shocks, but the half-periods tend to increase remarkably with the increasing distance in each shock.

Secondly, Figs. 4 (a)~(f) show the relationship between the half-periods of initial *P*- and *S*-waves or their period ratios and the travel-distance in all shocks observed at each observatory. For convenience's sake the abscissa indicates the $P\sim S$ times instead of focal distances. The circle (○), dot (●) and cross (×) show the half-period of initial *P*-waves, t_P, that of *S*-waves, t_S, and their period ratio, t_S/t_P, respectively.

Figs. 5, 6 and 7 illustrate the above-described relations for all shocks observed at all stations. That is, in these figures, the preceding relations in the respective observatories shown in Figs. 4 (a)~(f) are superposed.

Half-periods of both the initial *P*- and *S*-waves are spread over a fairly wide range. On the whole, however, they have a tendency to increase with a certain range, as the $P\sim S$ time or the travel-distance increases, and the increasing rates become less gradually. The rate of this increase for the *P*-wave at the two stations, Kainan and Yoro, seems to be slightly less than that at other stations.

Thirdly, as illustrated in Fig. 7, the ratio of the half-period of the initial *S*-wave to that of the *P*-wave has no fixed value and rather decreases rapidly with increase in travel-distance. This fact may be considered to indicate that the increasing rate relative to the focal distance for the latter is greater than that for the former, as can also be seen by comparing Fig. 5 with Fig. 6. This contrasts sharply with the case in the average periods of the both waves, which will be mentioned subsequently. The similar tendency that some difference is recognizable between the increasing rates for the *P*- and S-waves was observed also by A. E. Jones (**5**) in Hawaii.

(3) *Relation between the periods of the initial motion and the earthquake magnitude*

With a view to investigate the relationship between the half-periods of initial *P*- and *S*-waves and the corresponding earthquake magnitude, the magnitude of shocks was classified into three degrees with the product of recorded maximum amplitude and the $P\sim S$ times at each station, $A_m\times(P\sim S)$. This quantity means the maximum amplitude of every earthquake at a certain fixed distance. The triangle, circle and square in Figs. 5 and 6 illustrate the half-periods in the shock of which $A_m\times(P\sim S)$ is less than 20, in the range from 20 to 50, and larger than 50, respectively, at the

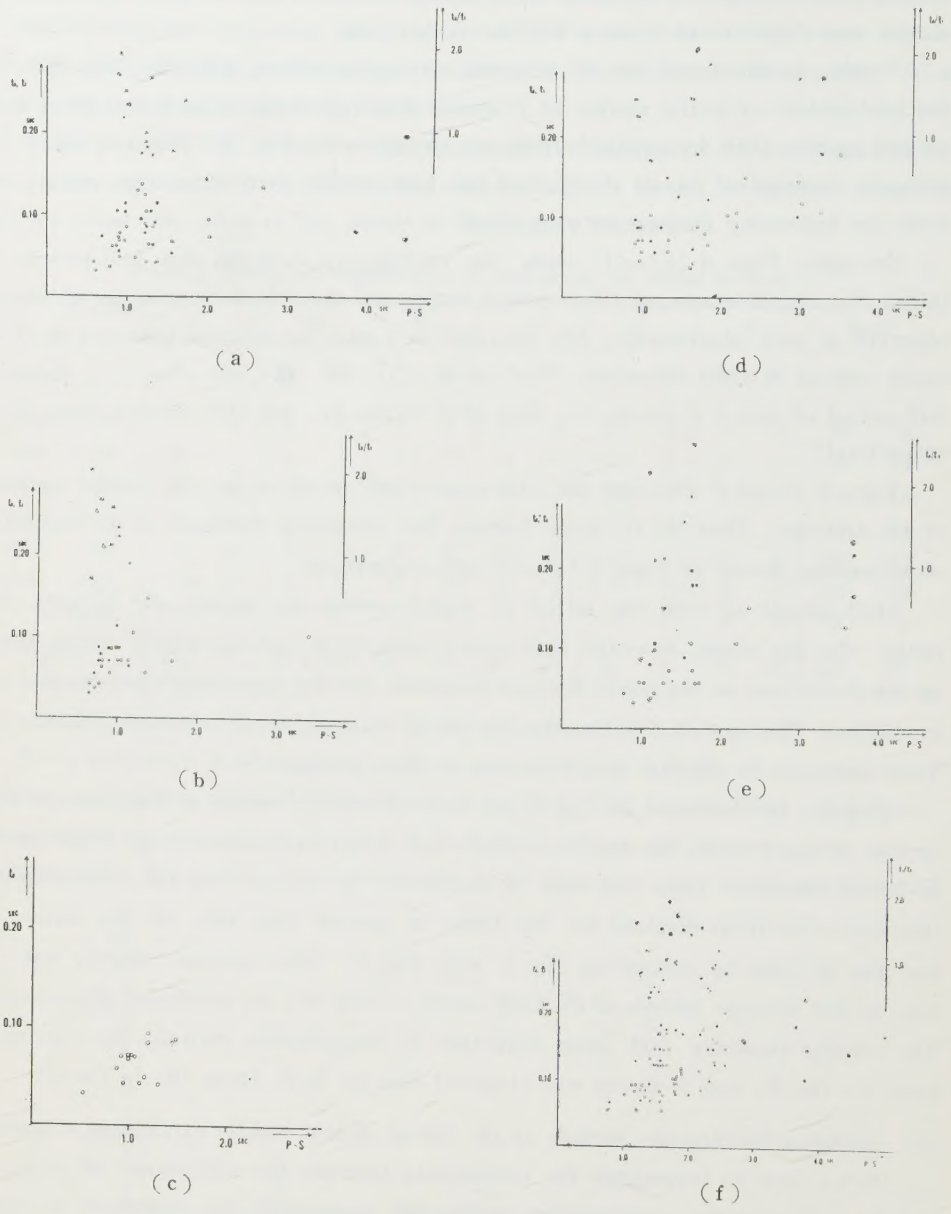

Fig. 4. Relations between the half-periods of initial *P*- and *S*-waves or their periods ratio and the focal distance, observed at each station.

○: t_P, half-period of initial *P*-wave ●: t_S, half-period of initial *S*-wave
×: t_S/t_P, periods ratio of both waves
(a) Idakiso, (b) Fuyuno, (c) Wakanoura,
(d) Kainan, (e) Yoro, (f) Nokami

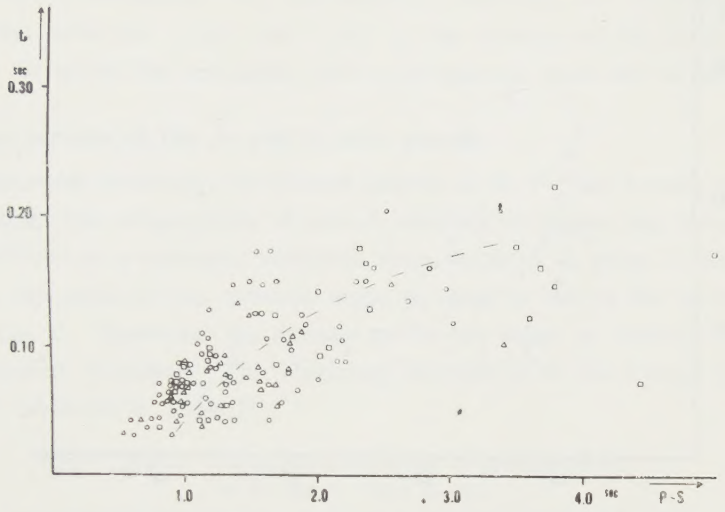

Fig. 5. Relation between the half-period of initial *P*-wave and the focal distance, for all shocks observed at all stations.

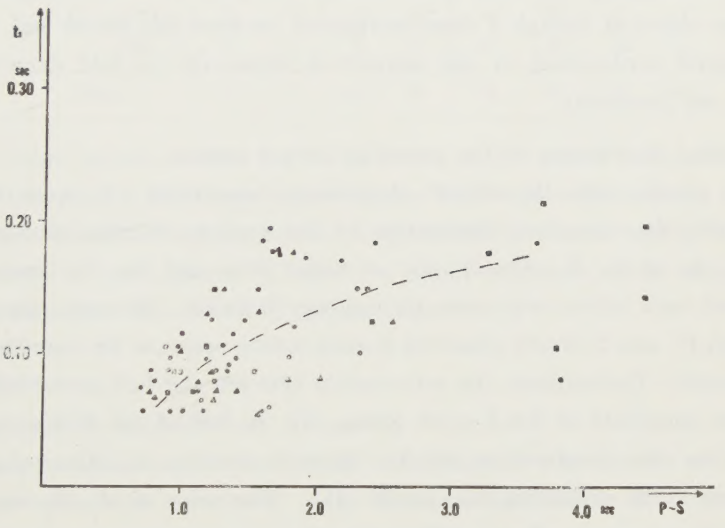

Fig. 6. Relation between the half-period of initial *S*-wave and the focal distance, for all shocks observed at all stations.

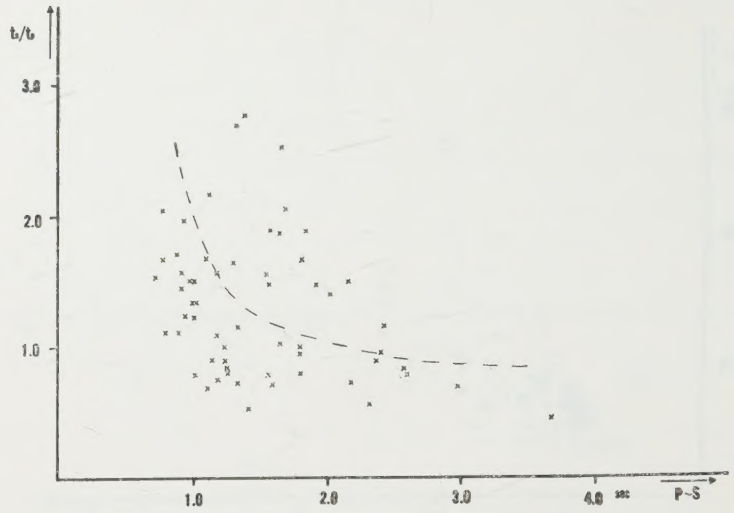

Fig. 7. Relation between the ratio of the half-periods of initial P- and S-waves and focal distance.

standard station Nokami. The energies released from these earthquakes are roughly estimated (**9**) to be less than 10^{11} ergs, in the order of $10^{11}\sim10^{12}$ ergs, and more than 10^{12} ergs, respectively. As we can see in these figures, no remarkable difference in the periods concerning the magnitude of the earthquake can be recognized within these ranges observed, though a close correlation between the period and the magnitude in natural earthquakes or the amount of explosives in field experiments has been found out frequently.

(4) *Azimuthal distribution of the period of initial motion*

Several shocks with the already determined hypocentre (**1**) were selected in order to study the azimuthal distribution of the periods of initial motion. In each earthquake, the angle, θ, between one of nodal lines and the line connecting the epicentre and each station was measured counter-clockwise. However, the half-period of the initial P- and S-waves observed at each station seems to be unrelated to $\cos\theta$, in all the shocks. Furthermore, the relationship between the half-period and the ratio of maximum amplitude of the S-wave group, A_S, to that of the P-wave group, A_P, at each station was examined for all the observed shocks. A_S/A_P or $A_S/A_P(P\sim S)$ is considered to be proportional to $\cot 2\theta$ (**11**). The value of A_S/A_P was corrected by magnification response of our seismometer for the respective periods of the P- and S-waves. The half-period of the P-waves seems to decrease slightly with an increase in $A_S/A_P(P\sim S)$. In none of the afore-mentioned cases, however, any clear evidence touching azimuthal distribution of those periods depending upon an earth-

quake generation mechanism (**12**) was detected. Moreover, any difference in period, in connection with the 'push' and 'pull' in the direction of the initial motion, or relating to the travel-time anomalies previously reported, could not be ascertained.

4. Average periods of the *P*- and *S*-wave groups

As mentioned previously, the average periods of the *P*- and *S*-wave groups were measured from the seismograms of type-A recorded at Idakiso and Nokami. When the incident wave is in stationary oscillation as in the form i), stated in the preceding paragraph, the period of the recorded wave is equal to that of the incident one, as shown in Fig. 2. Therefore, the average period can easily be obtained from a seismogram without correction. The frequency distribution of the average periods thus obtained is tabulated in Table II.

Table II. Frequency distribution of average period of *P*- and *S*- wave groups.

Station	I		N		Y		Total	
Period / s	*P*	*S*	*P*	*S*	*P*	*S*	*P*	*S*
<0.10	2	4	0	0	0	0	2	0
0.10 — 0.13	13	8	7	2	2	1	22	11
0.13 — 0.15	11	11	18	8	4	3	33	22
0.15 — 0.17	5	7	7	14	1	3	13	24
0.17 — 0.20	1	2	6	12	4	3	11	17
>0.20	0	0	3	1	5	8	8	9
Total	32	32	41	37	16	18	89	83

The average periods scatter less widely than in the case of half-period of initial motion. When plotted, they have approximately fixed values irrespective of the $P\sim S$ times or travel-distances and earthquake magnitudes, as shown in Fig. 8, and differ from the cases of half-periods. There is a slight difference in the mean values of average periods observed at two of the stations.

5. Discussion

(1) *Periods of the initial P- and S-waves*

The cause of increase in the period of earthquake waves with an increase in travel-distance has been considered to be mainly attributable to the viscosity of the medium for wave propagation, since the other effects, such as scattering due to heterogeneity in the medium or superposition (**13**) of the various waves, seems to be comparatively little. The attenuation factor of amplitude in relation to travel-distance for the waves propagating in visco-elastic medium (for example, the Voigt model) is

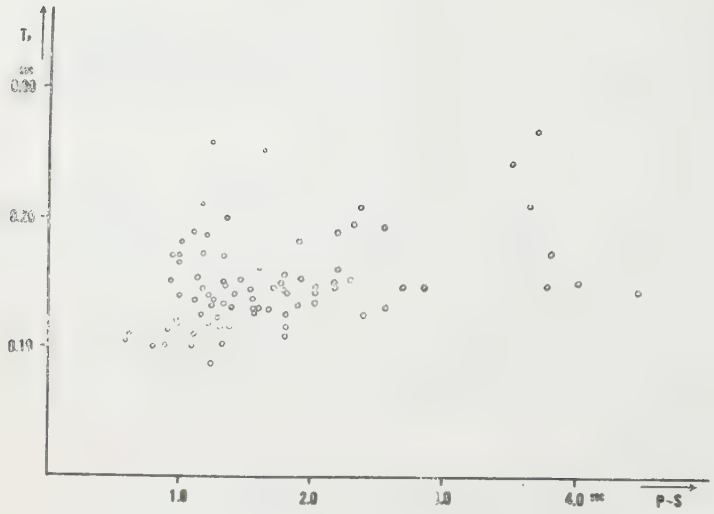

(a) Average period of *P*-wave group.

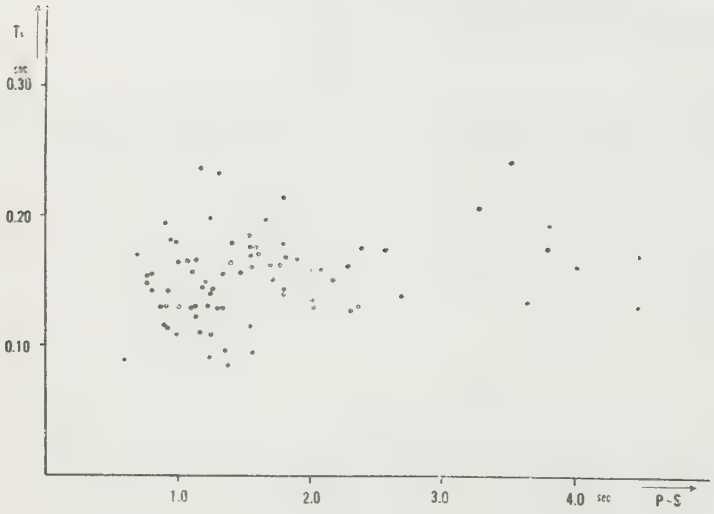

(b) Average period of *S*-wave group.

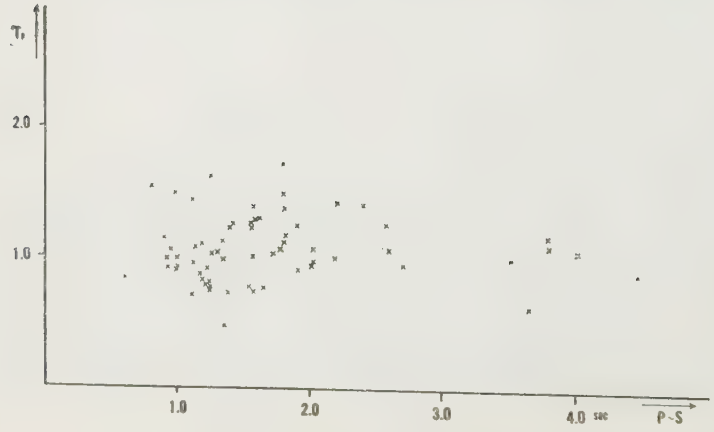

(c) Ratio of the average periods of *P*- and *S*-wave groups.

Fig. 8. Relations between the average periods of *P*- and *S*-wave groups or their period ratio and the focal distance.

proportional to the square of the wave frequency (**14**, **15**, **16**). Hence, the waves with longer periods survive as the travel-distance increases, because the wave components of higher frequency decay more rapidly. K. Sezawa studied theoretically the problem of wave propagation in the visco-elastic medium of Voigt solid when several types of disturbance were generated at the origin (**17**). From these results, B. Gutenberg established and expressed the relation between the period of seismic wave and the focal distance in the formula (**18**) ;

$$T = \sqrt{T_0^2 + \frac{\alpha}{V^3}\Delta}, \tag{1}$$

where T and T_0 are the observed period and the original period emitted from the focus, respectively, Δ is the hypocentral distance, V the velocity of wave propagation and α a constant.

Next, we try to explain, from the standpoint of the visco-elastic medium, the fact that the half-periods of the P-wave increase more rapidly than that of the S-wave as to the focal distance. As one of the simplest model of visco-elastic medium, the Voigt model was adopted in the present case. Our observed results shown in Figs. 5 and 6 indicate that the respective mean curves are in fairly good accordance with the above Gutenberg's formula. Hence, the relationship between the half-periods and the travel-distance of the P- and S-waves can be represented by the following formulae :

$$\left.\begin{aligned} T_P &= \sqrt{T_{P0}^2 + \frac{\alpha}{V_P^3}\Delta} \quad \text{for } P\text{-wave}, \\ T_S &= \sqrt{T_{S0}^2 + \frac{\beta}{V_S^3}\Delta} \quad \text{for } S\text{-wave}, \end{aligned}\right\} \tag{2}$$

and

$$\alpha = K\frac{\lambda' + 2\mu'}{2\rho}, \quad \beta = K\frac{\mu'}{2\rho}, \tag{3}$$

where T_{P0} and T_{S0} are the original periods and V_P and V_S are the propagation velocities, for the P- and S-waves, respectively. λ' and μ' are the viscosity coefficients analogous to Lamé's elastic constants λ and μ. μ' and $\lambda' + \frac{2}{3}\mu'$ are the so-called shear viscosity and dilatational viscosity respectively, ρ is the density and K is a numerical constant determined from the form of disturbance at the origin.

From (2), we get

$$\alpha = V_P^3 \frac{dT_P^2}{d\Delta}, \quad \beta = V_S^3 \frac{dT_S^2}{d\Delta}, \tag{4}$$

and therefore

$$\frac{\alpha}{\beta} = \left(\frac{V_P}{V_S}\right)^3 \cdot \frac{dT_{P2}^2}{d\Delta} \Big/ \frac{dT_S^2}{d\Delta}. \tag{5}$$

Also from (3), we have

$$\frac{\alpha}{\beta}=\frac{\lambda'}{\mu'}+2. \qquad (6)$$

The coefficients α and β can be determined from the observed results by the method of least squares, but were roughly estimated in the present treatment by means of a simple procedure. In this calculation the following values of V_P, V_S and Omori's constant k were used, which have already been determined on the crustal structure in Wakayama District (**1**).

$V_P = 4.3$ km/sec, $V_S = 2.5$ km/sec and $k = 6.0$ in the surface layer,
$V_P = 5.5$ km/sec, $V_S = 3.2$ km/sec and $k = 7.6$ in the second layer.

The observed period contain all those in the cases that the focus is both in the upper layer and in the second layer. Considering two extreme cases in which the crust is only of the uniform medium of 4.3 km/sec or 5.5 km/sec in propagation velocity, the real values of α and β should be calculated as the values between these two. Taking these circumstances into consideration, we find

$$7.2\times10^{9}<\alpha<1.2\times10^{10} \quad \text{c.g.s.},$$
$$1.0\times10^{9}<\beta<1.7\times10^{9} \quad \text{c.g.s.}.$$

The calculated value of α agrees in its order of magnitude with the previously obtained ones by Gutenberg (**18**), Asada and Suzuki (**8**) and others. No result as to the value of β for S-waves can be traced.

Taking the following values as the mean density (ρ) and rigidity (μ) in the upper layer of metamorphic rocks and in the second layer of granite, namely:

$\rho = 2.64$, $\mu = 2.30\times10^{11}$ c.g.s. for the upper layer,
$\rho = 2.67$, $\mu = 2.87\times10^{11}$ c.g.s. for the second layer,

λ' and μ' can be calculated by Eq. (3) as follows, assuming the value of K to be 8~11 (**18**):

$$2.5\times10^{9}<\lambda'<6.4\times10^{9} \quad \text{c.g.s.},$$
$$4.8\times10^{8}<\mu'<1.2\times10^{9} \quad \text{c.g.s.},$$
$$1.7\times10^{-3}<\mu'/\mu<5.2\times10^{-3}.$$

The viscosity coefficients thus obtained are in approximate accordance with the values determined by Jeffreys (**19**), Sezawa and Kanai (**20**) and others, and the value of μ'/μ agrees in its order both with laboratory data on various rocks and with field experiments (**21**).

Moreover, the following results are obtained from Eqs. (5) and (6),

$$\frac{\alpha}{\beta}=7.36, \quad \frac{\lambda'}{\mu'}=5.36.$$

The ratio of dilatational viscosity to shear viscosity, $\lambda'/\mu'+2/3$, is calculated to be about 6. Few values of λ'/μ' have been determined by laboratory experiments. K. Iida (**22**) published his experimental result of $\lambda'/\mu'=6.43$ for pumice at zero water content. It is also reported by another investigator (**23**) that λ'/μ' is nearly 36 for a kind of metal (nickel). Therefore, our calculated value is not an unexpected one.

As to the ratio of the period of the initial P-wave to that of the S-wave, K. Kanai discussed theoretically (**24**) in the case of a perfect elastic medium, and showed that the latter is about twice the former, taking into account the correction due to a constant of seismograph (**25**). On the other hand, this ratio becomes nearly 1.8, which can be obtained from Jeffreys' theoretical calculation (**26**). But these results indicate that the ratio of the above two periods do not change as to the travel-distance.

In order to explain the results illustrated in Fig. 7, the formulae (2) in the case of visco-elastic medium can be cited and rewritten in the form:

$$\frac{T_S}{T_P}=\sqrt{\frac{T_{S0}^2+\beta\Delta/V_S^3}{T_{P0}^2+\alpha\Delta/V_P^3}}\,. \qquad (2')$$

As the hypocentral distance Δ increases, T_S/T_P changes from T_{S0}/T_{P0} to $\sqrt{\frac{\beta}{\alpha}\left(\frac{V_P}{V_S}\right)^3}$. The original periods T_{P0} and T_{S0} cannot easily be determined by extrapolation of the results in Figs. 5 and 6. The observed minimum half-period of the P-wave is 0.03 sec, and that of the S-wave is 0.06 sec. If these values correspond to the original half-periods approximately, T_S/T_P decreases from 2 to 0.8 with an increase in focal distance. The results shown in Fig. 7 can be known from these points of view.

Comparing, then, the increasing rates of the periods of the initial P- and S-waves with each other, we find theoretically the following relations from the formulae (5) and (6):

$$\frac{dT_P^2}{d\Delta}\gtrless\frac{dT_S^2}{d\Delta}\,, \quad \text{according as} \quad \lambda'/\mu'\gtrless 3.1\,,$$

assuming Poisson's ratio to be 0.25. That is, it is the case of $\lambda'/\mu'>3.1$ when the increasing rate of the period of P-wave with increasing distance is larger than that of the S-wave. The presently obtained value of λ'/μ' is within this range, and may be considered to be reasonable one from the above consideration about the experimental data and from the aspect of the attenuation factor of amplitude obtained by some researchers.

Consequently, our observed results are explainable, if we consider the dilatational viscosity in the medium of wave propagation to be about six times as large as the shear viscosity.

However, the above relation cannot hold without any modification for more distant

earthquakes. Otherwise, the period of the P-wave come to be longer than that of the S-wave at a long distance. This is not generally acceptable. This problem may probably be solved, if the value of λ'/μ' at depth is smaller than at the shallower crust and $\lambda'/\mu' < 3.1$ on the ground that the initial wave propagates more deeply in the crust to a distant station.

On the other hand, N. Ricker stated in his wavelet theory on the visco-elastic medium that the wavelet breadth is proportional to the square root of the travel time of its centre (**28**, **29**). He confirmed his theory by field experiments and calculated the viscosity of shale from the relation between the wavelet breadth, b, and travel time, t; $b^2/t = \text{const.}$ (**30**). This can be rewritten into the formula relating the period, T, with the travel-distance, Δ, as follows:

$$T = 4\sqrt{\frac{\eta}{\rho V^3}\Delta}, \qquad (7)$$

where η is the viscosity of the medium for wave propagation, and can be expressed by $\eta = \frac{3}{4}(\lambda' + 2\mu')$ for the P-wave, and by $\eta = \mu'$ for the S-wave, in terms of λ' and μ'. In this case the form of disturbance at the origin was assumed to be of a rectangular type. If Eq. (7) is applied to our data, η is estimated to be of the order of 10^9 c.g.s. for propagation of the P-wave and 10^8 c.g.s. for that of the S-wave, adopting the previously mentioned crustal structure. Here, however, the ratio of the period of the initial P-wave to that of the S-wave is constant, regardless of travel-distance. Therefore, Ricker's formula cannot give a complete explanation to our observed results.

Consequently, we may consider that Gutenberg's formula can most suitably express our obtained data.

(2) *Average period*

The average periods of the P- and S-wave groups may be considered to represent the approximate predominant periods in their respective groups. The fact that there is a different predominant period in every station has been approved from many observations since some ten years ago (**31**). The predominant period was attributed (**32**) to the period of free oscillations of superficial layer, which is secondarily excited by multiple reflections in that layer in the case of incidence of impulsive initial shocks, and the possibility of free oscillations of the surface layer was also studied theoretically (**33**, **34**). According to those investigations, free oscillations have a periodicity when the length of disturbance in the impulsive wave is longer as compared with the thickness of surface layer. Hence, the predominant period depends upon the thickness of the surface layer, and the fact that it has a certain definite value scarcely relating to the travel-distance of seismic waves, the earthquake magnitude etc., has been ascertained (**35**, **36**). This agrees with our present findings.

Judging from seismograms recorded at Wakanoura, Kainan and especially at Yoro, the initial *P*– and *S*–waves seem to be fairly impulsive, as shown in Fig. 1. Therefore, the sinusoidal oscillations following the initial motion recorded at Idakiso and Nokami may be considered to be free oscillations of the superficial layer, composed of weathered schist, excited by the initial motion. The relationship between the surface thickness and the period of body waves has been estimated to various forms, not only in observations of near earthquakes (**6**, **37**, **38**, **39**) but also in field experiments (**40**, **41**). According to the results of these researches, the thickness of the superficial layer near the above two stations is presumed to be less than 100 m, even if the velocity in this layer is assumed to be nearly 2 km/sec. The delay in travel-time due to the existence of this layer is within 0.03 sec and has no effect upon the travel-time anomalies discussed in the previous paper.

6. Concluding remarks

The following results were obtained from a period analysis for the body waves of local earthquakes observed in Wakayama District.

i) The initial waves are considered to be of an impulsive character. Their periods increase with increasing distance travelled by the waves, but they are related neither to the magnitude of earthquake nor to other effects within the range of our observation. No clear evidence on azimuthal distribution for the periods was recognizable.

ii) The cause for the increase of periods of initial waves with an increase in focal distance is attributable to the viscosity of the medium for wave propagation. The relation between the periods of initial *P*– and *S*–waves and the travel-distance can approximately be expressed by Gutenberg's formula, but the increasing rate of the former is more rapid than that of the latter. This may be by reason that the dilatational viscosity of the medium is considerably larger than the shear viscosity. Our present results can be explained by the hypothesis that the dilatational and shear viscosities have the order of $10^{9}\sim10^{10}$ and $10^{8}\sim10^{9}$ in c.g.s. units, respectively, and the former is about six times the latter.

iii) The average periods of the *P*– and *S*–wave groups have a certain fixed value irrespective of the focal distance, the earthquake magnitude and other effects, within the scope of this observation. Namely, they may be closely related to the conditions of the observation station.

Acknowledgement

The writer wishes to express his sincere thanks to Prof. E. Nishimura and Messrs. T. Nishitake, Y. Kishimoto and M. Ōtsuka of our institute for their kind advices.

REFERENCES

1. T. Mikumo, Precise seismometric observations in the epicentral region of local shocks, Mem. Coll. Sci. Kyoto Univ. Ser. A, **28** (1956), 161.
2. K. Kawasumi, Theoretical and experimental study of initial motion of seismographs and qualitative study of first impulse of earthquakes, Bull. Earthq. Res. Inst., **14** (1936), 330.
3. K. Tajime, Seismometric investigation of the initial motion, Rep. Inst. for Underground Resources of Akita Univ., **14** (1955), 28 (in Japanese).
4. J. B. Macelwane, A study of the relation between the periods of elastic waves and distance travelled by them, based upon the seismographic records of the California Earthquake, January 31, 1942, Bull. Seism. Soc. America, **13** (1923), 56.
5. A. E. Jones, Empirical studies of some of the seismic phenomena of Hawaii, Bull. Seism. Soc. America, **28** (1938), 313.
6. K. Iida, Sur les caractéristique des ondes séismique d'après nos observations à l'aide des grands sismographes accélérométrique d'une tonne, Bull. Earthq. Res. Inst., **18** (1940), 532.
7. P. Byerly, The periods of local earthquake waves in central California, Bull. Seism. Soc. America, **37** (1947), 291.
8. Z. Suzuki and T. Asada, On aftershocks of the Nankai Earthquake, 2. Periods of seismic waves, Geophysical Notes, Tokyo Univ., No. 33 (1949), 1 (in Japanese).
9. T. Asada and Z. Suzuki, On microearthquakes having accompanied aftershocks of the Hukui Earthquake of June 28, 1948, Geophysical Notes, Tokyo Univ., No. 2 (1949), 1.
10. K. Aki, Correlogram analysis of seismograms, Journ. Seism. Soc. Japan, Ser. 2, **8** (1955), 99 (in Japanese).
11. H. Honda, The mechanism of earthquake, Sci. Rep. Tohoku Univ., Ser. 5, Geophysics, **9**, Suppl. 30 (1957).
12. S. Komura, A consideration about the mechanism of the occurrence of severe earthquake, 1, 2, Journ. Seism. Soc. Japan, Ser. 2, **9** (1957), 174; **10** (1957), 1.
13. I. Tamaki, Some problems on the ground motion near explosions, 1, Geophys. Explor. Japan, **5** (1952), 189 (in Japanese).
14. K. Sezawa and K. Kanai, Damping of periodic visco-elastic waves with increase in focal distance, Bull. Earthq. Res. Inst., **16** (1939), 491.
15. H. Kolsky, *Stress Waves in Solids* (1953), 99-129.
16. F. Collins and C. C. Lee, Seismic wave attenuation characteristics from pulse experiment, Geophys., **21** (1956), 16.
17. K. Sezawa, On the decay of waves in visco-elastic solid bodies, Bull. Earthq. Res. Inst., **3** (1927), 43.
18. B. Gutenberg, *Handbuch der Geophysik*, Bd. 4, Leif. 1 (1932), 16-22.
19. H. Jeffreys, The viscosity of the Earth, Mon. Not. Roy. Astr. Soc. Geophy. Suppl., **1** (1928), 416.
20. K. Sezawa and K. Kanai, Viscosity distribution within the Earth, Bull. Earthq. Res. Inst., **18** (1940), 169.
21. F. Birch, J. F. Schairer and H. C. Spicer, *Handbook of Physical Constants*, Geol. Soc. America, Spec. Paper (1944), 88-92; 133.
22. K. Iida, Elastic and viscous properties of a certain kind of rock, Bull. Earthq. Res. Inst., **17** (1937), 59.
23. J. H. C. Thompson, On the theory of visco-elasticity, Phil. Trans. Roy. Soc., **231** (1933), 347.
24. K. Kanai, Possibility of the period of *P*-waves becoming smaller than those of *S*-waves, Bull. Earthq. Res. Inst., **29** (1951), 529.

25. K. KANAI, Examination of the assumption concerning mechanism of earthquake origin through seismograms, Bull. Earthq. Res. Inst., **30** (1952), 39.
26. H. JEFFREYS, On the cause of oscillatory movements in seismograms, Mon. Not. Roy. Astr. Soc. Geophys. Suppl., **2** (1931), 407.
27. H. ARAKAWA, Dispersion and absorption of the dilatational and distortional waves in visco-elastic solid, Geophys. Mag., **4** (1931), 215.
28. N. RICKER, Further development in the wavelet theory of seismogram structure, Bull. Seism. Soc. America, **44** (1943), 197.
29. N. RICKER, The form and laws of propagation of seimic wavelets, Geophys. **18** (1953), 10.
30. N. RICKER, A note on the determination of the viscosity of shale from the measurement of wavelet breadth, Geophys., **6** (1941), 254.
31. A. IMAMURA, On the earth-vibrations induced in some localities at the arrival of seismic waves, Bull. Earthq. Res. Inst., **7** (1929), 481 (in Japanese).
32. M. ISHIMOTO, Comparaison accélérométrique des secousses sismique dans deux parties de la ville de Tokyo, Bull Earthq. Res. Inst., **10** (1932), 171.
33. K. SEZAWA, Possibility of the free oscillations of the surface-layer excited by the seismic waves, Bull. Earthq. Res. Inst., **8** (1930), 1.
34. K. SEZAWA and K. KANAI, Possibility of free oscillations of strata excited by seismic waves, Bull. Earthq. Res. Inst., **10** (1932), 1; 273.
35. M. ISHIMOTO, Observations des périodes prédominantes dans les secousses séismique dont la distance épicentrale est assez grande, Bull. Earthq. Res. Inst., **15** (1937), 536 (en Japonais).
36. T. MINAKAMI and S. SAKUMA, The earthquake motions on various formations of the Earth's surface, Bull. Earthq. Res. Inst., **26** (1948), 61.
37. M. ISHIMOTO, Observations des périodes prédominantes dans les secousses sismique, Bull. Earthq. Res. Inst, **14** (1936), 240 (en Japonais).
38. S. OMOTE, N. KOBAYASHI and S. KOMAKI, Earthquake observations in Kawasaki and Tsurumi areas and the seismic qualities of the ground, Bull. Earthq. Res. Inst., **34** (1956), 335.
39. B. GUTENBERG, Effects of ground on earthquake motion, Bull. Seism. Soc. America, **47** 1957 , 221.
40. M. HAYAKAWA, Some problems of seismic exploration, Rep. Geol. Survey, Japan, No. 137 (1951), 30 (in Japanese).
41. I. TAMAKI, Some problems on the ground motion near explosions, 2, Geophys. Explor. Japan, Vol. 6, No. 1 (1953), 30 (in Japanese).
42. K. IIDA and H. AOKI, On the visco-elastic waves radiated from a spherical cavity in elastico-viscous medium, Journ. Earth Science, Nagoya Univ., **3** (1955), 105.

Memoirs of the College of Science, University of Kyoto, Series A,
Vol. XXIX, No. 1, Article 2, 1958.

ON THE SEISMIC WAVES REFLECTED AT THE MOHOROVIČIĆ DISCONTINUITY (II)

BY

Akira KAMITSUKI

(*Received March 20, 1958*)

1. Introduction

Recently the investigation of the earth's crust has developed remarkably. Above all, the method using seismic waves which are transmitted through the crust is considered to be the most direct and powerful. Up to the present time, it was ascertained that the earth's crust usually consists of several layers separated by discontinuity surfaces. It was found that the crustal structure has the significant contrast between continents and ocean basins and has local difference from place to place. Furthermore, in America and some other regions, it is suggested that there may be a low-velocity layer in which the velocities of seismic waves decrease with the increase of depth. Thus more detailed discussions on the earth's crust need to be carried out.

In general, the records of near earthquakes are the major sources of information about the earth's crust, but practically speaking, various effects are superposed on one another, and the records are greatly complicated. Then it must be considered that these effects should be selected separately by some instrumental device and be caught with much certainty. On the other hand, it is also desirable for the observation stations to be distributed as densely as possible so that many records are available in the proper range of distance. And not only the travel time, but also the amplitude, period, wave form and other elements of seismograms should be traced continuously with distance and azimuth. From these more detailed informations about the earth's crust will be able to be obtained.

In seismometric analysis, there are different sorts of method of using the refraction, reflection, dispersion of surface waves and others. In the analysis of near earthquakes, the refracted waves are mainly investigated, that is, P^* and P_n of P-group or corresponding S^* and S_n of S-group, but movements between P- and S-phases are less studied. Jeffreys and Bullen suggested that these movements may be caused by the strong repeated reflection of bodily waves between the earth's outer surface and the crustal discontinuity (**1**, **2**). These phases were interpreted as pP, PP, etc. in analogy to distant earthquake by some researchers (**3**), but in this interpretation there is a disagreement in travel time relation. And there remain still

insolvable characters (**4, 5, 6**). Furthermore, in the part after *S*, the strong phases are frequently recognized but in this case, the appearance of surface waves should be considered together (**7, 8, 9**).

In our previous paper (Part I), the seismograms of near earthquake within about 100 km were studied, taking special account of the primary reflection of *S*-wave at some crustal discontinuities. As a continuation of Part I, the seismograms of shallow-seated earthquake recorded in the distance range from about 100 km to 600 km are investigated in the present paper, and the parts of seismograms between the *P*- and *S*-waves are mainly studied and its relations to the earth's crust are discussed in some detail.

2. The earthquakes of March 7, 1952 and July 27, 1955

Considering the conditions to have shallow-seated origin in the crust and to be observed at as many stations as possible, the following two earthquakes were selected.

Earthquake	(1) The Daishoji-Oki	(2) The Tokushima
Origin time	1952, March, $7^d\,16^h\,32^m$	1955, July, $27^d\,10^h\,20^m$
Epicenter	36°28′N, 136°12′E	33°45′N, 134°18′E
Focal depth	20 km	0~10 km
Greatest distance of human feeling	770 km	670 km

The former caused comparatively little damage on land owing to its epicenter located off sea coast and 152 aftershocks were registered in March (**10**), while slight damage was caused by the latter at the epicentral region in Tokushima Prefecture (**11**). In order to develop the following investigation, the original seismograms recorded at the Abuyama and Kamigamo Observatories and the copied seismograms recorded at the Japan Meteorological Observatories were available. The total number of stations concerned is 32 in all. In the case of the Daishoji-Oki Earthquake, the data used were from 25 stations extending from 130 km to 670 km, and in the case of the Tokushima Earthquake, those from 24 stations extending from 40 km to 540 km were used. The locations of epicenters and stations are shown in Fig. 1.

In the following, the parts of the seismograms from the initial *P*-motion to the principal *S*-motion are studied, analysing the travel time, amplitude, period and wave form of each phase.

a) *Travel time-distance graph*

In the first place, the arrival times of three phases in the forerunning part of *P*-wave and of the corresponding ones of *S*-wave are measured. The observed values are tabulated in Tables I and II.

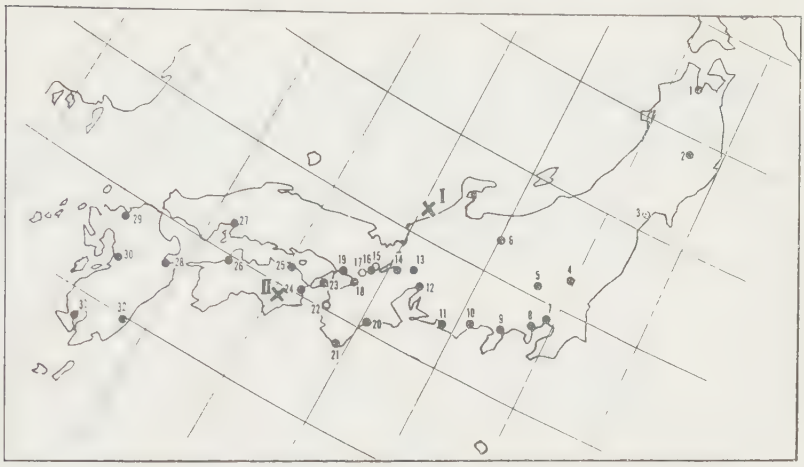

Fig. 1. The locations of epicenters and stations tabulated in Tables I and II.

Epicenters:—
(I) The Daishoji-Oki Earthquake
(II) Tokushima Earthquake

Stations:—

1. Aomori	2. Morioka	3. Sendai	4. Utsunomiya
5. Kumagaya	6. Nagano	7. Tokyo	8. Yokohama
9. Mishima	10. Shizuoka	11. Hamamatsu	12. Nagoya
13. Gifu	14. Hikone	15. Kamigamo (Kyoto Univ.)	16. Kyoto
17. Abuyama (Kyoto Univ.)	18. Osaka	19. Kobe	20. Owashi
21. Shionomisaki	22. Yuasa (Taikyu High School)	23. Sumoto	24. Tokushima
25. Takamatsu	26. Matsuyama	27. Hiroshima	28. Oita
29. Fukuoka	30. Kumamoto	31. Kagoshima	32. Miyazaki

To calculate the epicentral distance, the epicenters reported in the Seismological Bulletin published by the Japan Meteorological Agency are accepted and the following formula is used:

$$2(1-\cos \Delta) = (A-A')^2+(B-B')^2+(C-C')^2,$$

where Δ is the epicentral distance in degree and A, B and C of epicenter are defined by

$$A = \cos\theta\cos\phi, \quad B = \cos\theta\sin\phi, \quad C = \sin\theta.$$

Here, θ is the geocentric latitude, ϕ is the east longitude, and A', B', C' are the corresponding parameters for each station. The travel time–distance graphs of these two earthquakes are shown in Figs. 2 and 3 respectively. In these figures, the travel times before and after the direct P-wave (P) are taken against the epicentral distance. (Especially, the travel times of initial motion reported in the Seismological Bulletin are also plotted in Figs. 2 and 3. Then the total number of stations is 59 in the former and 54 in the latter.)

Table I. Arrival time of each phase of the Daishoji-Oki Earthquake. Station numbers are shown in Fig. 1.

No.	Station	Δ	Arrival time									
			P_n	P^*	$\overline{P}$	R_1	R_2	R_3	R_4	S_n	S^*	$\overline{S}$
		km	m s	m s	m s	m s	m s	m s	m s	m s	m s	m s
13	Gifu	133			33 1.9							
14	Hikone	133			1.4							
12	Nagoya	161	33 4.2									34 23.1
16	Kyoto	167	6.0			33 17.5						26.9
6	Nagano	180										
18	Osaka	211			15.5		33 31.5					41.3
19	Kobe	219	12.9		17.0	20.3	31.9	33 37.4			33 40.2	44.7
10	Shizuoka	260	18.9		23.7	30.4	35.2	43.1			51.4	
23	Sumoto	265	19.0		23.7	30.3	36.7	41.6			47.6	55.9
5	Kumagaya	289	23.8		30.5	33.4	40.9	50.0			56.5	34 3.2
9	Mishima	289	23.0		29.9	33.2	39.7	49.7			55.7	2.8
24	Tokushima	306	25.0	33 27.9	31.8	36.2	42.5	52.5			34 3.0	7.6
25	Takamatsu	310	25.0	27.1	31.2	38.5	45.0	51.0		33 58.8		8.0
4	Utsunomiya	328	27.8		37.1	39.2	46.3	56.3			8.5	16.9
8	Yokohama	332	27.6	32.2	37.5	39.3	49.6	55.0		34 3.2	9.6	15.8
7	Tokyo	332	27.6		37.5		49.1	54.4			8.3	19.7
27	Hiroshima	419	38.7	42.3	49.0	54.7	34 2.1	34 9.7	34 18.8	22.6	29.7	40.7
26	Matsuyama	426	38.8									44.2
3	Sendai	461	45.4	50.1	55.5		7.3	14.0	22.6	30.7	41.0	53.8
28	Oita	552	55.9	34 2.8	34 9.8		21.1	29.3	37.5	50.5	58.6	35 15.1
2	Morioka	565	57.4									
29	Fukuoka	621	34 5.9		22.7		29.8	40.2	48.0		35 21.7	38.0
1	Aomori	625	5.8									
30	Kumamoto	647	5.2	14.6	25.3		33.7	41.4	48.2	35 9.8	21.7	46.4
32	Miyazaki	669	10.6		32.2			45.8	55.6			53.5

Table II. Arrival time of each phase of the Tokushima Earthquake.
Station numbers are shown in Fig. 1.

No.	Station	Δ	Arrival time											
			P_n	P^*	$\bar{P}$	R_1	R_2	R_3	R_4	R_5	R_6	S_n	S^*	$\bar{S}$
		km	m s	m s	m s	m s	m s	m s	m s	m s	m s	m s	m s	m s
24	Tokushima	46			20 58.5									21 3.6
25	Takamatsu	67			21 2.3									11.8
22	Yuasa	87			6.3									18.5
23	Sumoto	87			4.0									
21	Shionomisaki	141		21 15.0	16.2	21 19.5	21 23.9							32.1
26	Matsuyama	141		14.6	16.4	18.7	24.3	21 28.7						31.9
17	Abuyama	171	21 19.0		21.8	24.7								41.3
20	Owashi	180	19.0		23.2		33.4						21 40.1	44.4
27	Hiroshima	185	21.3		23.7	27.0	33.3	39.9					43.0	45.2
15	Kamigamo	198	22.4		26.7	29.8	33.5	40.9				21 44.8		48.2
14	Hikone	247	29.1		34.8	37.1	41.5	45.9	21 52.1			56.8		21 2.3
28	Oita	256		32.8	36.7		41.9	45.7	52.0				59.8	9.7
12	Nagoya	291	34.5		41.2			49.2	55.7	22 0.6			22 10.8	16.8
13	Gifu	291	34.9		42.8		45.1	51.9	57.9	3.3			10.7	17.9
32	Miyazaki	326	40.3	43.3	50.6			55.5	22 2.2		22 5.1		16.5	29.4
11	Hamamatsu	332	40.9		49.5				2.5				26.3	31.8
30	Kumamoto	350	40.9	47.5	53.6			58.7	5.3	12.0	16.7	22 20.3	28.5	35.8
29	Fukuoka	363	43.0		52.6			57.9	4.8	10.1				38.3
10	Shizuoka	400	47.8		22 0.8			22 7.8	16.2	20.5		28.6	33.8	48.3
31	Kagoshima	426	50.5	55.4	4.8			10.8	18.9	23.2	31.1	34.9	42.3	56.6
9	Mishima	452	53.8	59.5	10.6			16.9	21.8		33.5	40.3	52.5	23 6.1
8	Yokohama	524	22 2.6											
5	Kumagaya	536	6.4	22 12.1	20.6				31.4	36.8	46.7	23 1.0	23 17.6	28.4
7	Tokyo	545	8.3		21.5			27.7	32.9				16.5	31.9

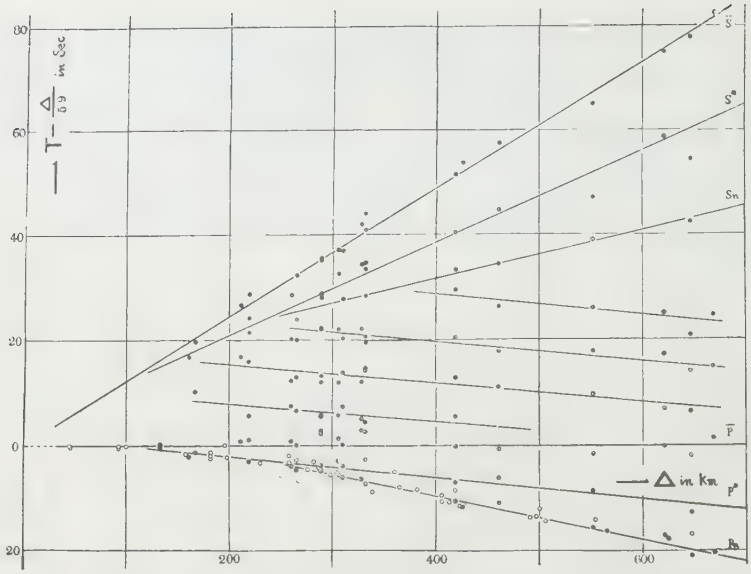

Fig. 2. Travel time–distance graph of the Daishoji-Oki Earthquake tabulated in Table I.

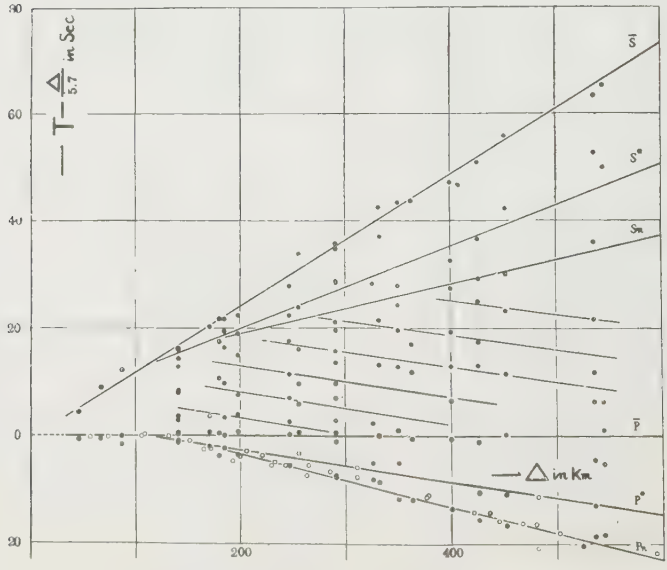

Fig. 3. Travel time–distance graph of the Tokushima Earthquake tabulated in Table II.

In the previous investigations it was stated that in our country, the crustal structure has a local difference and its thickness varies from place to place in the range between 25 km and 50 km. And moreover, its diversity is mainly due to the lowest layer, i.e. the basaltic layer (**12, 13, 14**). Relating to this fact, in the present analysis, the forerunning parts of the two earthquakes have a significant difference. Usually in the distance beyond about 100 km, the P^*-wave and the P_n-wave succeeding it appear before the arrival of direct P-wave. In the case of the Daishoji-Oki Earthquake, the distance range in which the P^*-wave is the first motion, is wider than in the case of the Tokushima Earthquake. And in the latter, the identification of the P^*-wave as the second phase in larger distances is rather difficult. This corresponds to the fact that the basaltic layer is thicker in the mountain area of the central part of Honshu than in the district of Shikoku and Kii Peninsula. In the next, the phases of S-group are less identifiable than the corresponding ones of P-group, especially in the cases of S^* and S_n. By the method of least squares, the velocities of each phase are calculated as follows.

	The Daishoji-Oki Earthquake	The Tokushima Earthquake
$\bar{P}$	5.9 km/sec	5.7 km/sec
P^*	6.9	7.0
P_n	8.0	7.9
S	3.4	3.3
S^*	4.0	4.0
S_n	4.7	4.6

After these preliminary investigations the parts of the seismograms between P- and S-waves are studied in detail. In such part, the displacement traced at any observation station is usually much complicated in appearance. It is found, however, that the several pulses recur successively in about equal time interval. The arrival times of these successive phases are tabulated in Tables I and II, and are plotted against the epicentral distance in Figs. 2 and 3. The typical examples of such records are shown in Figs. 4, 5, 6, 7, 8, 9 and 10. These are recorded at stations of epicentral distances of 265 km, 419 km, 552 km and 647 km in the case of the Daishoji-Oki Earthquake, and 256 km, 291 km and 536 km in the case of the Tokushima Earthquake respectively. Connecting these phases from station to station continuously, the curves of R_1, R_2, R_3, etc. are drawn. Then, (1) their apparent velocities have the values between those of the $\bar{P}$ and P_n and (2) they appear successively in about equal time interval after the direct P-wave. From these facts, they should be interpreted to be the multiple reflections of P-wave between the earth's outer surface and the Mohorovičić discontinuity. Moreover, the time intervals between them are about from 7 sec to

10 sec in the Daishoji-Oki Earthquake and from 5 sec to 7 sec in the Tokushima Earthquake. These values show their clear dependence on the crustal thickness of each region through which the multiple reflected waves are transmitted. The former value corresponds to the thickness of about 40 km and the latter to the 30 km, respectively.

In general the seismic wave impinging upon the discontinuity surface generates the reflected and refracted waves and suffers the change of type from P to S or *vice versa*. Then, in the records of near earthquake, there can be a large number of phases theoretically. But the change of type at the interface involving the Mohorovičić discontinuity usually causes considerable diminishing of amplitudes except the case at the free surface (**1**, **15**, **16**, **17**). Therefore the composite waves which suffer the change of type at the internal discontinuity encountered may be left out of consideration. The multiple reflections between the outer free surface and the g–b discontinuity (between granitic layer and basaltic layer) have no need to be considered, because they arrive much earlier and have smaller amplitude than the phases discussed in the present study. But it may not be distinguishable in the point of arrival time and amplitude, whether the wave starts initially upward to the outer free surface or downward to the base reflector. Taking account of these conditions, the number of phases to be observable is fairly reducible. In order to verify the above-mentioned identification from the travel time, the amplitude investigation should be made in addition.

b) *Amplitude- and period-relation*

As mentioned earlier, in the records of near earthquakes many phases may be identifiable. But there is frequently much ambiguity in their identifications owing to the scattering or clustering of plotted points in the travel time–distance graph. In order to avoid such arbitrariness, it is desirable that the data of as many stations as possible be available and besides, the changes of amplitude, period, wave form, etc. with epicentral distance which may characterize these phases, be investigated concurrently. Then they can be connected continuously from station to station and their reliability will be increased. For this purpose, it was favourable that the seismographs equipped at the stations concerned in the present study are all of the same type except a few (Tokushima, Hamamatsu and Matsuyama), that is, the small Wiechert seismograph which has the following constants.

Component	Weight of mass	Magnification	Period	Damping ratio
Horizontal	200 kg	60～100	4～5 sec	5～7
Vertical	80 kg	50～ 80	4～5 sec	5～7

In the following study of amplitude, the vertical component is mainly studied, because it contains theoretically the waves of P- and SV-types only. On the other hand, in the horizontal component the polarization and azimuth of station as seen from the epicenter must be considered in addition. Observed values are tabulated in Tables III and IV.

Table III. Observed amplitude of each phase (vertical component) of the Daishoji-Oki Earthquake. Station numbers are shown in Fig. 1.

No.	Station	Δ	Amplitude						
			P_n	$\bar{P}$	R_1	R_2	R_3	R_4	$\bar{S}$
		km	μ	μ	μ	μ	μ	μ	μ
	Kanazawa	45		700					
14	Hikone	133		449					
12	Nagoya	161	135	405					
6	Nagano	180	62	402					
	Kameyama	182		457					
18	Osaka	211		336					
19	Kobe	219	110	193	131	56	65		280
	Kofu	230	33						
10	Shizuoka	260	69	136	118	80	89		—
23	Sumoto	265	30	125	198	75	63		262
20	Owashi	267	23						
9	Mishima	289	29	122	108	70	110		396
5	Kumagaya	289	28	142	94	175	163		181
4	Utsunomiya	328	10	100	72	123	123		460
8	Yokohama	332	22	110					
7	Tokyo	332	50	156	81	148	173		425
27	Hiroshima	419	15	103	35	21	40	28	256
26	Matsuyama	426	16						
28	Oita	552	17	91		91	56	60	212
29	Fukuoka	621	10	55		30	25	25	225
30	Kumamoto	647	15	42		26	38	26	122

In Figs. 11 and 12, the amplitude of each phase is plotted against the epicentral distance. The points are rather scattered. This may be due to the emission mechanism at the origin, the locality of each station, the instrumental effect, etc. Then, especially the amplitudes of $\bar{P}$ and P_n are taken up and they are adjusted to the mean curves respectively, and the other phases are plotted according to such adjustment.

On the other hand, the theoretical calculation is made under the following assumptions and the result is shown in Fig. 13.

1) The crustal structure as shown in the previous paper (I) is used and the origin is situated at depth of 20 km (**14**).

2) At the origin, the equal energy is emitted in all directions.

3) The reflection and refraction coefficients of waves at each discontinuity are calculated as for plane waves (**16, 18, 19, 20,21, 22**).

4) Divergence effect of spreading of waves and absorption effect due to the crustal structure are neglected.

The dominant factors in the calculation are the reflection coefficients at both the free surface and the Mohorovičić discontinuity as the upper and lower boundaries. And the refractions at the interfaces elsewhere have scarcely any influence upon the calculated values.

Comparing the observed and calculated curves, we see that they are generally in good accordance with each other. It is found that as the number of multiple increases, the amplitude curves of respective phases have its own peak successively

Table IV. Observed amplitude of each phase (vertical component) of the Tokushima Earthquake. Station numbers are shown in Fig. 1.

No.	Station	Δ	Amplitude								
			P_n	$\bar{P}$	R_1	R_2	R_3	R_4	R_5	R_6	$\bar{S}$
		km	μ	μ	μ	μ	μ	μ	μ	μ	μ
	Muroto	57		700							
25	Takamatsu	67		460							645
	Kochi	74		328							
23	Sumoto	87	109	—							–
21	Shionomisaki	141	107	175	315	64					452
26	Matsuyama	141	100	173	168	171	75				268
17	Abuyama	171	40	140							410
20	Owashi	180	44	152		57					272
27	Hiroshima	185	33	172	120	100	71				380
15	Kamigamo	198	15	140	100	144					331
	Toyooka	200	28								
	Kameyama	234	38								
	Hamada	243	3								
14	Hikone	247	20	67		53	87				430
28	Oita	256	20	123		90	94	185			400
12	Nagoya	291	20	73			52	20	47		434
13	Gifu	291	—	50		60	28	50	68		280
32	Miyazaki	326	3	17							110
30	Kumamoto	350	4	55			26	22		22	129
29	Fukuoka	363	12	50							
10	Shizuoka	400	9	27			23		21		192
31	Kagoshima	426	2	12			35	27		42	92
9	Mishima	452	6	36			21	17		25	64
5	Kumagaya	536	5	17				18	17	15	285

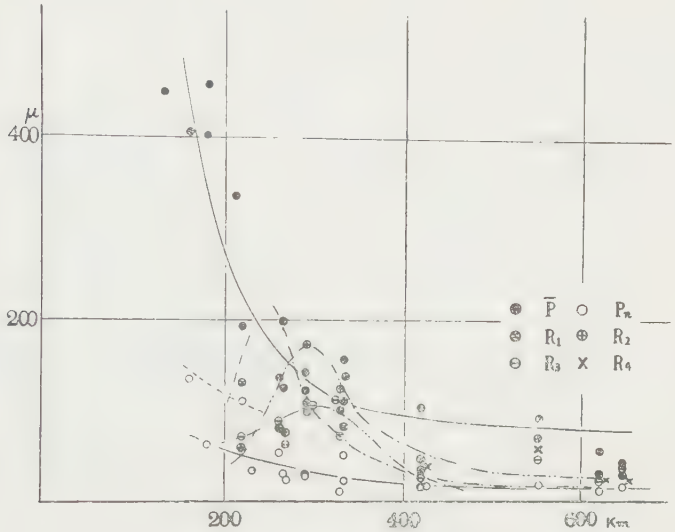

Fig. 11. Observed amplitude-distance graph (vertical component) of the Daishoji-Oki Earthquake.

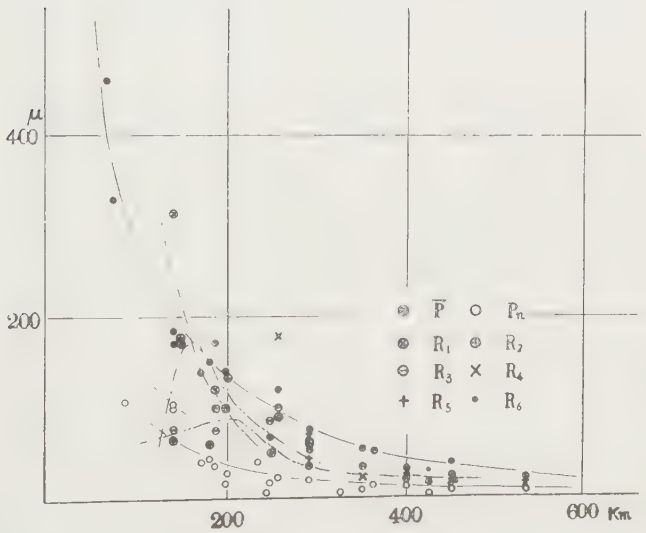

Fig. 12. Observed amplitude-distance graph (vertical component) of the Tokushima Earthquake.

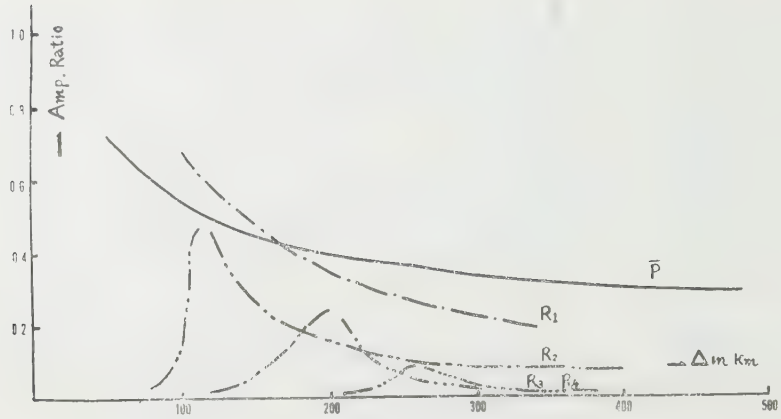

Fig. 13 Theoretical amplitude–distance graph (vertical component).

in the particular distance and their maximum value sometimes exceeds the value of direct *P*–wave. In the case of the Daishoji-Oki Earthquake, this is clearly shown in Fig. 4 recorded at Sumoto (Δ=265 km). At that distance, the large phase of R_1 follows the direct *P*–wave.

In the case of the Daishoji-Oki Earthquake, the later phases, R_3 and R_4, and in the case of the Tokushima Earthquake, R_3, R_4, R_5 and R_6 prevail over a wider range of distance, and moreover, their periods are longer than those earlier all over the range concerned as shown in Figs. 11 and 12. Their periods are likely those of the *S*–group.

Continuing to trace the amplitude variation beyond about 500 km, the periods of the direct *P*–wave and the successive phases in the following part become longer and longer one after another forming a wave train in a beat-like form, as shown in Figs. 7 and 10. Relating to these points, Gutenberg suggested that the direct *P*–wave at distances greater than about 100 km is the channel wave through the low–velocity layer (**23**). Further study about these points will be necessary.

3. Some considerations

In the seismic prospecting, the multiple reflections drew attention since early days. They are frequently too prevalent to overshadow the deep reflections, and the incorrect interpretation about them leads to the existence of the false reflector. Then an attempt to eliminate them is made and on the other hand, in order to identify them as the multiple reflection phase, the time interval between them, the move-out anomaly, the phase reversal, etc. are discussed in detail (**24**, **25**, **26**, **27**, **28**, **29**, **30**, **31**, **32**, **33**, **34**). And it is to be noted that their energies remain sufficiently strong to be recordable at surface after numerous multiple reflections. In the case of the present

study, it is also recognized that especially in the higher multiples, their amplitudes are too large relative to that of the direct *P*–wave. As mentioned above, the main effects ruling their amplitudes are theoretically in the reflection at the outer free surface and the Mohorovičić discontinuity of the base reflecting surface. But in reference to this point, the effects of the sedimentary layer as the low velocity contrast of the upper boundary may be considered to be likely those of the weathering layer in the seismic prospecting. Or, as in the marine survey, some sort of wave guide mechanism involving multiple reflection may be possible, and reinforcement by the constructive interference will also be suggestionable (**35**, **36**, **37**, **38**, **39**).

It is, however, one reasonable explanation for the anomalously large amplitude that the multiple reflections considered in the present study may be derived from the initially *S*–wave which is converted from *S* to *P* at the outer free surface. The considerable retardation of the travel times as a whole, namely from 5 to 10 sec in the present case (cf. Figs. 2 and 3) will then be also explained.

4. Summary

Generally speaking, in shallow earthquake's record, the part between the initial *P*-motion and the principal *S*–motion is much more complicated than in deep earthquake's record. Considering the path along which the seismic waves are transmitted, the cause of this complexity is the complex structure of the earth's crust.

In the present study, two shallow earthquakes are selected and their seismograms recorded at 32 stations in the distance range from about 100 km to 600 km are studied concurrently. The various phases in the part from the initial *P*–motion to the principal *S*–motion are traced not only in their travel time but also in amplitude and period. Then the repetitive features of pulses in about equal time interval are interpreted as the multiple reflections between the outer free surface and the Mohorovičić discontinuity.

It was found especially that the difference of the time interval in the two cases of the selected earthquake, corresponds to the local difference of the thickness of the crust through which they are transmitted. Moreover, the identification of these multiple reflections is verified by the amplitude– and period–distance relations. On the amplitude and period variation with distance, more precise measurements are desirable which will offer the more interesting informations about the earth's crust.

Acknowledgments

The writer wishes to express his hearty thanks to Prof. E. Nishimura for his kind guidance and encouragement throughout the present study. The writer is also indebted to the directors and members of the Japan Meteorological Agency concerned in this study for their generous permission for copying seismograms recorded at their

observatories. The cost of the present study was partly defrayed by a grant-in-aid for scientific research of the Ministry of Education.

REFERENCES

1. H. JEFFREYS, *The Earth*, (3rd ed., Cambridge University Press, 1952).
2. K. E. BULLEN, *An Introduction to the Theory of Seismology*, (2nd ed., Cambridge University Press, 1953).
3. K. SAGISAKA and M. TAKEHANA, On the surface reflections in near earthquake, Kenshin-Ziho, **8** (1935), 53–74 (in Japanese).
4. V. CONRAD, Das Schwadorfer Beben vom 8. Oktober 1927, Gerl. Beitr. z. Geophys., **20** (1928), 240–277.
5. B. GUTENBERG, Travel time curves at small distances, and wave velocities in Southern California, *ibid.*, **35** (1932), 16–50.
6. T. UTSU, Some remarkable phases on seismograms of near earthquakes (Part I), Kenshin-Ziho, **20** (1956), 13–16 (in Japanese).
7. T. MATUZAWA und T. FUKUTOMI, Zwei merkwürdige Wellengruppen bei einigen Erdbeben in Kantô und die dritte Mitteilung über den vorlaufenden Teil der Erdbebenbewegungen, Bull. Earthq. Res. Inst., **10** (1932), 499–516.
8. P. L. WILLMORE, A. L. HALES and P. G. GANE, A seismic investigation of crustal structure in the Western Transvaal, Bull. Seism. Soc. America, **42** (1952), 53–80.
9. E. R. LAPWOOD, Study of a series of Japanese earthquakes, Mon. Not. Roy. Astr. Soc., Geophys. Suppl., **7** (1955), 135–146.
10. The Seismological Bulletin for March, 1952, (The Central Meteorological Observatory, Tokyo, Japan, 1952).
11. The Seismological Bulletin for July, 1955, (The Central Meteorological Observatory, Tokyo, Japan, 1955).
12. Y. KISHIMOTO, Seismometric investigation of the earth's interior, Part I. On the structure of the earth's upper layer, Mem. Coll. Sci., Kyoto Univ., A, **27** (1954), 125–143.
13. ———, Ditto, Part II. On the structure of the earth's crust, *ibid.*, A, **27** (1955), 243–288.
14. A. KAMITSUKI, On the seismic waves reflected at the Mohorovičić discontinuity (I), *ibid.*, A, **28** (1956), 143–159.
15. H. JEFFREYS, Reflexion and refraction of elastic waves, Mon. Not. Roy. Astr. Soc., Geophys. Suppl., **1** (1926), 321–334.
16. B. GUTENBERG, Energy ratio of reflected and refracted seismic waves, Bull. Seism. Soc. America, **34** (1944), 85–102.
17. ———, Reflected and minor phases in records of near-by earthquakes in Southern California, *ibid.*, **34** (1944), 137–160.
18. H. KAWASUMI and T. SUZUKI, Reflection and refraction of seismic waves at plane interface of the earth's crust, Zisin, **4** (1932), 277–307 (in Japanese).
19. M. MUSKAT and M. W. MERES, Reflection and transmission coefficients for plane waves in elastic media, Geophysics **5** (1940), 115–148.
20. L. B. SLICHTER and V. G. GABRIEL, Studies in reflected seismic waves, Gerl. Beitr. z. Geophys., **38** (1933), 228–256.
21. T. MATUZAWA, An example of surface reflection of elastic plane waves, Zisin, **4** (1932), 7–12 (in Japanese).
22. L. KNOPOFF, R. W. FREDRICKS, A. F. GANGI and L. D. PORTER, Surface amplitudes of reflected body waves, Geophysics, **22** (1957), 842–847.
23. B. GUTENBERG, Revised travel times in Southern California, Bull. Seism. Soc. America, **41** (1951), 143–163.

24. L. Don Leet, Some Phases on explosion records in a 3-layered region, Gerl. Beitr. z. Geophys., **42** (1934), 246 251.
25. ———, Trial travel times for Northern America, Bull. Seism. Soc. America, **31** (1941), 325 334.
26. T. P. Ellsworth, Multiple reflections, Geophysics, **13** (1948), 1–18.
27. Curtis H. Johnson, Remarks regarding multiple reflections, *ibid.*, **13** (1948), 19 26.
28. John Sloat, Identification of echo reflections, *ibid.*, **13** (1948), 27 35.
29. B. Gutenberg and C. Y. Fu, Remarks on multiple reflections, *ibid.*, **13** (1948), 45 48.
30. Raul F. Hansen, Multiple reflections of seismic energy, *ibid.*, **13** (1948), 58 85.
31. Arne Junger, Deep basement reflections in Big Horn County, Montana, *ibid.*, **16** (1951), 499 505.
32. Thos. C. Poulter and Leonard V. Lombardi, Multiple reflections on the Edwards Plateau, *ibid.*, **17** (1952), 107–115.
33. M. Tatsugami, On the multiple reflections in Ariake District, Butsuri-Tanko, 8 (1955), 1–8 (in Japanese).
34. Glen H. Swenumson, Geophysical case history of the Anderson Ranch Field, Lea County, New Mexico, Geophysics, **22** (1957), 870 886.
35. K. E. Burg, M. Ewing, F. Press and E. T. Stulken, A seismic wave guide phenomenon, *ibid.*, **16** (1951), 594–612.
36. George P. Sarrafian, A marine seismic model, *ibid.*, **21** (1956), 320–336.
37. M. Ewing and F. Press, *Surface Waves and Guided Waves*, *Handbuch der Physik* (Springer-Verlag, 1957) Bd. 47, 119 139.
38. B. Gutenberg, Channel waves in the earth's crust, Geophysics, **20** (1955), 283 294.
39. F. Press and B. Gutenberg, Channel *P* waves *Πg* in the earth's crust, Trans. Amer. Geophys. Union, **37** (1956), 754 756.

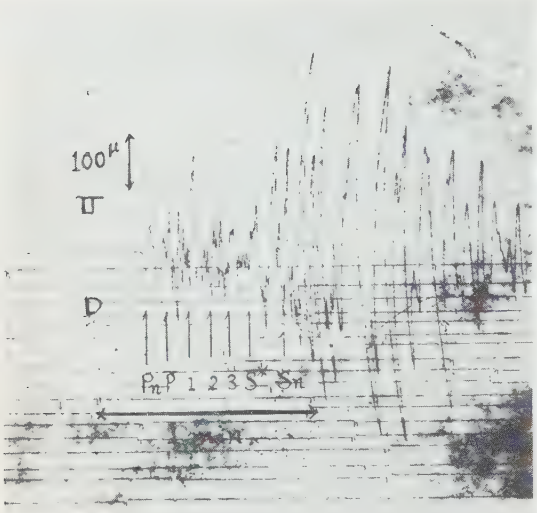

Fig. 4. Vertical Wiechert-seismogram, the Daishoji-Oki Earthqurke, Sumoto (Δ=265 km). (By the courtesy of the Sumoto Meteorological Observatory)

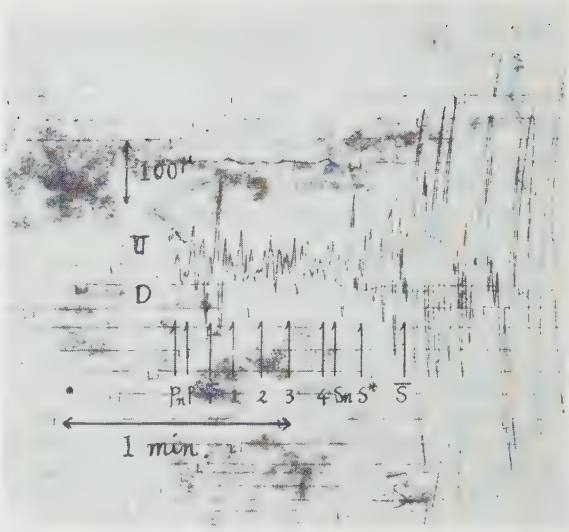

Fig. 5. Vertical Wiechert-seismogram, the Daishoji-Oki Earthquake, Hiroshima (Δ=419 km). (By the courtesy of the Hiroshima Meteorological Observatory)

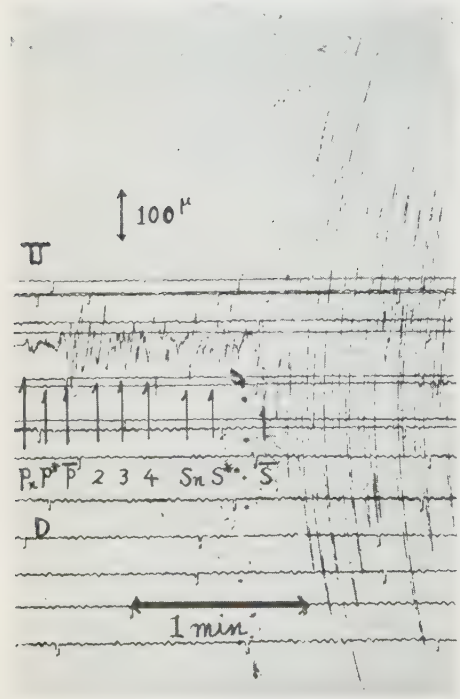

Fig. 6. Vertical Wiechert-seismogram, the Daishoji-Oki Earthquake, Oita (Δ=552 km). (By the courtesy of the Oita Meteorological Observatory)

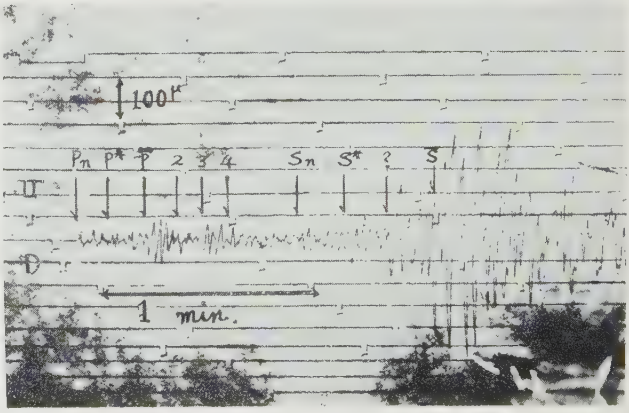

Fig. 7. Vertical Wiechert-seismogram, the Daishoji-Oki Earthquake, Kumamoto (Δ=647 km). (By the courtesy of the Kumamoto Meteorological Observatory)

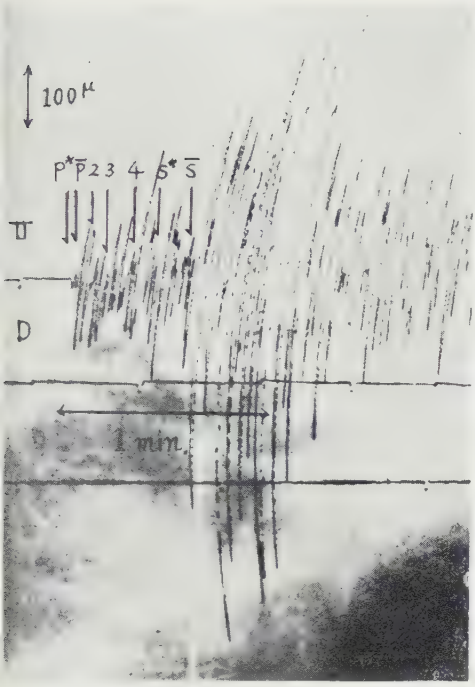

Fig. 8. Vertical Wiechert-seismogram, the Tokushima Earthquake, Oita (Δ=256 km). (By the courtesy of the Oita Meteorological Observatory)

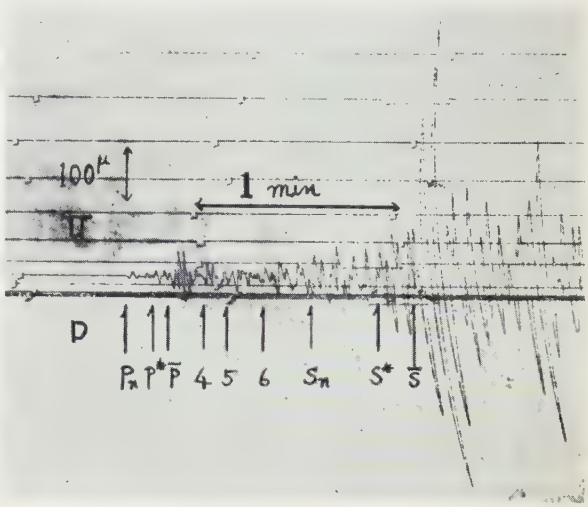

Fig. 10. Vertical Wiechert-seismogram, the Tokushima Earthquake, Kumagaya (Δ=536 km). (By the courtesy of the Kumagaya Meteorological Observatory)

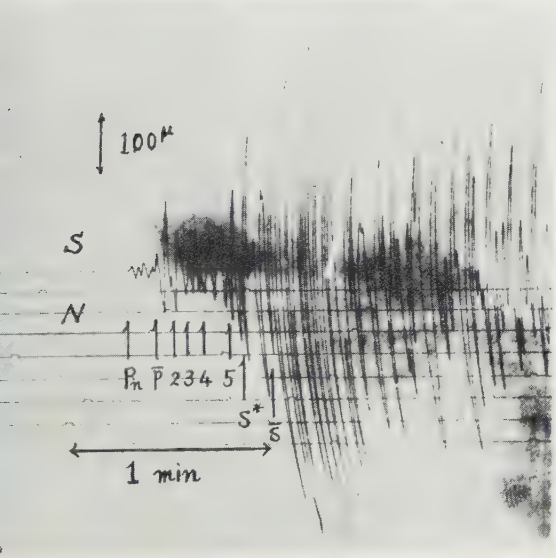

Fig. 9 a. Horizontal Wiechert-seismogram, the Tokushima Earthquake, Gifu (Δ=291 km). (By the courtesy of the Gifu Meteorological Observatory)

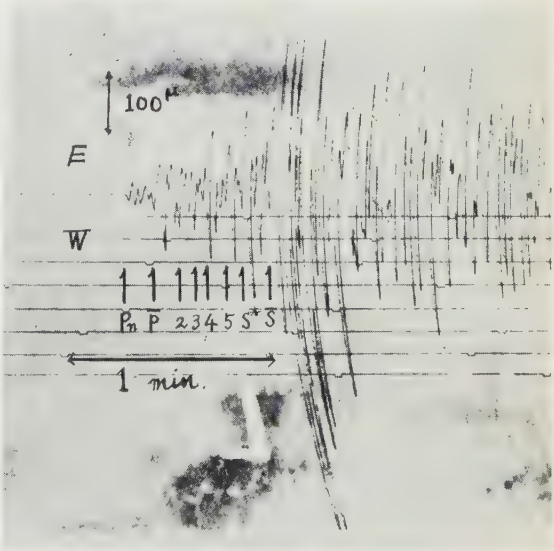

Fig. 9 b. Horizontal Wiechert-seismogram, the Tokushima Earthquake, Gifu (Δ=291 km). (By the courtesy of the Gifu Meteorological Observatory)

Memoirs of the College of Science, University of Kyoto, Series A,
Vol. XXIX, No. 1, Article 3, 1958.

ON THE MATERIALS IN THE EARTH'S MANTLE

BY

Teruo NISHITAKE

(*Received March 20, 1958*)

ABSTRACT

Several figures of the stony portion of stony meteorites are discussed in point of elastic property as compared with the figure of the mantle.

After the conclusion that there is no ground to assume that the stony portion of meteorites is the constituent material in the mantle, it is considered that, as previously discussed, dunite is the most probable material as the constituent of the mantle.

1. Introduction

Owing to a rapid advance in geophysics, the problem of what material the Earth's mantle is composed has recently become more and more important for every branch of Earth Science. With regard to radioactivity, thermal conduction, plasticity, and rupture phenomena in the Earth's mantle, for example, no definite conclusion could be drawn without knowledge of the material which exists in the mantle. Information about the material below the crust is necessarily indirect, and it is impossible to reach a conclusion unless some restriction is placed on speculation. Chemistry on rocks, meteorites and solar atmosphere will also be able to reveal the restriction about the material in the mantle. Our present knowledge of the Earth's interior, however, is mainly confined to the physical properties—seismic waves, density, moment of inertia, etc. Then, it is more natural to draw a definite conclusion that physical properties of rocks and meteorites constitute a conclusive factor. In this paper, the elastic property of stony meteorites and the variation of elasticity with metallic contents will be compared with that of the mantle by means of high pressure experiments.

2. Statistical analysis of stony meteorites

The study on chemical analysis of meteorites began a long time ago, and the data of the field of this branch have been accumulated year after year. Several authors (**1**, **2**, **3**, **4**) have published interesting results as to the statistical consideration of the accumulated chemical analyses. But, there is no conclusive theory of meteorites derived from statistical chemical analyses. It is supposed that the reason is mainly due to scarcity of data. In the following, three models for stony meteorites are tentatively chosen.

i) *Model A.* Recently Urey (**4**) has chosen 94 superior analyses as being reliable representatives for chondrite meteorites. These Urey's chemical analyses are taken as model A.

ii) *Model B.* Owing to the weight of overlying materials, pressure in the Earth's interior is very high, and consequently the transition to a high pressure form would be plausible. Since the mineral in the Earth's interior would be transformed into jadeites or garnets under high pressure, the model of transformed feldspars in meteorites will be referred to as model B.

iii) *Model C.* Wahl (**3**) proposed an Earth's model and a meteorites' model. According to him, the Earth and mother body of meteorites are originally metals, and owing to oxidation both have turned into oxides (rocks). He has chosen the meteorites fitted in his figure. This model will be referred to as model C.

3. Physical property of the meteorites

In order to compare the physical quantities of the Earth's mantle with those of the stony portion of stony meteorites, the density, the bulk modulus, and the ratio of the bulk modulus to the density of the stony portion are calculated as follows. At first, the mineralogical compositions of the stony portion are calculated. Secondly, the density of the stony portion is calculated by the equation:

$$\rho = \frac{\sum \rho_i v_i}{\sum v_i}, \qquad (1)$$

where ρ_i and v_i are the density and volume for the ith mineral respectively. Thirdly, the bulk modulus k of the stony portion is derived from the equation:

$$\frac{1}{k} = \frac{\sum \kappa_i v_i}{\sum v_i}, \qquad (2)$$

where κ_i is the compressibility of the ith mineral. There are some doubts about calculation of mineralogical composition from its chemical analysis for rocks and meteorites, and so it is preferable to collect the mineralogical composition of the stony portion.

But data for measured mineralogical compositions of the stony portion are still rare and in the present paper the theoretical calculations of mineralogical composition are adopted.

There is little ambiguity about reliability of Eqs. (1) and (2). L. H. Adams (**5**) has pointed out that the accuracy of Eqs. (1) and (2) is very high and that error of calculation is within 2 per cent.

The density and the bulk modulus of the stony portion are not measured directly, because meteorites have a mosaic structure with iron, sulphide and stony portion.

It is necessary to obtain their densities and bulk modulus to calculate from suitable assumptions. At the present stage of the study on meteorites the above-mentioned method would offer a plausible one.

The outline of calculation of the density and the bulk modulus of the stony portion is just as above mentioned. The details are stated in the following.

Model A. Urey has chosen 94 superior analyses as being reliable representatives for chondrite meteorites. This figure is assigned as model A. Brown (**2**) also collected the data for both stony and iron meteorites. His figure is very similar to that by Urey. For statistical analysis, the 94 chemical compositions are placed as ascending series of free metal contents, at which the free metal contents range from 2 per cent to 27 per cent. The 94 analyses are grouped into 28 groups in arrangement of every one per cent metal content. Among these 28 groups, the groups which contain smaller than ten analyses are discarded, because of the scarcity of members in the group. There are five groups which contain more than ten analyses among 28 groups. For these five groups, the means of chemical analyses are taken, from which the density and the bulk modulus of the stony portion are derived.

From the five mean chemical analyses, the mineralogical compositions can be calculated by the method proposed by Wahl (**3**). In Table I, the mineralogical compositions for five mean chemical analyses thus obtained are shown.

The calculation of mineralogical compositions (norm) from chemical compositions for meteorites have some uncertainty, though for rocks the norm calculation is established. And so the accuracy of the data shown in Table I is still unjustified. But the mineralogical compositions of the stony portion of stony meteorites are very simple compared with those of rocks, and the above figure in Table I is not so much different from those of the means of actual mineralogical compositions.

The densities of the stony portion for the five groups are derived from Eq. (1). The densities thus obtained for the five groups are shown in Table II.

It should be noted that the density of the stony portion is free from sulphide, because this procedure comes from taking account of the Earth's mantle free from sulphides.

There is another method of calculation of the density of the stony portion of stony meteorites. The method will be adopted in the following in order to ascertain the limit of error of calculation of the density.

The actual density of stony meteorites consists of the weighted means of contribution of metal, sulphide and stony portion, because actual stony meteorites consist of metal, sulphide and stony portion. Then the density of the stony portion has a value which is obtained by subtracting the contribution of the both parts of metal and sulphides from the original. The density ρ of the stony portion is obtained from the equation :

Table I. Average mineral compositions of stony meteorites.

Mineral	Density[1] (g/cm^3)	Mean weight %				
		Group 1	Group 2	Group 3	Group 4	Group 5
$Na_2OAl_2O_36SiO_2$	2.62	8.09	7.82	7.97	7.92	7.02
$K_2OAl_2O_36SiO_2$	2.56	1.20	1.32	0.84	1.17	0.71
$CaOA_2O_32SiO_2$	2.76	0.82	2.31	2.79	0.33	2.30
$FeOSiO_2$	3.9	7.44	7.62	6.53	5.43	6.36
$FeOTiO_2$	4.75	0.38	0.27	0.15	0.27	0.27
$MnOSiO_2$	3.67	0.31	0.36	0.84	0.44	0.46
$CaOSiO_2$	3.33[2]	3.25	2.33	2.23	4.19	2.26
$MgOSiO_2$	3.19	17.71	17.63	15.76	17.68	21.20
$2FeOSiO_2$	4.07	14.45	14.47	14.62	9.96	8.63
$2MgOSiO_2$	3.21	31.76	30.45	32.09	29.02	26.07
$FeOCr_2O_3$	4.5	0.55	0.90	0.58	0.38	0.41
$3CaONa_2OP_2O_5$	3.10	0.65	0.21	0.62	0.64	0.48
Metal	7.7[3]	7.42	8.43	9.44	16.77	18.86
FeS	4.73[3]	5.40	5.92	6.12	5.38	5.10

Name of meteorites

Group 1. Bjnrbole, Chandakapur, Forksville, Lundsgard, Modoc, Moorleah, Rakovka, Rich Mountain, Tuan Tuc, Warbreccan.

Group 2. Baroti, Chantonnay, Girgenti, Grossliebenthal, MacKinney, Meuselbach, Perpeti, Saint Deniswestrem, Saratov, Shelburne, Strathmore, Tieschitz, Tourinnesla-Grosse, Varpaisjarvi, Wittekrantz.

Group 3. Coon Butte, Crumlin, Lanzenkirchen, Launton, Lesves, Lissa, Mezo-madaras, Narellan, Ojuelos Altos, Phuoc-binh, Prambachkirchen, Rangara, Saint Christophe, Saint Michel, Sazovice.

Group 4. Bowden, Estacado, Linum, Oakley, Phu-Long, Salt Lake City, Seldebourak, Suwahib, Tabor, Tanezrouft.

Group 5. Beaver Creek, Benld, Benoni, Cape Girardeau, Collescipoli, Cronstad, Ekeby, Elsinora, Gopalpur, Hessle, Khairpur, Khetri, Mount Browne, Olmedilla di Alarcon, Plantersville.

1) from Reference (**10**)
2) assumed as diopside
3) from Reference (**11**)

Table II. Average density of silicate portion of stony meteorites.

Mineral	Mean weight %				
	Group 1	Group 2	Group 3	Group 4	Group 5
Feldspars	11.60	13.37	13.75	12.09	12.23
Pyroxenes	33.36	32.94	30.22	35.98	40.20
Olivine	53.28	52.46	55.33	50.08	45.64
Chromite	0.63	1.05	0.69	0.49	0.54
Merrillite	0.74	0.24	0.74	0.82	0.63
Total	99.61	100.16	100.73	99.46	100.24
Metal content (%)	7.42	8.43	9.44	16.77	18.86
Density[1] (g/cm^3)	3.3_0	3.3_0	3.2_9	3.2_6	3.2_6

1) Density of silicate portion of stony meteorite (mean value)

$$\rho = \frac{100-c_M-c_S}{100\,\rho_0 - c_M\,\rho_M - c_S\,\rho_S}, \qquad (3)$$

where ρ_0 is the measured density of actual stony meteorites, and c_M, c_S, ρ_M and ρ_S are the volume percentage of metal portion, the volume percentage of sulphide portion, the density of metal portion and the density of sulphide portion respectively.

In Table III, the densities of the stony portion of stony meteorites for given groups are shown.

Table III.

Component	Density (g/cm^3)	Mean weight %				
		Group 1	Group 2	Group 3	Group 4	Group 5
Metal	7.7	7.42	8.43	9.44	16.77	18.86
FeS	4.73	5.40	5.92	6.12	5.38	5.10
Silicate		87.18	85.65	84.44	77.85	76.04
Measured density[1] (g/cm^3)		3.50	3.51	3.52	3.59	3.66
Density of silicate portion[2] (g/cm^3)		3.3_0	3.3_0	3.2_9	3.2_6	3.2_6
Density of silicate portion[3] (g/cm^3)		3.2_9	3.2_7	3.2_6	3.1_7	3.1_9

1) Density of stony meteorite (mean value)
2) Density from Table II.
3) Calculated density from Eq. (3) for comparison.

The densities in Table III offer the indication of the limit of error of densities calculated in Table II. The values obtained in Table III are all in good agreement with those in Table II within errors of about 3 per cent. Therefore, the figures shown in Table II will have an accuracy smaller than about 3 per cent. As seen in Tables II and III, the figures obtained in Table III are all smaller than those in Table II. This is no doubt due to porosity of actual meteorites.

The bulk modulus (incompressibility) of the stony portion is derived from Eq. (2).

Among the minerals found in stony meteorites, the compressibilities for almost all of them were measured. But a few are not measured yet, $3CaO \cdot Na_2O \cdot P_2O_5$, for example, and so for such materials calculations were made without them. Total amount of the materials for which the compressibility is still unknown does not exceed 1 per cent. In Table IV, the bulk modulus for the stony portion (without sulphide) is shown.

It should be noted that the error of calculated figures in Table IV will be within 5 per cent, because the error comes from the uncertainty of Eq. (2) and the unknown factor of compressibility which is not yet measured.

Model B. Owing to the weight of overlying materials, pressure in the Earth's mantle is extraordinarily large, and under such high pressure the transition of minerals

Table IV. Average elasticity of silicate portion of stony meteorites.

Mineral	κ [1] (10^{-13}C.G.S.)	Mean volume %				
		Group 1	Group 2	Group 3	Group 4	Group 5
$Na_2OAl_2O_36SiO_2$	19	11.75	11.48	11.77	12.73	11.44
$K_2OAl_2O_36SiO_2$	21	1.75	1.98	1.27	1.90	1.17
$CaOAl_2O_32SiO_2$	11	1.13	3.23	3.92	0.49	3.54
$FeOSiO_2$	10	7.26	7.52	6.47	5.87	6.95
$FeOTiO_2$	5.6	0.30	0.23	0.13	0.23	0.23
$MnOSiO_2$		0.30	0.36	0.88	0.52	0.52
$CaOSiO_2$	11	3.72	2.67	2.58	5.28	2.89
$MgOSiO_2$	10	21.11	21.25	19.09	23.33	28.41
$2FeOSiO_2$	9.1	13.74	13.69	13.89	10.30	9.07
$2MgOSiO_2$	7.9	37.64	36.53	38.70	38.10	34.71
$FeOCr_2O_3$		0.46	0.76	0.49	0.36	0.39
$3CaONa_2OP_2O_5$		0.79	0.26	0.78	0.85	0.65
κ (10^{-13}C.G.S.)		$10._4$	$10._4$	$10._3$	$10._5$	$10._4$
k/ρ (10^{11}C.G.S.)		2.9	2.9	2.9	2.9	2.9

1) from Reference (**10**)

Table V. Elasticity of the stony portion of stony meteorites in hypothetical high pressure form.

Mineral	Density (g/cm^3)	κ (10^{-13} C.G.S.)	Mean weight %				
			Group 1	Group 2	Group 3	Group 4	Group 5
$Na_2OAl_2O_34SiO_2$	3.33[1]	7.8[1]	8.17	7.80	8.00	8.93	7.80
$3CaOAl_2O_33SiO_2$	3.54[1]	6.3[1]	1.53	4.36	5.22	0.67	4.91
$3FeOAl_2O_33SiO_2$	4.16[1]	6.0[1]	—	—	0.15	5.02	—
$CaOSiO_2$	3.33	11	2.93	0.46	—	—	0.45
$FeOTiO_2$	4.75	5.6	0.44	0.32	0.18	5.02	0.36
$FeOCr_2O_3$	4.5		0.63	1.05	0.69	0.49	0.54
$MnOSiO_2$	3.67		0.35	0.42	1.00	0.57	0.61
$2FeOSiO_2$	4.07	9.1	14.73	14.45	14.73	10.82	9.47
$2MgOSiO_2$	3.21	7.9	31.82	30.47	32.42	31.90	28.90
$FeOSiO_2$	3.9	10	11.31	12.11	10.99	9.24	10.80
$MgOSiO_2$	3.19	10	26.95	27.84	26.65	30.02	35.97
$3CaONa_2OP_2O_3$	3.10		0.74	0.89	0.74	0.82	0.63
Density (g/cm^3)			3.4	3.4	3.4	3.4	3.4
κ (10^{-13}C.G.S.)			8.9	8.8	8.7	8.8	8.9
k/ρ (10^{+11}C.G.S.)			3.3	3.3	3.4	3.3	3.3

1) Reference (**12**)

will be undergone. Recent experiments (**6**) show that feldspars are transformed into jadeites and garnets in such case of high pressure. It is plausible that under high pressure, a part of the stony portion will be transformed into a high pressure form. If it happens, the figures in model A will lose their reliability. In model B, whole feldspars will be transformed into high pressure forms and other minerals still remain unchanged as in model A.

The method of calculation of both the density and the bulk modulus is the same except feldspars. In Table V, the bulk modulus of a hypothetical high pressure form of the stony portion is shown.

The limit of errors in the figures in Table V cannot be estimated because of uncertainty of the fundamental postulation.

Model C. Recently, Wahl (**3**) proposed an Earth's model and meteorites. According to him, the Earth and the mother body of meteorites consist originally of metals. Owing to oxidation, the planets are oxided gradually from their surface to deeper part. The planets become two-layer planets composed of oxides layer (rocks layer) and metal layer (core). According to him, it must be concluded that for meteorites the larger their metal content is, the smaller FeO content. He has chosen four representative groups for stony meteorites fitted with the figure. In Table VI, the ratio of the bulk modulus to the density of his figures is shown.

Table VI. Mineralogical composition; After W. Wahl.

Mineral	Density (g/cm^3)	κ [2] (10^{-13}C.G.S.)	Weight %			
			Sample 1	Sample 2[1]	Sample 3	Sample 4
$Na_2OAl_2O_3 6SiO_2$	2.62	19	5.72	9.92	7.18	8.14
$K_2OAl_2O_3 6SiO_2$	2.56	21	1.50	1.37	1.51	1.37
$CaOAl_2O_3 2SiO_2$	2.76	11	2.86	2.60	2.20	2.36
$FeOSiO_2$	3.9	10	0.13	8.71	8.23	0.04
$FeOTiO_2$	4.75	5.6	0.31	0.28	0.43	0.36
$MnOSiO_2$	3.67		0.41	0.60	0.59	0.06
$CaOSiO_2$	3.33	11	3.33	2.67	4.67	3.41
$MgOSiO_2$	3.19	10	0.18	19.53	26.93	83.20
$2FeOSiO_2$	4.07	9.1	37.98	16.40	11.68	—
$2MgOSiO_2$	3.21	7.9	46.06	36.30	34.55	—
$FeOCr_2O_3$	4.5		0.95	0.84	1.00	0.51
$3CaONa_2OP_2O_5$	3.1		0.58	0.74	1.03	—
SiO_2	2.6	27	—	—	—	0.53
Metal content %			5.54	9.08	17.16	25.60
k/ρ (10^{11}C.G.S.)			3.0	2.9	2.9	2.8

1) Mean value of 12 stony meteorites.
2) Reference (**10**)

To obtain the figure in Table VI, the employed procedure is exactly the same as those for model A, except the difference in mineralogical compositions.

4. Comparison with the Earth's mantle

Meteorites are only rocks which come from outside the Earth. Chemical properties of meteorites are studied in many respects and are shown similiar to those for rocks on the surface of the Earth. It is often said from this point of view that the Earth's mantle consists of materials very similar to the stony portion of stony meteorites. But little has been done of their elastic properties in comparison with the Earth's mantle. The physical properties of meteorites are only tools to compare with those of the mantle. In Table VII, are shown the values of the ratio of the bulk modulus to the density for models A, B, and C respectively, together with that in the mantle (**7**).

Table VII. Average k/ρ from models A, B and C together with that from seismic observation in the Earth's mantle.

	Model A	Model B	Model C	Mantle[1)]
$\frac{k}{\rho}$ (10^{11}C.G.S.)	29	33	29	36～37

1) from Reference (**6**)

The ratio of the bulk modulus to the density in the Earth's mantle can be calculated without introducing any assumptions about seismic wave velocities. In Table VII the said ratio at the surface of the mantle is given for comparison with the figures obtained in § 3.

As will be seen in Table VII, the ratios of the bulk modulus to the density of the stony portion of stony meteorites from models A, B and C are all smaller than that obtained from seismic observation.

If we assume that the ratio of the bulk modulus to the rigidity for meteorites is nearly 2, just as in the case of both rocks and the Earth's interior, the dilatational wave velocities for figures of models A, B and C are 7.1, 7.5 and 7.4 km/sec respectively. From seismic observation, it is shown that the dilatational wave velocity just below the so-called Mohorovičić discontinuity is nearly equal to 8.0 km/sec (**6**). The discrepancy will exceed the limit of error of calculation.

For figures of model A the discrepancy is very large, and so there is no ground to assume that the Earth's mantle consists of the minerals similar to those of meteorites.

Usually, minerals have very complex crustal lattice structure, and so occurrence of polymorphic transitions under high pressure are very plausible in the Earth's mantle.

In this sense, the figure of model B will be reasonable for the figures proposed in the mantle. As shown in Table VII, however, this figure of model B is qualitatively unsatisfactory.

It will be pointed out that if stony meteorites contained more sodium oxide and alumina, the figure of meteorites would be fitted with that in the Earth's mantle. For model C, the calculated figure is still lower than that in the Earth's mantle. It will be pointed out that FeO is too much to interpret the figure of meteorites as that of the mantle in this case.

With regard to the variation of elasticity of the stony portion with metallic contents, the variation is very small, as seen in tables, and there is no correlation of the existence of layers in the mantle with the variation of elasticity of the stony portion of meteorites with their metallic contents.

Adams (**8**) has pointed out that the Earth's mantle consists mailny of olivine and dunite. His figure fits the observational fact in the mantle with regard to seismic wave velocities. There is no ground for altering Adam's postulation for figures of meteorites.

5. Conclusion

Several models of figures of the stony portion of stony meteorites were taken for the sake of comparison with the figure in the Earth's mantle. Calculated bulk modulus, and the ratio of the bulk modulus to the density for the stony portion of stony meteorites cannot interpret the value in the mantle obtained from seismic observations. The present writer tried to examine physical properties of dunite in the previous paper (**9**) and confirmed that the mantle consists mainly of dunite. This assumption was ascertained also in the present paper.

Acknowledgment

The writer would like to express his sincere thanks to Professor E. Nishimura for his kind guidance and to Professor A. Harumoto for his kind advice.

REFERENCES

1. G. T. Prior, On the genetic relationships and classification of meteorites, Mineralog. Mag., **18** (1916), 26.
2. H. Brown and C. Patterson, The composition of meteoritic matter, I. The composition of the silicate phase of stony meteorites, J. Geol., **55** (1947), 405.
3. W. Wahl, The statement of chemical analyses of stony meteorites and the interpretation of the analyses in terms of minerals, Mineralog. Mag., **29** (1950), 416.
4. H. C. Urey and H. Craig, The composition of the stone meteorites and the origin of the meteorites, Geochimica Cosmochimica Acta, **4** (1953), 36.
5. L. H. Adams, *Internal Constitution of the Earth*, (edited by B. Gutenberg, 1951) Chap. 4, p. 60.
6. D. T. Griggs and G. C. Kenedy, A simple apparatus for high pressures and temperatures, Amer. J. Sci., **254** (1956), 722.
7. H. Jeffreys, The structure of the Earth down to the 20° discontinuity, Mon. Not. Roy. Astr. Soc. Geophys. Suppl., **4** (1937), 13.

8. L. H. Adams, The compressibility of fayalite and the velocity of elastic waves in peridotite with different iron-magnesium ratios, Beitr. Geophys., **31** (1931), 315.
9. T. Nishitake, Elastic properties of rocks with relation to the Earth's interior, Mem. Coll. Sci., Kyoto University, A, **28** (1956), 73–98.
10. F. Birch, J. F. Chairer and H. C. Spicer, *Handbook of Physical Constants*, Geol. Soc. America, Special Paper, No. 36 (1954).
11. Dana's *System of Mineralogy*, Vol. 1 (7th edit. John Wiley & Sons Inc., New York, 1946).
12. L. H. Adams, The elastic properties of certain basic rocks and their constituent minerals, Proc. Nat. Acad. Sci., **15** (1929), 713–724.

Memoirs of the College of Science, University of Kyoto, Series A,
Vol. XXIX, No. 1, Article 4, 1958.

ELASTICITY OF SOLIDS AT HIGH PRESSURE AND THE EARTH'S MANTLE

BY

Teruo NISHITAKE

(*Received June 9, 1958*)

ABSTRACT

Elasticity of solids under high pressure is calculated on both theoretical and experimental grounds. It is concluded that the calculated elasticities of dunite and MgO are in good agreement with those obtained from seismic data in the upper mantle and lower mantle respectively. There is some possibility of existence of low-velocity layer or constant-velocity layer just below the so-called Mohorovičić discontinuity and of admixture of metallic iron near the core boundary.

1. Introduction

As the measurement of elasticity of solids has been rapidly advanced, many interesting and valuable data on rock elasticity have been published. In Japan, A. Kubotera (**1**) and D. Shimozuru (**2**) measured velocities of both dilatational and rotational waves in rock samples by the transmission time of ultrasonic impulse. Recently, D. S. Hughes and his co-workers (**3**) have succeeded in measuring elastic wave velocities under variable pressure conditions. Under these circumstances, it is now possible to compare these data with those of the Earth's interior, together with a theoretical treatment. In the present paper, the theoretical extrapolation of high pressure experiments will be made on the basis of the theory of solids.

2. Rock-elasticity

The behaviour of elasticity of rocks under varying pressure is very complex, and the complexity is mainly due to their porosity. But at high pressure, the effect of porosity on elasticity of rocks becomes more and more trivial.

The effect of porosity on elasticity of rocks was studied in my previous paper (**4**), and in the present paper the following points will be emphasized.

A) Both the value of elastic waves and that of compressibility of rocks are exceedingly diverse for each rock-sample of the same kind, but at sufficiently high pressure these values are nearly the same for rocks of the same kind because of the diminution of porosity.

B) Both the velocity of elastic waves and compressibility of rocks are the unique

functions of their specific volume at sufficiently high pressure.

With regard to A), Birch (**5**) and Adams (**6**) have concluded from their rock-experiments that at high pressure both velocities of elastic waves and compressibility of rocks tend to the values obtained by averaging velocities and compressibilities of the minerals of which the rocks are composed.

With regard to B), the present writer has concluded from D. S. Hughes' experiment used in my previous paper (**4**) that at high pressure both velocities of elastic waves and compressibilities of rocks become asymptotically functions of their density, free from their temperature.

From the above two points, it is possible to apply the results of rock-experiments to the Earth's mantle, if the data at sufficiently high pressure on rock-experiments are used with suitable care.

It may, therefore, be concluded that in determining the pressure coefficient for both elastic wave velocity and compressibility in the range of high pressure, the use of a bulk modulus-density diagram is more natural and accurate than a direct application of a bulk modulus-pressure diagram with respect to the elimination of the effect of porosity. In Table I some elastic properties of various rocks from D. S. Hughes' experiments are shown, where the pressure coefficients of elasticity are obtained from the bulk modulus-density diagram as in my previous paper (**4**).

Table I. Elasticity of rocks and MgO at atmospheric pressure and at room temperature.

	Granite	Basalt	Dunite	MgO
V_p (km/sec)	6.0	7.0	8.0	—
k (10^{12} C.G.S.)	0.57	0.86	1.15	1.672
ρ (g/cm^3)	2.7	2.9	3.2	4.0
$\frac{dV_p}{dp}$ (km/sec/10^4 bars)	0.2	0.1	0.1 (0.09～0.14)	—
$\frac{dk}{dp}$ (C.G.S.)	6.6 (6～7)	5.7 (5～6.5)	4.5 (4～5)	4.2 (4～4.5)

References (**3**) and (**20**)

3. Elasticity of rocks and minerals at high pressure

In order to compare the elasticity of the Earth's mantle with that of rocks and minerals, the problem of what materials the Earth's mantle consists, has become a very important factor, and investigations were made in my previous paper (**7**), without reaching a definite conclusion yet. In the present paper, two cases are considered : One case is based upon an assumption that the Earth's mantle consists of dunite, while in the other we assume that the mantle consists of MgO (periclase).

A. *Case of dunite*

It is well known that the elasticity of dunite is nearly equal to that in the upper part of the upper mantle. Hence, whether the elasticity of dunite at very high pressure is still in good agreement with that of the deeper part of the Earth's mantle, is a very interesting subject. In the following, the elasticity of dunite at very high pressure will be obtained from a theoretical extrapolation.

Rocks and minerals are assumed to belong to ionic crystals, and a theoretical treatment of the elasticity of ionic crystals after Born and Mayer (8) will be applicable.

Taking a unit volume of any mineral, its internal energy E is obtained from summation of a Coulomb interaction and a closed shell interaction, as a function of volume:

$$\left.\begin{aligned} E &= -\frac{A}{v^{1/3}} + Be^{-\alpha v^{1/3}}, \\ v_0 &= 1, \end{aligned}\right\} \tag{1}$$

where A, B and α are constants and v is volume, suffix 0 denoting the value at zero pressure. Here a Van der Waals interaction is neglected.

Then from the thermodynamical relation, we obtain

$$p = -\frac{\partial E}{\partial v} = -\frac{1}{3}\left(Av^{-4/3} - B\alpha v^{-2/3}e^{-\alpha v^{1/3}}\right), \tag{2}$$

$$k = -v\frac{\partial p}{\partial v} = -\frac{1}{9}\left(4Av^{-4/3} - 2B\alpha v^{-2/3}e^{-\alpha v^{1/3}} - B\alpha^2 v^{-1/3}e^{-\alpha v^{1/3}}\right), \tag{3}$$

$$\frac{dk}{dp} = \frac{\frac{16}{3}Av^{-1/3} - \frac{4}{3}B\alpha v^{1/3}e^{-\alpha v^{1/3}} - B\alpha^2 v^{2/3}e^{-\alpha v^{1/3}} - \frac{1}{3}B\alpha^3 v e^{-\alpha v^{1/3}}}{4Av^{-1/3} - 2B\alpha v^{1/3}e^{-\alpha v^{1/3}} - B\alpha^2 v^{2/3}e^{-\alpha v^{1/3}}}, \tag{4}$$

where p and k are the pressure and the bulk modulus respectively.

At zero pressure, the following relations hold:

$$p = -\frac{1}{3}\left(A - B\alpha e^{-\alpha}\right) = 0, \tag{2'}$$

$$k = -\frac{1}{9}\left(4A - 2B\alpha e^{-\alpha} - B\alpha^2 e^{-\alpha}\right) = k_0, \tag{3'}$$

$$\frac{dk}{dp} = \frac{\frac{16}{3}A - \frac{4}{3}B\alpha e^{-\alpha} - B\alpha^2 e^{-\alpha} - \frac{1}{3}B\alpha^3 e^{-\alpha}}{4A - 2B\alpha e^{-\alpha} - B\alpha^2 e^{-\alpha}} = \left(\frac{dk}{dp}\right)_0. \tag{4'}$$

The values of k_0 and $\left(\frac{dk}{dp}\right)_0$ in the above equations (3′) and (4′) are obtained from rock experiments, so that unknown A, B and α can be determined. In Table II are shown the values of the elasticity of dunite at high pressure which have been calculated from Eqs. (2), (3) and (4) with the help of Eqs. (2′), (3′) and (4′).

Table II. Elasticity of dunite at high pressure (calculated from Eqs. (2), (3) and (4)).

v/v_0	1.0	0.9	0.8	0.7	0.6
ρ (g/cm^3)	3.2	3.5	4.0	4.5	5.3
p (10^4bars)	0	15	41.4	90	178
$\frac{dk}{dp}$	4.5	4.0	3.7	3.4	3.1
k (10^{12} C.G.S.)	1.15	1.8	2.82	4.5	7.4
$\frac{k}{\rho}$ (10^{11} C.G.S.)	3.6	5.1	7.1	9.8	13.9

B. *Case of MgO (periclase)*

Recently the present author and others have concluded that at very high pressure the decomposition of dunite into MgO and quartz is possible (**9**). The pressure at which the decomposition will occur is suggested as nearly 500,000 bars, and will correspond to that at the depth of nearly 1,000 km in the Earth. Therefore, the elasticity of MgO at high pressure will theoretically be discussed here, in order to compare the observed elasticity of the Earth's mantle with that of MgO.

Internal energy of MgO was determined by Mayer (**10**), and the Coulomb and Van der Waals terms obtained by him are adopted here, but the term of closed shell interaction is assumed to be different from that obtained by Mayer.

Internal energy of MgO per molecule is given by the equation:

$$E = -\left(\frac{A'}{r}+\frac{C'}{r^6}\right)+B_1e^{-\alpha' r}+B_2e^{-\sqrt{2}\alpha' r}, \tag{5}$$

where A', C', α', B_1 and B_2 are constants and r is the distance between the nearest neighbours. The first and second terms represent the Coulomb and Van der Waals term respectively, while the third and fourth represent the closed shell interactions between the nearest and second neighbours respectively.

Then from thermodynamic relation we get

$$p = -\left(\frac{A'}{3nr^4}+\frac{2C'}{nr^9}\right)+\frac{B_1}{3nr^2}\alpha' e^{-\alpha' r}+\frac{\sqrt{2}B_2}{3nr^2}\alpha' e^{-\sqrt{2}\alpha' r}, \tag{6}$$

$$k = -\frac{1}{9}\left(\frac{4A'}{nr^4}+\frac{54C'}{nr^9}\right)+\frac{1}{9}\frac{1}{nr^3}(2B_1\alpha' re^{-\alpha' r}+B_1\alpha'^2r^2e^{-\alpha' r}) + \frac{1}{9}\frac{1}{nr^3}(2\sqrt{2}B_2\alpha' re^{-\sqrt{2}\alpha' r}+2B_2\alpha'^2r^2e^{-\sqrt{2}\alpha' r}), \tag{7}$$

$$\frac{dk}{dp} = \left\{\frac{16A'}{3r}+\frac{162C'}{r^6}-\frac{4}{3}B_1\alpha' re^{-\alpha' r}-B_1\alpha'^2r^2e^{-\alpha' r}-\frac{B_1}{3}\alpha'^3r^3e^{-\alpha' r} -\frac{4\sqrt{2}}{3}B_2\alpha' re^{-\sqrt{2}\alpha' r}-2B_2\alpha'^2r^2e^{-\sqrt{2}\alpha' r}-\frac{2\sqrt{2}}{3}B_2\alpha'^3r^3e^{-\sqrt{2}\alpha' r}\right\} \div\left\{\frac{4A'}{r}+\frac{54C'}{r^6}-2B_1\alpha' re^{-\alpha' r}-B_1\alpha'^2r^2e^{-\alpha' r}-2\sqrt{2}B_2\alpha' re^{-\sqrt{2}\alpha' r}-2B_2\alpha'^2r^2e^{-\sqrt{2}\alpha' r}\right\}, \tag{8}$$

$$v = nr^3,$$

where v is the volume per molecule and n is a constant. At zero pressure, the above equations are written as

$$p = -\left(\frac{A'}{3nr_0^4}+\frac{2C'}{nr_0^9}\right)+\frac{B_1}{3nr_0^2}\alpha' e^{-\alpha' r_0}+\frac{\sqrt{2}B_2}{3nr_0^2}\alpha' e^{-\sqrt{2}\alpha' r_0}=0, \tag{6'}$$

$$k = -\frac{1}{9}\left(\frac{4A'}{nr_0^4}+\frac{54C'}{nr_0^9}\right)+\frac{1}{9}\frac{1}{nr_0^3}(2B_1\alpha' r_0 e^{-\alpha' r_0}+B_1\alpha'^2 r_0^2 e^{-\alpha' r_0})$$
$$\frac{1}{9}\frac{1}{nr^3}(2\sqrt{2}B_2\alpha' r_0 e^{-\sqrt{2}\alpha' r_0}+2B_2\alpha'^2 r_0^2 e^{-\alpha'\sqrt{2}r_0})$$
$$= k_0, \tag{7'}$$

$$\frac{dk}{dp} = \left\{\frac{16A'}{3r_0}+\frac{162C'}{r_0^6}-\frac{4}{3}B_1\alpha' r_0 e^{-\alpha' r_0}-B_1\alpha'^2 r_0^2 e^{-\alpha' r_0}-\frac{B_1}{3}\alpha'^3 r_0^3 e^{-\alpha' r_0}\right.$$
$$\left.-\frac{4\sqrt{2}}{3}B_2\alpha' r_0 e^{-\sqrt{2}\alpha' r_0}-2B_2\alpha'^2 r_0^2 e^{-\sqrt{2}\alpha' r_0}-\frac{2\sqrt{2}}{3}B_2\alpha'^3 r_0^3 e^{-\sqrt{2}\alpha' r_0}\right\}$$
$$\div\left\{\frac{4A'}{r_0}+\frac{54C'}{r_0^6}-2B_1\alpha' r_0 e^{-\alpha' r_0}-B_1\alpha'^2 r_0^2 e^{-\alpha' r_0}-2\sqrt{2}\frac{B_2}{3}\alpha' r_0 e^{-\sqrt{2}\alpha' r_0}-2B_2\alpha'^2 r_0^2 e^{-\sqrt{2}\alpha' r_0}\right\}$$
$$= \left(\frac{dk}{dp}\right)_1, \tag{8'}$$
$$v = nr^3 = 2r_0^3,$$

where r_0 is the distance between the nearest neighbours at zero pressure.

The right-hand sides of the above equations are all determined from high pressure experiments, so that the unknown α', B_1 and B_2 are obtained from the above simultaneous equations.

Table III. Elasticity of MgO at high pressure (calculated from Eqs. (6),(7) and (8)).

v/v_0	1.0	0.9	0.8	0.7	0.6
ρ (g/cm^3)	3.6	4.0	4.5	5.1	6.0
p (10^4bars)	0	22	60	127	247
$\frac{dk}{dp}$	4.2	3.8	3.5	3.2	3.0
k (10^{12} C.G.S.)	1.67	2.54	3.91	6.14	9.8
$\frac{k}{\rho}$ (10^{11} C.G.S.)	4.7	6.3	8.7	11.9	16.4

The elasticity of MgO at high pressure thus calculated is given in Table III. It should be noticed that in the above theoretical calculation dunite and MgO are assumed to be ionic crystals. Strictly speaking, this is not the case, and dunite and MgO contain some electron pair bonds. The nature of such electron pair bonds is still unknown and in the present paper the assumption is regarded to be correct in a first approximation.

4. Comparison of the calculated elasticity of dunite and MgO with those observed in the Earth's mantle.

Velocities of seismic waves in the Earth's mantle obtained by Jeffreys (**11**) and Gutenberg (**12**) are in good agreement except in low-velocity layer. The elasticity of the Earth's mantle is known exact enough to compare it with that of rocks at high pressure evaluated in § 4. In the following a discussion will be given, for convenience, in two parts, i.e., in the upper and lower mantle respectively.

1. *Upper mantle*

Both k/ρ obtained from seismic wave velocity in the Earth's mantle, where ρ denotes density, and that calculated in § 3, are shown in Fig. 1, where the data of pressure in the Earth's mantle are taken from Bullen's (**13**).

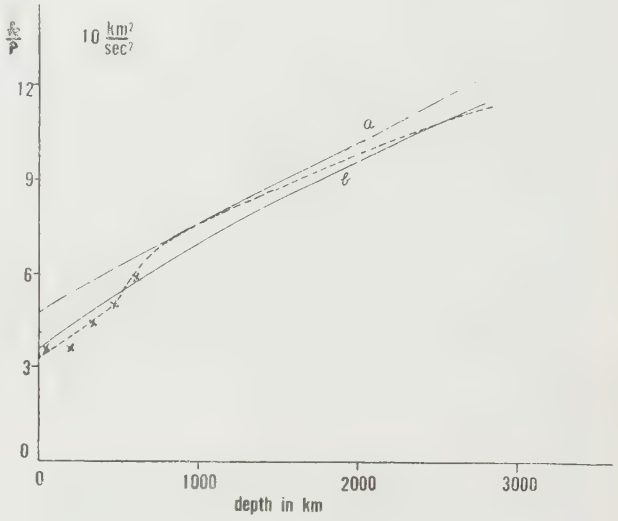

Fig. 1. Calculated elasticity of dunite and MgO
(a) : k/ρ of MgO, (b) : k/ρ of dunite
broken line : k/ρ of the Earth's mantle from seismic observation by Jeffreys (**11**)
$\times\times$: k/ρ by Gutenberg (**12**), abscissa being the depth in the Earth's mantle.

As seen in Fig. 1, the elasticity of dunite at high pressure is in good agreement with that from seismic data in the upper mantle. Especially increasing rate of the elasticity of dunite under high pressure is in very good agreement with that in the upper mantle, except in low-velocity layer.

From these relations, the effect of temperature and inhomogeneity in the upper mantle are considered small and the velocity increase in the upper mantle is regarded to be due mainly to compression with the overlying materials, except in low-velocity layer.

With regard to the region just below the so-called Mohorovičić discontinuity, temperature effects should not be neglected, because in this region temperature gradient is considered to be large. In order to make the temperature correction in this region, it is necessary to know the distribution of temperature in the upper mantle, but it is not yet accurately determined up to the present. Consequently a very simple correction due to temperature-effect will be given in the following. It is assumed in

a first approximation that the velocity of elastic wave in solids is a function of density alone, the relation being valid excepting the case when the temperature is near the melting point of the solids. If the relation is satisfied in the upper mantle, i.e., the temperature in the upper mantle is below the melting point of rocks, then a correction due to temperature-effect will be obtained simply.

The variations of elastic wave velocity (V_p) and the bulk modulus with increasing depth are given by the equations:

$$\frac{dV_p}{dh} = \frac{dV_p}{d\rho}\frac{d\rho}{dh} = \frac{dV_p}{d\rho}\frac{\rho_{h+\Delta h}-\rho_h}{\Delta h}, \tag{9}$$

$$\frac{dk}{dh} = \frac{dk}{d\rho}\frac{d\rho}{dh} = \frac{dk}{d\rho}\frac{\rho_{h+\Delta h}-\rho_h}{\Delta h}, \tag{10}$$

where ρ_h and $\rho_{h+\Delta h}$ are the densities at the depths of h and $h+\Delta h$ in the upper mantle respectively.

Then these equations are written in the forms:

$$\frac{dV_p}{dh} = \frac{dV_p}{d\rho}\left(\frac{\rho}{k}\Delta p - \beta\rho\Delta T\right)\Big/\Delta h, \tag{11}$$

$$\frac{dk}{dh} = \frac{dk}{d\rho}\left(\frac{\rho}{k}\Delta p - \beta\rho\Delta T\right)\Big/\Delta h, \tag{12}$$

where p, T and β are pressure, temperature and thermal expansion coefficient, at the depth of h, and Δp and ΔT are the pressure- and the temperature-differences between the depths of h and $h+\Delta h$.

If we assume $\frac{k}{\rho} = 35\,\mathrm{km^2/sec^2}$, $\beta = 4\cdot10^{-5}$ and $\frac{dV_p}{d\rho} = 6\,\mathrm{km/sec/g/cm^3}$ in this region, the variation of the velocity of dilatational wave with depth in the upper mantle is obtained, when the temperature distribution in the upper mantle is given.

In Table IV and Fig. 2 the the velocity of dilatational wave at various depths in the upper mantle is shown, where the temperature distribution is adopted from Gutenberg (**14**), Daly (**15**), and Jeffreys (**16**).

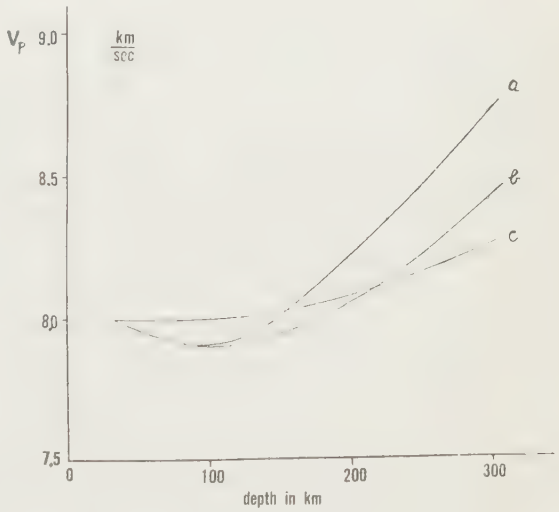

Fig. 2. Dilatational wave-velocity of dunite *versus* depth in the Earth's mantle.
Temperature distributions are after (a) Gutenberg, (b) Daly, and (c) Jeffreys respectively.

Table IV. Seismic wave velocity in the upper mantle.

	Dilatational wave velocity (km/sec)		
Depth (km)	A	B	C
30~50	8.0	8.0	8.0
100	<7.9	<7.9	8.0
200	8.1	8.3	8.15
300	8.5	8.8	8.3

Temperature distributions for models A, B and C are after Daly, Gutenberg and Jeffreys respectively.

The velocity at the depth of 30 km is assumed to be 8.0 km/sec as is seen in Fig. 2. At depths between 50 and 100 km, a low-velocity layer is obtained from Gutenberg's and Daly's temperature distribution and a constant-velocity layer from Jeffreys'. It will safely be concluded that the existence of a low-velocity layer or a constant-velocity layer is theoretically and observationally possible.

Needless to say, the present discussion is correct only in a rough approximation, and it contains ambiguity in the point of simplification. According to Born and others (**8**) the bulk modulus of solids is given in the form, $k=f(v)+g(v, T)$ where f and g are functions of volume alone, and of volume and temperature respectively. In the above procedure, the second term is neglected because of the assumption that the temperature in the upper mantle is below the melting point of rock. Near the melting point, elasticity of solids becomes very rapidly small. Recent experiments on the elasticity of solids below and above the melting point of solid show that temperature effect becomes suddenly large at the temperature very near the melting point. According to Birch (**17**) and Shimozuru (**18**), when $T/T_m \approx 0.95$, the effect of temperature becomes predominant, where T_m is the melting point of the solid. If the melting point of dunite is assumed to be 1,500°C, the effect of temperature will become very large above 1,400°C. But there is no evidence that temperature in the upper mantle is within 100°C lower than the melting point of rocks at the prevailing pressure in this region. Therefore the assumption in the above procedure is not far from the actual condition in the upper mantle. Moreover, if the second term is taken into account, temperature effect will be larger than that in the above discussion, and the existence of a low-velocity layer becomes more probable.

2. *Lower mantle*

As seen in Fig. 1, the elasticity of MgO is in good agreement with that in the Earth's lower mantle. The elasticity of dunite at high pressure is in good agreement with that in the Earth's upper mantle, but not in the lower mantle.

Recently, the present author and others pointed out that olivine will decompose into MgO and SiO_2 at very high pressure, and the coincidence of elasticity of MgO with that in the lower mantle supports this possibility. The elasticity of MgO at depths from 1,000 km to 3,000 km is especially in good agreement with that in the lower mantle. It was concluded in our previous paper (**9**) that the pressure at which the decomposition of olivine will occur corresponds to a depth of about 1,000 km. This previous estimation was ascertained also from the point of view of elastic property. Therefore, in this region of the lower mantle (at depths from 1,000 to 2,000 km), MgO is to be regarded as a main constituent mineral.

Below the depth of 2,000 km in the lower mantle, the elasticity of MgO is larger than that obtained from a seismic observation, as seen in Fig. 1. This fact will be explained as due to admixture of low velocity materials—metallic iron. If we assume that the constituent of the Earth's core is metallic iron and if the elasticity of a mixture is given by a weighted mean of elasticities of constituents, the difference between the elasticity of the core boundary observed from seismic waves and that of MgO at pressure corresponding to that depth, will be explained as due to an admixture of 10 per cent metallic iron in weight. But the propriety of theoretical extrapolation of elasticity of MgO to this depth in the lower mantle is considered questionable, and a definite conclusion must be postponed. A rapid development in experimental research in this field is earnestly desired.

5. Concluding remarks

1) The elasticity of dunite as calculated from the theory of solids is in good agreement with that observed in the Earth's upper mantle excepting the region just below the so-called Mohorovičić discontinuity.

2) Taking into account the effect of temperature, an existence of low-velocity layer or constant-velocity layer just below the crust is presumed to be probable.

3) The calculated elasticity of MgO is in good agreement with that in the region of depths from 1,000 to 2,000 km, and from this the existence of MgO in the lower mantle is considered to be probable.

4) Below the depth of 2,000 km in the lower mantle, an admixture of metallic iron is suggested as probable.

Acknowledgement

The author wishes to express his cordial thanks to Professor E. Nishimura in the Department of Geophysics for his kind guidance, and to Professor K. Sassa for his kind advice throughout the present study, and also to Professors K. Tomita in the Department of Physics and T. Yamamoto in the Department of Chemistry for their valuable information and advice on the theory of solids.

REFERENCES

1. A. KUBOTERA, J. Physics Earth, **2** (1954), 33.
2. D. SHIMOZURU, Bull. Earthq. Res. Inst., **30** (1952), 63.
3. D. S. HUGHES *et al.*, Geophysics, **16** (1951), 577; **21** (1956), 277; **22** (1957), 23.
4. T. NISHITAKE, Mem. Coll. Sci., Kyoto Univ. A, **28** (1957), 73.
5. F. BIRCH, Bull. Geol. Soc. America, **54** (1943), 263.
6. L. H. ADAMS and E. D. WILLIAMSON, J. Franklin Inst., **195** (1923).
7. T. NISHITAKE, Mem. Coll. Sci., Kyoto Univ., **29** (1958), 37.
8. M. BORN and J. E. MAYER, ZS f. Phys., **75** (1932), 1.
9. T. NISHITAKE *et al.*, Report of I.U.G.G. in Toronto (1957).
10. J. E. MAYER and M. McC MALTIBIE, ZS f. Phys., **75** (1932), 748.
11. H. JEFFREYS, *The Earth*, (Camb. Univ. Press, 1952).
12. B. GUTENBERG, Bull. Seis. Soc. America, **43** (1953) 223.
13. K. E. BULLEN, *An Introduction to Theory of Seismology*, (Camb. Univ. Press, 1952).
14. B. GUTENBERG, *Internal Constitution of the Earth*, (Dover Publication, 1951).
15. R. A. DALY, Bull. Geol. Soc. America, **54** (1943), 401.
16. H. JEFFREYS, loc. cit.
17. F. BIRCH, J. Chem. Phys., **8** (1940), 641.
18. D. SHIMOZURU, Bull. Earthq. Res. Inst., **34** (1956), 88.
19. J. E. MAYER and M. L. HUGGINS, J. Chem. Phys., **1** (1933), 643.
20. F. BIRCH *et al.*, *Handbook of Physical Constants*, Geol. Soc. America, Special Paper No. 36 (1954).

Memoirs of the College of Science, University of Kyoto, Series A,
Vol. XXIX, No. 1, Article 5, 1958.

PRECISE MEASUREMENT OF FREQUENCY SHIFT OF AMMONIA INVERSION SPECTRUM

BY

Masaru YAMANO

(*Received June 9, 1958*)

ABSTRACT

The shift of the center frequency of an ammonia inversion spectrum ($J=K=3$) was accurately measured, when the gas was pure ammonia and when some foreign gas was mixed, respectively. The value of a which is the ratio of frequency shift to $\Delta\nu_p$ (pressure broadening) was determined to be $(2.8 \pm 0.1)\times 10^{-2}$, the ratio of frequency shift to gas pressure to be (0.77 ± 0.02) Mc/mmHg, and the collision broadening parameter κ to be (27.5 ± 0.1) Mc/mmHg, when the ammonia purity is about 94% and the half-half width, $\Delta\nu = 350$ kc/s.

1. Introduction

Atomic clocks (**1**～**5**) of different types based on the constancy of the spectral frequency have been studied and constructed. Thus, the center frequency of the ammonia inversion spectrum had been considered to be accurately constant at sufficiently low pressures. It was, however, found in the course of research on the Stark modulation atomic clock (**5**) by the author and his coworkers, that the frequency given by this atomic clock does shift downward with the decrease in the ammonia gas pressure (**6**～**8**).

Then, the frequency given by the atomic clock was plotted *versus* the square of Stark electric field for various pressures of the ammonia gas, and the curves thus obtained all became very nearly parallel straight lines (Fig. 1). From this, the above frequency shift

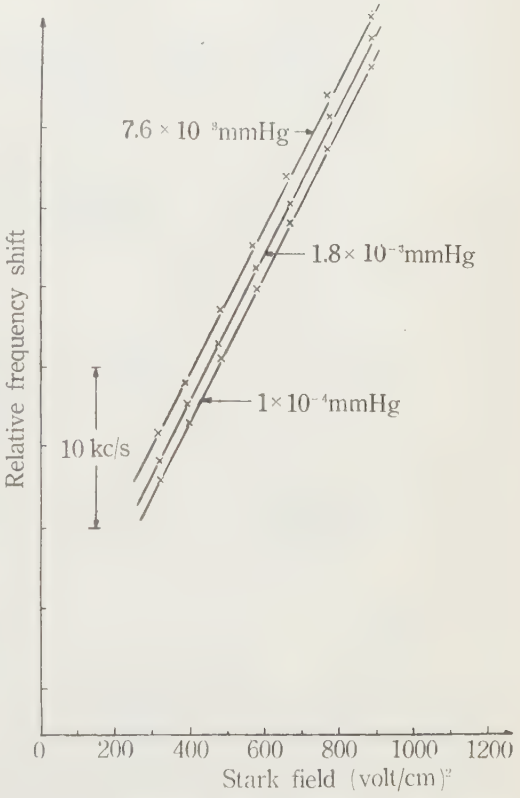

Fig. 1. Frequency *versus* square of Stark field intensity for various pressures.

can be ascribed to the shift of the center frequency of the used inversion spectrum. The measurement of the frequency shift was done about the pure ammonia and about the gas mixed with some foreign gas, respectively.

2. Experimental apparatus

For the measurement of the frequency shift and the half-half width $\Delta\nu$, a frequency comparator and a quartz chronometer (100 kc/s) were used. The former is a component of the atomic clock (Fig. 2) and illustrated in Fig. 3, and the latter has a stability better than 1×10^{-7}/day and an accuracy almost the same as the original accuracy (2×10^{-8}) of the JJY signal. In fact, the above quartz chronometer was calibrated by using the standard waves of 5 Mc/s from JJY. Though the radio waves reflected by the ionosphere are accompanied by the frequency shift (Doppler effect) caused by the movement of the ionosphere, the author has ascertained from his long time observation (**9**) that during daytime there occurs ordinarily no Doppler shift as large as 1×10^{-8} in the 5 Mc/s waves received in Kyoto.

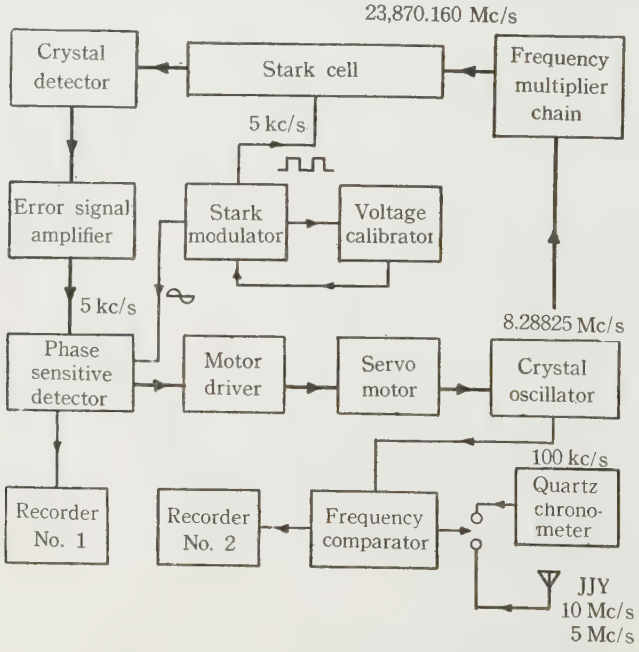

Fig. 2. Construction of the atomic clock.

The Stark cell consists of a brass X-band wave guide section 2 meter long and the absorption coefficient of the cell is about 1 db per foot. The Stark electrode is made of copper plate 0.5 mm thick and supported by teflon spacers (Fig. 4). Each end of the Stark cell is connected with a tapered section 20 cm long followed by a matching section and then by a ferrite uniguide, with a phase shifter between the

uniguide and the matching section on the output side of the cell. The phase shifter is used to test the matching of the microwave circuit. It has a voltage standing wave ratio within 1.11 at about 23,870 Mc/s and can shift the phase of the input microwave signal by more than $3/4\,\lambda_g$ (λ_g: guide wavelength).

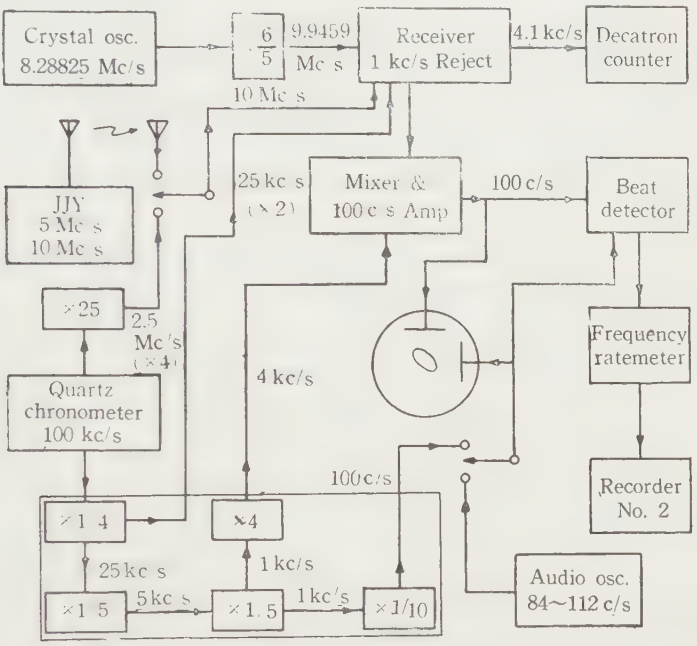

Fig. 3. Block diagram of the frequency comparator.

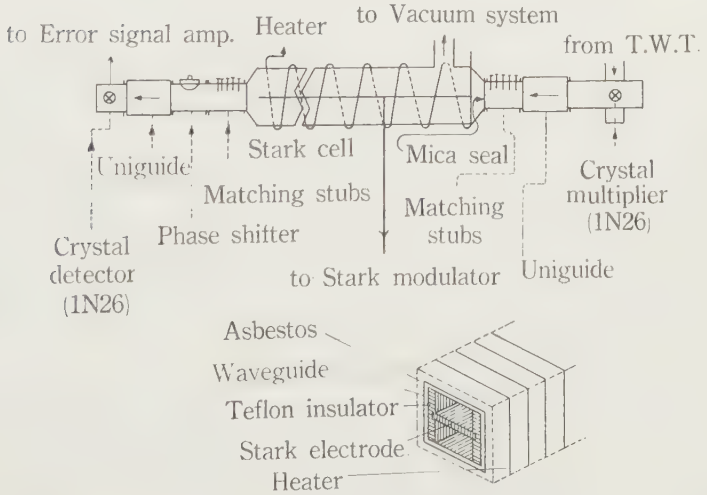

Fig. 4. Microwave circuit and cross section of Stark cell.

The input microwave to the Stark cell of the frequency 23,870 Mc/s is about 6 μW in power, too weak to cause saturation broadening (**11**) and is produced by frequency multipliers of various types from the crystal oscillator of the frequency 8.28825 Mc/s and has an enough signal to noise ratio, since it was ascertained by a beat measurement at 8,000 Mc/s with another crystal controlled frequency standard.

In order to keep the wall temperature of the Stark cell constant, a heating wire was wound on the outside of the cell through the whole length with asbestos sheets as separator, and a mercury thermostat was set at the center so as to contact tightly with the wider face. This is absolutely necessary:

(a) to be used when eliminating the substitution effect which is to be later described,

(b) to keep the pressure of ammonia constant because it changes due to the variation in the adsorption by the wall with the wall temperature even if the cell is completely outgased,

(c) to keep $\Delta\nu$ constant, since it may change with the gas temperature.

In the experiment, the cell wall was kept at the temperatures: 44.4, 40.8, 36.8, 31.9 $\pm$ 0.3°C.

The pressure measurement of the gas was done by using both Pirany gauge and vibration type quartz fiber pressure meter (**14**). The former is suitable for fast and continuous measurement but has zero point drift, while the latter takes more time for measurement (about 30 seconds at 4.2×10^{-3} mmHg) but has an absolute accuracy better than 5×10^{-2} in the pressure region about from 1×10^{-4} mmHg to 2×10^{-2} mmHg.

3. Experimental procedure

Before the measurement of the frequency shift, the calibration of the quartz chronometer has to be finished. Then, the ammonia gas is introduced into the Stark cell and set at the working pressure of about 2×10^{-3} mmHg and the matching of the microwave circuit is completed by means of two matching sections which have each five matching stubs. The five stubs on each side of the cell are adjusted to ensure that the frequency of the atomic clock does not vary with the phase change of the microwave. This is necessary to eliminate errors due to gas dispersion (**5**). The final accuracy of the atomic clock depends on this adjustment. When adjusting, the frequency is counted by the frequency comparator against the phase change artificially caused by the phase shifter.

The measurement of $\Delta\nu$ was carried out with the frequency control loop open, by changing manually the frequency of the crystal oscillator within 100 c/s at 8.28825 Mc/s to trace the two absorption curves (with and without Stark field).

By detecting the maximum points of the 5 kc/s error signal, the frequencies ν_m

and ν'_m of the maximum gradient of the curves can be determined.

$\Delta\nu$ is calculated from $\nu'_m - \nu_m$ (**6**) in this case when the modulation frequency is 5 kc/s and the sweep width is about 60 kc/s. The stability of the crystal oscillator of the atomic clock with the servo-loop open is better than 2×10^{-8} during one measurement which takes about 30 seconds. But the final accuracy of $\Delta\nu$ is limited by the signal to noise ratio of the frequency comparator and estimated to be 1×10^{-7} or 2.5 kc/s at 23,870 Mc/s.

The measurement of the shift of the center frequency was carried out by measuring the frequency ν_s (the frequency of the cross point of the two curves) by the frequency rate meter of the frequency comparator with the servo-loop closed.

4. Substitution of ammonia molecules

As reported before (**7, 8, 9**), the center frequency shifts downward for a few days after the introduction of the gas into the Stark cell. So the sample gas contained in the cell for 7 days was analyzed by means of mass-spectrometer and the result showed the remarkable decrease in the partial pressure of the ammonia gas (in an extreme case, from 94% to 20%). This fact corresponds to the substitution of ammonia molecules by foreign gas molecules contained in the cell wall and the frequency shift downward can partially be explained by the decrease in the partial pressure of ammonia gas.

The substitution, on the other hand, seems to occur connected with the adsorption (**11**) by, and the evaporation from, the cell wall at different temperatures.

In turn, the measurement of the frequency shift of ammonia spectrum is expected to give a means to investigate the adsorption character of a wall.

5. Frequency shift by self-broadening

To eliminate the substitution effect, the Stark cell was treated in the following way, before it was used. The cell was kept at the pressure of about 2×10^{-5} mmHg and at the temperature of about 45°C during daytime and left off pumping and heating in the night for 3 weeks and then it was filled with dense fresh ammonia gas (of purity of about 94%) for a full week.

The above gas and cell were used, with the pressure reduced to the working value (about 2×10^{-3} mmHg). The measured values of the center frequency and $\Delta\nu$ using the above gas and cell completely coincided with those using ammonia gas of purity of 94% which value was checked by mass-spectrometer analysis. Thus, it is certain that the cell treated in the above-mentioned way is completely free from the substitution effect.

Fig. 5 shows the frequency shift *versus* the pressure of ammonia gas, p. The

upper part of the curve (in the pressure region above some 3×10^{-3} mmHg) is quite straight and the lower part makes downward deviation from the straight line. The latter might be less reliable since the measurement of the partial pressure in the lower pressure region is far more difficult than in the larger.

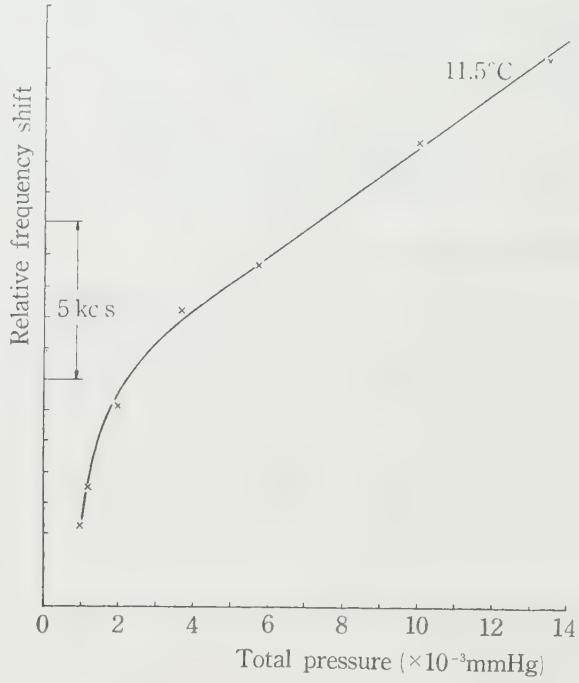

Fig. 5. Frequency shift *versus* pressure of ammonia gas. The cell wall temperature is indicated.

The frequency shift relative to the ammonia pressure was determined to be 0.77 ± 0.02 Mc/s/mmHg at $\Delta\nu=350$ kc/s. Therefore, in order to realize a precise frequency standard of an accuracy better than 5×10^{-9} using the ammonia spectrum ($\nu_0=23{,}870$ Mc/s) at the gas pressure of about 2×10^{-3} mmHg, the fluctuation of the partial pressure of ammonia gas should be kept within 14% or 2.8×10^{-4} mmHg.

Fig. 6 shows $\Delta\nu$ *versus* p. Since the wall collision broadening $\Delta\nu_w$ and the Doppler broadening $\Delta\nu_d$ are considered constant, so that the result can be represented, if it is assumed that $\Delta\nu_p/p=\kappa$ is constant (**12**), by the expressions (**2, 18**):

$\Delta\nu=\Delta\nu_p+\Delta\nu_w+\Delta\nu_d$ below some 4×10^{-3} mmHg,

$\Delta\nu=\{(\Delta\nu_p+\Delta\nu_w)^2+(\Delta\nu_d)^2\}^{1/2}$ between some 4×10^{-3} and 1.6×10^{-2} mmHg,

$\Delta\nu=\{(\Delta\nu_p)^2+(\Delta\nu_w)^2+(\Delta\nu_d)^2\}^{1/2}$ above some 1.6×10^{-2} mmHg,

where $\Delta\nu_w$ and $\Delta\nu_d$ are assigned respectively the values 52.6 kc/s and 34.9 kc/s which are calculated from

$$\Delta\nu_w = 5\left(\frac{a+b}{ab}\right)\left(\frac{T}{M}\right)^{1/2} \text{kc/s} \quad (\mathbf{14}),$$

$$\Delta\nu_d = 3.58\times10^{-7}\left(\frac{T}{M}\right)^{1/2}\nu_0 \text{ kc/s} \quad (\mathbf{15}),$$

when $T=274°\text{K}$ and X-band wave guide is used.

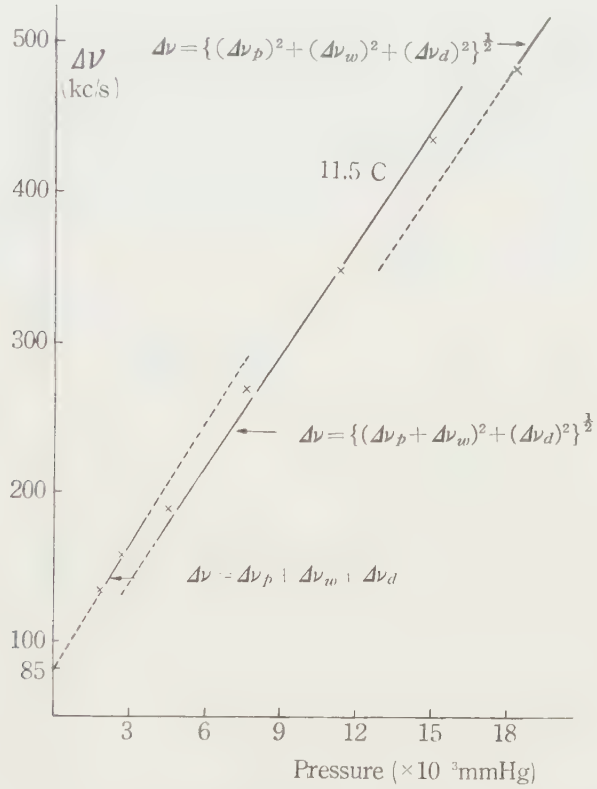

Fig. 6. $\Delta\nu$ *versus* pressure of ammonia gas. The cell wall temperature is indicated.

The value of $\Delta\nu_w+\Delta\nu_d$ at $p=0$ obtained by extrapolation from the curve $\Delta\nu=\Delta\nu_p+\Delta\nu_w+\Delta\nu_d$ becomes 85 ± 2 kc/s, which agrees well with the value 87.5 kc/s resulting from the values $\Delta\nu_w=52.6$ kc/s and $\Delta\nu_d=34.9$ kc/s in the above.

Thus, the relation $\Delta\nu_p=\kappa p$ and the expressions for $\Delta\nu$ might be demonstrated to hold in the pressure region 1×10^{-2} to 2×10^{-2} mmHg, and collision broadening parameter κ was determined to be 27.5 ± 0.1 Mc/s/mmHg. Fig. 7 shows the frequency shift *versus* $\Delta\nu_p$ which was derived from Fig. 5 by using the relation $\Delta\nu_p=\kappa p$. The absorption coefficient α is given by the expression (**17**):

$$\alpha = \frac{\alpha_0(\Delta\nu_p)^2}{(\nu-\nu_0\pm a\Delta\nu_p)^2}\frac{}{(\Delta\nu_p)^2},$$

where ν_0 is the center frequency of the absorption curve and α_0 is the absorption coefficient at $\nu=\nu_0$. The value of a was determined to be $(2.8\pm0.1)\times10^{-2}$ at $\Delta\nu=350$ kc/s which is selected since it is situated on the linear part and when the ammonia purity is about 94%. At lower pressures, the larger values are obtained. Tomita* gave the value 0.18 theoretically.

The temperature dependence of frequency shift (**19**) and $\Delta\nu$ had been one of the research items, but the author was unable to finish it because of the following circumstances. To obtain a measurable change in $\Delta\nu$, it is necessary to make a considerable change in the temperature as large as 100°C at least. It is, however, connected with some difficulties, since a large temperature variation causes partial pressure change due to both or either of the selective adsorption and the substitution effect excited in the cell and further in the present case, teflon spacers cannot stand such a large temperature variation.

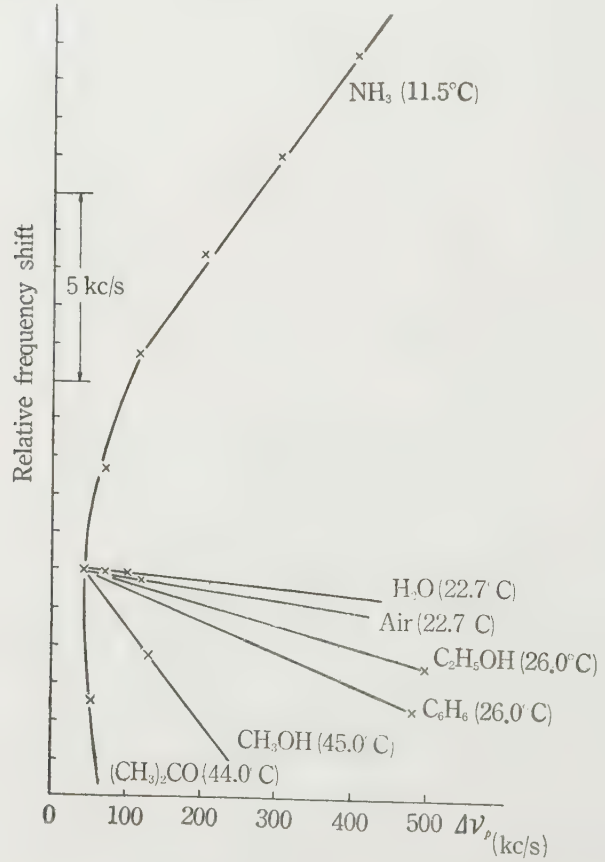

Fig. 7. Frequency shift *versus* pressure broadening. The cell wall temperature is indicated for each curve.

* Reported before the meeting of Physical Society of Japan, April, 1957. See also Reference (22).

6. Frequency shift when foreign gas is mixed

The frequency shift of ammonia inversion spectrum was also measured when some foreign gas was leaked into the cell containing the ammonia gas at the pressure of about 2×10^{-3} mmHg and $\Delta\nu=140$ kc/s. Fig. 8 shows the frequency shift *versus* $\Delta\nu_p$ of ammonia gas, each line being specified by the name of leaked foreign gas. All values of a have become negative, as shown in Table I and the author is sure of this result, though it is inexplicable for the present. Fig. 8 shows also the frequency shift of ammonia gas when the foreign gas was mixed at equal pressures before the introduction of the gas into the Stark cell. The measurement gives also the negative

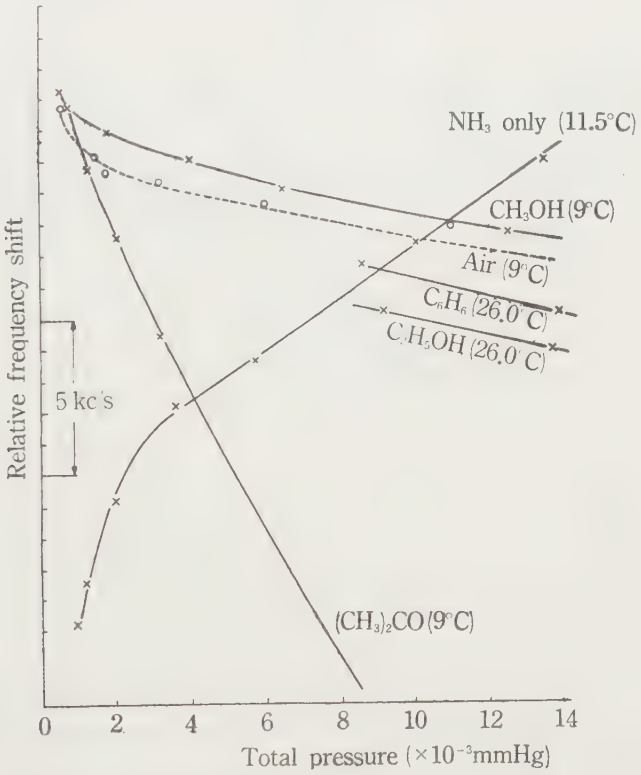

Fig. 8. Frequency shift *versus* total gas pressure. The cell wall temperature is indicated for each curve.

value of a for all the foreign gases. The large shift when aceton was mixed might be considered to be connected with the absorption by aceton at frequencies very near 23,870 Mc/s (**20**). The author, however, cannot come to any definite conclusion, considering that the absorption lines of aceton at those frequencies are very weak (**21**), while the used ammonia line is very strong. Either or both of the measurements of frequency shift and $\Delta\nu$ might be useful for investigation of reaction rate of a gas reacting on ammonia gas.

Table I.

Gas	Molecular dipole moment (in Debye)	Value of a
NH_3	1.47	$(2.8 \pm 0.1) \times 10^{-2}$
Air	0	$-(0.27 \pm 0.05) \times 10^{-2}$
H_2O	1.8	$-(0.19 \pm 0.05) \times 10^{-2}$
C_6H_6	0	$-(0.82 \pm 0.05) \times 10^{-2}$
C_2H_5OH	1.7	$-(0.56 \pm 0.05) \times 10^{-2}$
CH_3OH	1.7	$-(2.5 \pm 0.5) \times 10^{-2}$
$(CH_3)_2CO$	2.7	$-(36 \pm 10) \times 10^{-2}$

Acknowledgements

The author wishes to express his sincere thanks to Professor I. Takahashi for his guidance and discussion, and to Professor N. Sasaki and Mr. K. Kubota of Sumitomo Chemical Co. for the convenience given to analyze the sample gas by mass-spectrometer. Thanks are also due to Messrs. T. Ogawa, A. Hirai and J. Kakimoto, and many other colleagues for their assistance throughout this work.

REFERENCES

1. H. Lyons, Ann. N. Y. Acad. Sci., **55** (1952), 831.
2. K. Shimoda, J. Phys. Soc. Japan, **9** (1954), 378, 558, 567.
3. J. P. Gordon, H. J. Zeiger and C. H. Townes, Phys. Rev., **95** (1954), 282.
4. L. Essen, Nature, **176** (1955), 280.
5. I. Takahashi, T. Ogawa, M. Yamano, A. Hirai and M. Takeyama, Rev. Sci. Inst., **27** (1956), 739.
6. J. H. Burkhalter, R. S. Anderson, W. V. Smith and W. Gordy, Phys. Rev., **77** (1950) 152.
7. I. Takahashi, T. Ogawa, M. Yamano *et al.*, Report on Stark modulation atomic clock submitted to the research committee on atomic clock of Japan, Sept, 1956 (in Japanese).
8. I. Takahashi, T. Ogawa, M. Yamano and A. Hirai, Phys. Rev., **106** (1957), 606 (L).
9. K. Matsuura, Y. Sugiura and G.M. Hatoyama, J. Phys. Soc. Japan, **11** (1956) 1301; **12** (1957), 314.
10. I. Takahashi, T. Ogawa, M. Yamano and A. Hirai, IRE (to appear soon).
11. W. Gordy, W. Smith and R. Trambarulo, *Microwave Spectroscopy*, (John Wiley & Sons. Inc., New York, 1953) p. 198.
12. C. H. Townes and A. L. Schawlow, *Microwave Spectroscopy* (McGraw-Hill Book Co. Inc. New York, 1955) p. 344.
13. De Boer, *Dynamical Character of Adsorption*, (Clarendon Press, Oxford, 1953).
14. W. D. Coolidge, J. A. C. S. **45** (1923), 1637.
15. W. Gordy, W. Smith and R. Trambarulo, *Ibid.* p. 197.
16. W. Gordy, W. Smith and R. Trambarulo, *Ibid.* p. 188.
17. C. H. Townes and A. L. Schawlow, *Ibid.* p. 355.
18. C. H. Townes and A. L. Schawlow, *Ibid.* p. 374.
19. W. Gordy, W. Smith and R. Trambarulo, *Ibid.* p. 196.
20. B. Bak, E. S. Knudsen and E. Madsen, Phys. Rev., **75** (1949), 1622 (L).
21. T. L. Weatherly and D. Williams, J. Chem. Phys., **20** (1952), 755 (L).
22. K. Tomita, Prog. Theor. Phys., **18** (1957), 316.

Memoirs of the College of Science, University of Kyoto, Series A,
Vol. XXIX, No. 1, Article 6, 1958.

CENTER FREQUENCY OF AMMONIA INVERSION SPECTRUM IN LOW PRESSURE REGION

BY

Masaru YAMANO

(*Received June 9, 1958*)

ABSTRACT

The center frequency of ammonia inversion spectrum ($J=K=3$) was measured in Kyoto by Stark modulation atomic clock of absorption type (**1**) with reference to Tokyo UT2. The measured value of the center frequency was corrected using the pressure dependence which was measured by the author (**2**). Stark coefficient was also determined to be 23.52 ∓ 0.04 c/(volt/cm)^2. Error due to Doppler shift in the frequency measurement was minimized by using 5 Mc/s JJY and by a long time comparison of the JJY signal with 100 kc crystal oscillator (**3**). The center frequency of the spectrum was determined from a long time comparison with the astronomical frequency standard (JJY) from February to October in 1957 to be

23,870,130.05 0.05* · 0.1** · 0.2***(· 1.2) kc s

reduced to zero pressure on UT2 with ammonia of purity of 94%.

1. Introduction

The center frequency of the ammonia inversion spectrum ($J=K=3$) in low pressure region (below 10^{-2}mmHg) had been considered to be accurately constant until the frequency shift with gas pressure was found (**4, 5, 6**).

Therefore, the center frequency of the spectrum measured by atomic clock must be expressed, reduced to zero pressure, using the results of the frequency shift. Since the measurements of the frequency shift of the spectrum were performed using the Stark modulation system atomic clock of absorption type when the gas was pure ammonia and when some foreign gas was mixed respectively, the center frequency of the spectrum could be determined, based on Tokyo UT2 to the accuracy of the atomic clock, which corresponds to the comparison of the astronomical time with the atomic time. In the determination, the effect of the Doppler shift of JJY signal received in Kyoto was minimized, by a long time measurement of the center frequency of the spectrum utilizing the different frequencies (10 Mc/s and 5 Mc/s) of JJY.

* error of the atomic clock
** error of the reference (UT2)
*** error due to Doppler effect of JJY of 5 Mc/s (or 10 Mc/s).

Further, in the atomic clock, the cross point frequency, ν_s, (Fig. 1) was directly measured instead of the center frequency at the working pressure, ν_0, but the latter was accurately determined by the extrapolation of the curve of ν_s *versus* the square of the Stark field.

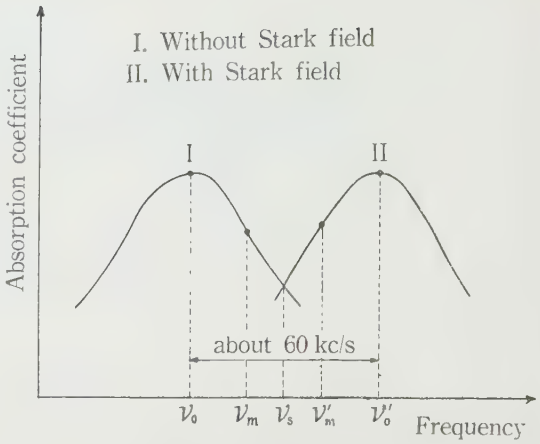

Fig. 1. Absorption curves with and without Stark electric field.

2. The determination of the center frequency

The experiment was performed with the same apparatus as in I*, only improved in such a way that the input microwave power to the cell is continuously changeable from 10 μW to 1×10^{-3} μW, in order that the experiment might be carried out without saturation broadening even below the gas pressure of about 1×10^{-3}mmHg. The value of ν_s was directly measured by using the atomic clock and the standard wave JJY (5 Mc/s), and the Stark shift determined by extrapolation from the curves of ν_s *versus* the square of the Stark field. Then ν_0 was obtained by subtracting the Stark shift from ν_s. Finally it was reduced to zero pressure by extrapolating the upper linear part of the curve in Fig. 5 in I.

(1) *Measurement of* ν_s

The final accuracy of measured ν_s is estimated to be 4.2×10^{-9} which is affected by the following errors.

a) The error due to random noise $\delta\nu_n$ (**1**) given by

$$\delta\nu_n = \frac{\pi}{M}(4kTB)^{\frac{1}{2}}\frac{1}{P_i}e^{\alpha_m l}\frac{\{(\nu-\nu_0)^2+(\Delta\nu)^2\}}{2l\alpha_m(\Delta\nu)^2(\nu-\nu_0)},$$

where

M: figure of merit,
B: Band width of detector amplifier,
k: Boltzmann constant,
α_m: maximum absorption coefficient of gas,
l: Stark cell length,
P_i: input microwave power,
$\alpha=\alpha_c+\alpha_g$ { α_c: absorption coefficient of the cell, α_g: absorption coefficient of the gas.

* The preceding paper: "Precise measurement of frequency shift of ammonia inversion spectrum" by the present author is referred to as I.

When the values (**1**):

$B=1$ c/s, $P_i \leqq 5\ \mu$W,
$M=25$, $\nu_s-\nu_0 \approx 30$ kc/s,
$l=3\times10^2$ cm, $\alpha_m=7\times10^{-4}$cm^{-1},
$\Delta\nu \approx 100$ kc/s, $\alpha_c=7.5\times10^{-3}$cm^{-1}

are used, we have $\delta\nu_n=28$ c/s. Therefore, the error due to random noise is less than 1×10^{-9}, but experimentally it was less than 2.0×10^{-9}.

b) The error due to gas dispersion, $\delta\nu_d$, given, after some calculations, by the following expression (**1**):

$$\delta\nu_d \leqq \frac{1}{2} e^{-\alpha l} |\Gamma| \frac{\lambda_g}{\lambda_0} \Delta\nu ,$$

if $$(\nu_s-\nu_0)^2 \ll \Delta\nu^2 ,$$

where

$l=3\times10^2$ cm : Stark cell length,
$\lambda_g=1.55$ cm : guide wavelength,
$\lambda_0=1.25$ cm : wavelength in free space,
$\Delta\nu \approx 10^5$ c. p. s,. :
$|\Gamma| = |\Gamma_i \cdot \Gamma_0|$
with Γ_i : input reflection coefficient,
Γ_0 : output reflection coefficient,

ν_s : frequency of the cross point of the two curves when Stark field is off and on.
ν_0 : center frequency of the absorption curve at working pressure of the atomic clock.

If $|\Gamma| \leqq 1\times10^{-2}$, $\delta\nu_d=60$ c/s. Therefore, the error due to gas dispersion is less than 2.5×10^{-9}. In the experiment, adjusting the microwave circuit, $|\Gamma|$ could be made less than 1×10^{-2} and the measurement using a phase shifter gave the error less than 2.0×10^{-9}.

c) The error due to the uncertainty of the Stark field. It was experimentally less than 2.4×10^{-9}.

d) The error due to the frequency shift with pressure change (**7**). It was experimentally less than 2.0×10^{-9}, averaged over more than 5 measurements, with the pressure of the gas indirectly measured by measuring $\Delta\nu$ and the gas purity higher than 94%.

All the errors are considered to be independent of each other. Therefore, the final accuracy of measured ν_s is given by

$$(2.0^2+2.0^2+2.4^2+2.0^2)^{1/2}\times10^{-9}=4.2\times10^{-9} .$$

The frequency comparison of ν_s was chiefly done with 5 Mc/s JJY as mentioned before, at 9 a. m. and 3 p. m. every day through six days of each week. Then the

error due to Doppler shift could be reduced (**3**) within 1×10^{-8}. But during daytime, the field intensity of 5 Mc/s JJY is usually weak and when it was so weak that the frequency measurement was impossible, 10 Mc/s JJY was used which is usually strong in daytime, but then the error due to Doppler shift becomes larger up to 5×10^{-8}. Five values of ν_s obtained at each measurement were averaged. These measurements of ν_s on UT2 were performed from February to October, 1957, by 5 Mc/s and 10 Mc/s JJY.

(2) *Measurement of Stark shift* $(\nu_s-\nu_0)$

It is the most accurate and simple way of getting ν_0 from ν_s, to extrapolate to the zero Stark field the curves which show ν_s *versus* square of the Stark field for various pressures, because at the Stark field below 5 volt/cm, the loop gain of the frequency control loop was experimentally sufficient and the error of the measured ν_s was below 2×10^{-9}. Since the impedance matching of the Stark cell is more difficult

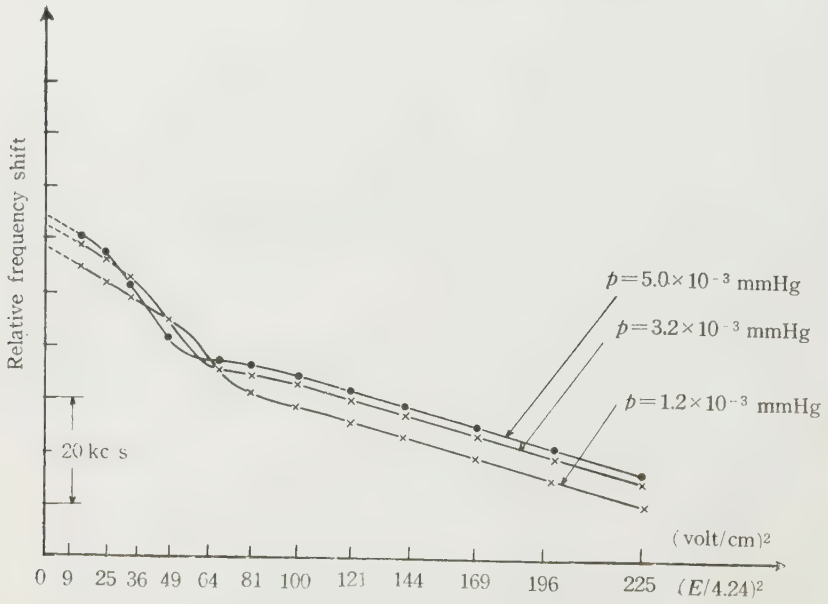

Fig. 2. ν_s *versus* square of Stark field at various pressures of ammonia of purity of 94%.

in the wide frequency range, the source modulation method of getting ν_0 is a simple way but may be less accurate than that of the extrapolation of the curves. Fig. 2 shows ν_s *versus* square of Stark field at various pressures of ammonia of purity of 94%. The kinks in the curves seem to be caused by the splitting-up of the spectral line into 23 components (**8**) in a weak field and the sudden change of the envelope

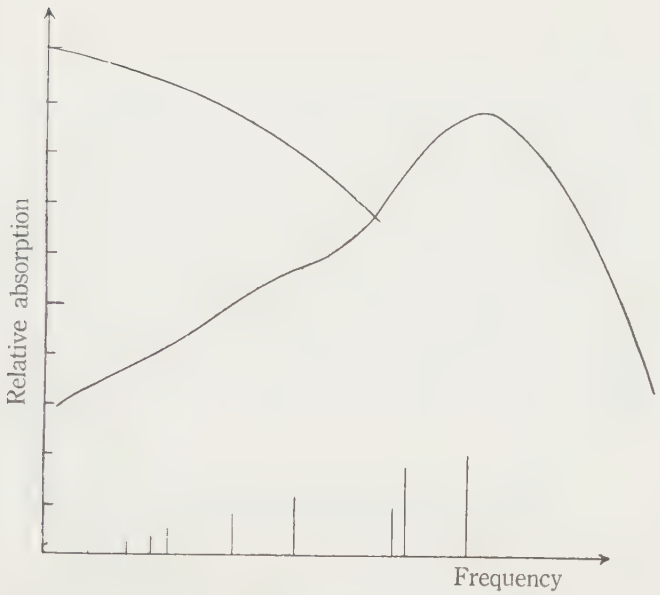

Fig. 3. Stark splitting of the spectrum and its envelope in the weak field, nine major components being plotted out of 23 altogether.

of the components near 9 volt/cm Stark field (Fig. 3). The Stark voltage was measured to the accuracy of 2×10^{-4} by using an amplifier with chopper and two standard cadmium cells (**1**). The precisely measured value of Stark field intensity can be used to determine the Stark coefficient of the spectrum so far as the absorption curve may be considered to shift with the shape unchanged in a weak Stark field. The value 23.52 ± 0.04 c/(volt/cm)^2 (at $E=61.98$ volt/cm and $\Delta\nu=150$ kc/s) was obtained in this way.

(3) *Frequency shift due to self-broadening*

The frequency shift of the spectrum due to pressure change was found (**4**, **5**, **6**) and precisely measured (**2**) first when the gas was pure ammonia and when some foreign gas was mixed respectively. Figs. 5 and 7 in I show frequency shift *versus* p and frequency shift *versus* $\Delta\nu_p$ respectively. Fig. 8 in I also shows the frequency shift when some foreign gas is mixed. The value $(2.8\pm0.1)\times10^{-2}$ of a, the ratio of frequency shift to $\Delta\nu_p$ (pressure broadening) and the value $(0.77\pm0.1)\times10^{-2}$ of the ratio of frequency shift to pressure are used to calculate the center frequency at zero pressure from ν_0 at the working pressure of the atomic clock.

Finishing the above-mentioned processes, the center frequency of the spectrum at zero pressure was determined on UT2. Fig. 4 shows the center frequency *versus* time in month, which was obtained from ν_s. The center frequency of the ammonia 3,3 line was determined to be

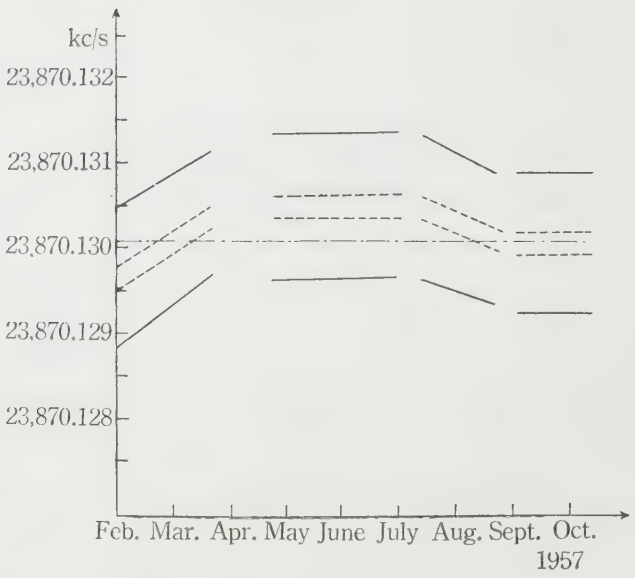

Fig. 4. Center frequency *versus* time in month. When compared with 5Mc/s JJY, it is limited between two dotted lines indicated whereas when with 10Mc/s JJY, it is limited between two solid lines.

$$23{,}870{,}130.05 \pm 0.05^{*} \pm 0.1^{**} \pm 0.2\ \text{kc}^{***} (1.2\ \text{kc/s})$$

from February to October in 1957 reduced to zero pressure on UT2, where * denotes the error of the atomic clock, ** the error of the reference (UT2) and *** the error due to Doppler shift of JJY of frequency 5 Mc/s (or 10 Mc/s). In the above determination, the shift due to $\Delta\nu_w$ (wall collision broadening) was neglected, though it was not certain whether it existed. The center frequency given above is lower than the value by K. Shimoda (**9**), namely:

$$23{,}870{,}131.05 \pm 0.05\ \text{kc/s},$$

on UT2, reduced to zero pressure with $a = 0.4$, measured by Stark, source and Zeeman modulation atomic clock, with circular waveguide, but purity of ammonia unspecified, while it is larger than the value by Sugiura and Hatoyama *et al.* (**10**), namely:

$$23{,}870{,}129.31 \pm 0.05\ \text{kc/s},$$

on UT2, reduced to zero pressure with $a = 0.18$, measured by source modulation atomic clock, with K band wave guide, but purity of ammonia unspecified.

These three values of the center frequency do not agree within the experimental error. This seems to be connected with the disagreement of the values of a which will be in part explained by the circumstance that the partial pressure of the ammonia was not measured in the experiments by the others than the present author.

3. Conclusion

The accuracy of the absorption type atomic clock which utilizes ammonia inversion spectrum as a frequency standard had been considered to be mainly limited by the errors due to the detection of the spectral line, neglecting the effect of a as being very small. On the contrary, the value of a is considerable and it affects the center very frequency through the gas pressure, as can be seen. The value of a was measured for three different types of atomic clock and the three values agreed with each other in the order of magnitude. So, to obtain the atomic clock of the final accuracy better than 1×10^{-9}, the gas pressure must be kept within the error of 1×10^{-2} in 10^{-3}mmHg region. It is almost impossible, however, by the present vacuum technique. To keep the constancy of the total gas pressure in the cell might be realized, for instance, by supplying fresh ammonia gas very slowly into the cell from a large gas container attached. However, to keep the constancy of the partial pressure of ammonia within the error of 1×10^{-2} in 10^{-3}mmHg is another difficulty. Even if it is possible, for obtaining the atomic clock of the accuracy better than 1×10^{-9}, the molecular beam method seems better than the absorption method. But the frequency shift connected with a may also happen in the molecular oscillator using ammonia gas (**11**), although the amount of the shift is far smaller than that in the absorption type atomic clock.

Theoretically, Tomita's theory (**12**), which is based upon Anderson's impact theory, is most accurate but does not agree so well with the experimental results. He ascribed the difference of the theory from the experiment to the rough assumption, since he assumed that the perturber should pass straightly with uniform velocity. But when foreign gas exists, his theory cannot explain the negative value of a.

According to the phase shift theory (**13**), if the potential of interaction of two molecules is assumed to be of the form

$$V = \frac{B}{r^n},$$

where B is a certain constant and r the intermolecular distance, the value of a vanishes and $n=3$ for the dipole-dipole interaction, and otherwise the higher n, the smaller a. But by this theory, the negative value of a when foreign gas is mixed cannot be explained either.

Further experiments of the frequency shift when foreign gas is mixed for various samples and by various mixing methods are now in progress. Table I in the preceding paper (I) shows no correlation existing between dipole-moment and a. For the purpose of measuring more precise partial pressure of ammonia under the working conditions, the mass-spectrometer or some other equipment working with the atomic clock may be necessary.

Acknowledgement

The author wishes to express his sincere thanks to Professor I. Takahashi for his kind guidance and discussions and to Professor M. Miyaji of Tokyo Astronomical Observatory for valuable suggestions on frequency comparison. The author's thanks are also due to Professor K. Tomita for his useful advice and to many coworkers for their assistance throughout this research.

REFERENCES

1. I. Takahashi, T. Ogawa, M Yamano, A. Hirai and M. Takeyama, Rev. Sci. Inst., **27** (1956), 739.
2. M. Yamano, Mem. Coll. Sci. Kyoto Univ., **29** (1958), 57.
3. I. Takahashi, T. Ogawa, M. Yamano, A. Hirai and M. Takiuchi, IRE, **45** (1957), 1408.
4. I. Takahashi, T. Ogawa, M. Yamano *et al.*, Report on Stark modulation atomic clock submitted to the research committee on atomic clock of Japan, Sept. 1956.
5. I. Takahashi, T. Ogawa, M. Yamano and A. Hirai, Phys. Rev., **106** (1957), 606(L).
6. K. Matsuura, Y. Sugiura and G. M. Hatoyama, J. Phys. Soc. Japan, **11** (1956), 1301; **12** (1957), 314.
7. M. Yamano, Report of the researches conducted in doctor course, Faculty of Science, Kyoto University, March, 1958 (in Japanese).
8. J. M. Jauch, Phys. Rev., **72** (1947), 715.
9. K. Shimoda, J. Phys. Soc. Japan, **12** (1957), 558.
10. K. Matsuura, Y. Sugiura and G.M. Hatoyama, Phys. Rev., **106** (1957), 607(L).
11. J. C. Helmer, J. Appl. Phys., **28** (1957), 212.
12. K. Tomita, Prog. Theor. Phys., **18** (1957), 316(L).
13. C. H. Townes and A. L. Schawlow, *Microwave Spectroscopy* (McGraw-Hill Book Co. Inc., New York, 1955) p. 355.

Memoirs of the College of Science, University of Kyoto, Series A,
Vol. XXIX, No. 1, Article 7, 1958.

ON THE INFLUENCE OF OXYGEN GAS UPON THE OPTICAL ABSORPTION BANDS OF EVAPORATED BARIUM OXIDE FILMS IN THE ULTRAVIOLET REGION

BY

Tosiro TOMOTIKA

(*Received June 10, 1958*)

ABSTRACT

By measuring the optical absorption of BaO films evaporated in vacuum, it is observed at room temperature that the threshold for absorption occurs at 320 mμ and the second rapid rise in absorption begins at 250 mμ approximately. Two absorption bands are observed between 320 mμ and 250 mμ: one has a maximum at about 303 mμ, while the other has a maximum at about 285 mμ. Tyler assumed that the absorption bands in the region of 320 mμ~250 mμ are exciton bands, and various experimental results concerning these absorption bands have also been reported by other investigators.

In our laboratory, the effect of oxygen gas upon the absorption bands under various heat treatments has been investigated. By measuring the change of oxygen gas pressure in a definite volume as well as the amount of BaO, it has been observed that the absorption bands in the region of 320 mμ~250 mμ vanished out and at the same time the reduction of oxygen gas pressure in the definite volume occurred corresponding to the stoichiometric amount of oxygen in BaO.

Thus, the result of the present experiment seems to suggest that the 320 mμ~250 mμ absorption bands are due to the production of excitons.

1. Introduction

Since Tyler (**1**) found that the edge of optical absorption of evaporated BaO films lies at 3.8 ev (≈320 mμ) and a second increase in the absorption constant occurs at 4.8 ev (≈260 mμ) approximately, several experimenters have investigated the energy bands in BaO by optical methods. The location of the absorption edge at about 3.8 ev as reported by Tyler was confirmed by Taft and Dickey (**2**) on the basis of studies on photoelectric emission from thin metallic film deposited on the surface of BaO layers. In the case of BaO single crystals, the optical absorption and photoconductivity were measured by Tyler and Sproull (**3**), thus obtaining the results that the threshold photon energy for both the optical absorption and photoconductivity is 3.8 ev (≈320 mμ) and that a first absorption band is accompanied by photoconductivity, but not a second absorption band. Judging from the fact that the absorption constant is of the order of 10^5 cm^{-1} at the peak of the first absorption band, Tyler has assumed that this absorption band may be attributed to the production of excitons in BaO

lattice, and that this band is accompanied by photoconductivity due to the thermal dissociation of excitons or excitation ionization of impurity centres.

Also, by measuring the spectral distributions of photoelectric yield for BaO surfaces prepared in different ways, Apker *et al.* (**4**) observed that the abrupt rise at 5.0 ev is characteristic of all samples, but the behaviour for $h\nu < 5.0$ ev depends on the procedure in which the sample was prepared. They attributed the rise in the yield at $h\nu \approx 3.8$ ev to exciton-induced photoelectric emission from some kinds of impurity centres.

Later, measurements of the optical absorption of BaO films at temperatures between 15°K and 370°C were carried out by Zollweg (**5**), who reported that the two strongest absorption peaks in the region between 3.8 ev and 5.0 ev are to be caused by exciton absorption. Recently, Jahoda (**6**) has measured the reflectivity spectrum of BaO single crystals in the ultraviolet region and making use of the Kramers-Kronig relation, he has obtained the spectral distribution of optical absorption constant which is similar to Zollweg's. Thus, he has concluded that the absorption bands between 3.8 ev and 5.0 ev are exciton bands. These experimental results have also been explained theoretically by Overhauser (**7**).

Independent investigation on the optical absorption of BaO films has been carried on in these several years in our laboratory. Takazawa and the present writer (**8**) observed that the absorption bands in the region of 320 mμ~250 mμ vanished out suddenly when BaO film was exposed to oxygen gas, but no alteration occurred in the case of the absorption band beginning at about 250 mμ, and these results led us to the conclusion, contrary to the results by Tyler and others, that the absorption bands in the region of 320 mμ~250 mμ are due to some kinds of lattice imperfection.

In order to decide whether the above-mentioned absorption bands are due to exciton production or to some kinds of lattice imperfection, the present writer has attempted to measure quantitatively the ratio of the amount of oxygen gas necessary for vanishing out absorption bands to the amount of BaO, under various heat treatments, and to the description of the results of our measurements the present paper is mainly directed.

2. Experimental apparatus and techniques

The evaporation vacuum-cell used in the present experiment is shown schematically in Fig. 1. The cell whose total volume is about 20 cc consists of two parts: one is made of glass and has vacuum cocks, electrodes and thermistor bead, while the other is a fused quartz tube on whose inside surface BaO film was evaporated. These two parts were connected to each other by a joint using silicon grease. By cooling the jointed part by water, it was possible to heat the quartz tube up to about

1,000°C and to exhaust gases from the tube thoroughly. The filament made of platinum wire of 0.3 mm diameter was used and was coated with $BaCO_3$ (Merck Ultra Pure) which was pasted in distilled water. The cell was connected by another joint to the vacuum system. After having exhausted, $BaCO_3$ was converted to BaO by heating the $BaCO_3$ coated platinum filament slowly up to about 1,000°C, the heating having been continued until gas evolution has substantially ceased. Then the quartz tube was heated in a furnace up to about 1,000°C.

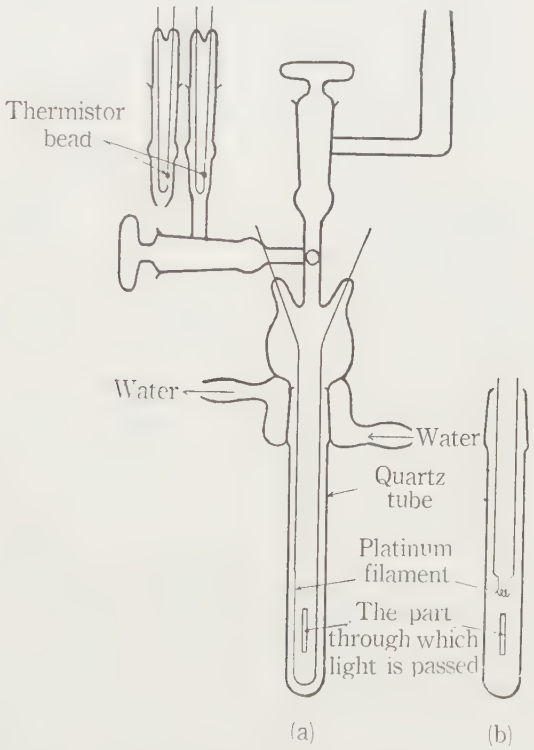

Fig. 1. Evaporation vacuum cell.

After these procedures, by heating the filament at temperatures of 1,200°C～1,300°C the BaO film was evaporated on the inside surface of the quartz tube whose temperature was slightly higher than room temperature. The temperature of the coated filament was measured by an optical pyrometer. In all cases the optical absorption of BaO film was measured at room temperature by the use of a Beckman DU spectrophotometer. Oxygen gas prepared by heating $KMnO_4$ in a vacuum chamber was dehydrated by P_2O_5 for a few days, and after having finished the measurement of the optical absorption of the BaO film in vacuum, the dehydrated oxygen gas was led to the evaporation cell through a cold trap of dry ice–alcohol or liquid oxygen.

Then, the relationship between the change of optical densities at the peaks of

the absorption bands and the change of oxygen gas pressure was observed by means of a thermistor vacuum gauge. Fig. 2 shows the thermistor gauge as used under such a condition that another thermistor bead exposed to atmosphere was used as a temperature compensator.

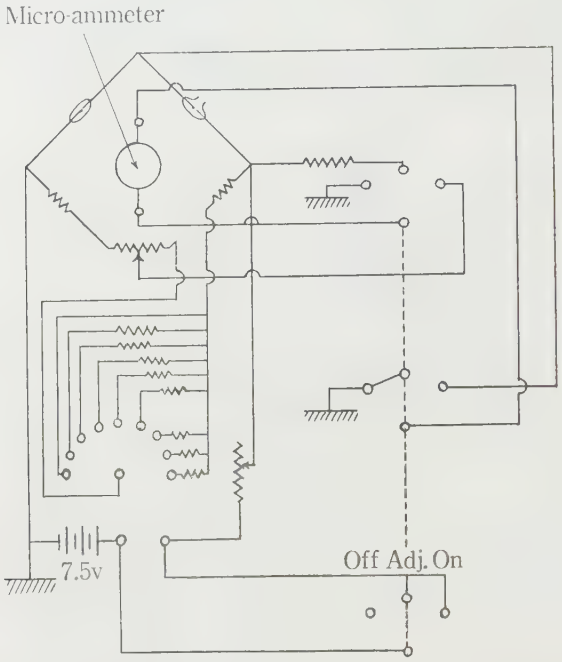

Fig. 2. Schematic diagram of the thermistor vacuum gauge.

The thermistor gauge was calibrated in such a manner that a micro-ammeter with full scale of 10 μA indicates the zero point at one atmospheric pressure. The characteristic curve for oxygen gas is shown on semilogarithmic scale in Fig. 3, taking the logarithm of oxygen gas pressure as ordinate and the electric current as abscissa. It will readily be seen that this characteristic curve is linear in a range from 5×10^{-1} mmHg to 5×10^{-2} mmHg. It was able to observe pressure differences of 5×10^{-2} mmHg at 1 mmHg, 2×10^{-2} mmHg at 0.5 mmHg, 2×10^{-3} mmHg at 1×10^{-1} mmHg and 2×10^{-3} mmHg at 5×10^{-2} mmHg, respectively. The limiting pressures capable of being observed were about 5 mmHg and 5×10^{-3} mmHg respectively.

The thermistor gauge was also used as a qualitative indicator of gas pressure in the evaporation cell. When the cell was exhausted sufficiently, only a small amount of increase of gas pressure in the cell was observed even when the quartz tube was heated at ~500°C for about thirty minutes. In such a case the alteration of the optical densities of the evaporated film in the ultraviolet region scarcely occurred at room temperature for several hours.

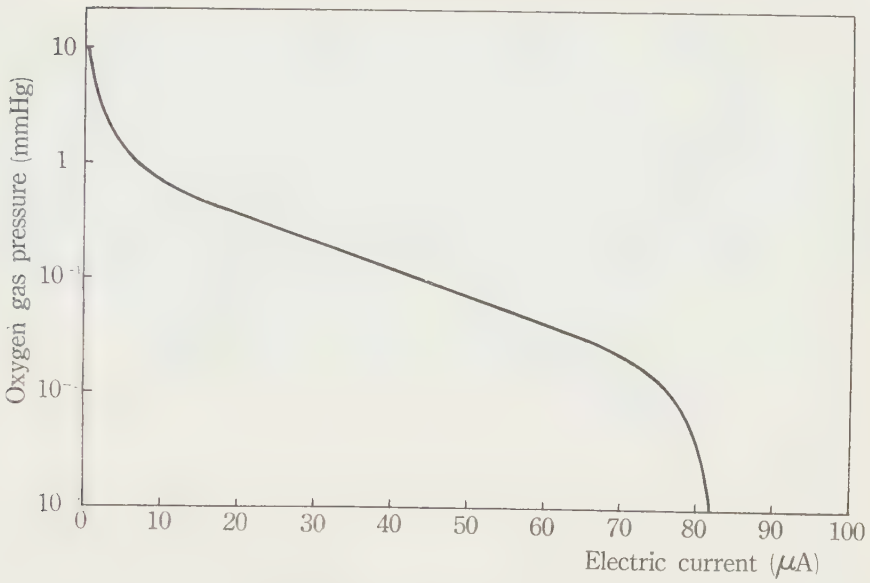

Fig. 3. The characteristic curve for oxygen gas at room temperature.

3. Experimental results

Fig. 4 shows a typical absorption spectrum of BaO films in the ultraviolet region, as observed at room temperature. The spectrum observed under no heat treatment is shown by curve A, while curve B shows the spectrum as observed after having heated the BaO films at about 400°C in vacuum and then quenched. It is easily seen that there are two absorption bands in the region between 320 mμ and 250 mμ, a large band in the region of wavelengths shorter than 250 mμ and presumably a broad band in the region of wavelengths longer than 320 mμ, though the last one has not yet been recognized definitely. Also it is found that the positions of absorption peaks were shifted to longer wavelength side under heat treatment in vacuum and at the same time the sharpening of the band shape took place.

In order to obtain the concentration of the absorption centres responsible for the absorption bands in the region of 320 mμ~250 mμ, an order estimation of the absorption constants at the absorption peaks was attempted in the following way. Regarding the $BaCO_3$ coated platinum filament in the form of coil, as shown in Fig. 1 (b), as a point and thus assuming that BaO was evaporated spherical-symmetrically from the platinum coil, the distribution of the BaO film thickness on the inside surface of the quartz tube was calculated approximately by making use of the total amount of BaO film which was measured by a steelyard.

Then, the optical densities at the absorption peaks were calculated by taking the absorption constants there to be of the order of $10^5\,cm^{-1}$, and it was found that the

calculated values were in good agreement with observed ones. Judging from this result it is certain that the absorption centres have high concentration as obtained by Tyler and others.

In other cases of the present experiment, a platinum filament with the shape of a straight line as shown in Fig. 1 (a) was generally used in order to make the thickness of BaO film as uniform as possible. In such a case the total amount of BaO had to be of the order of 0.5 mg in order to obtain appropriate optical densities.

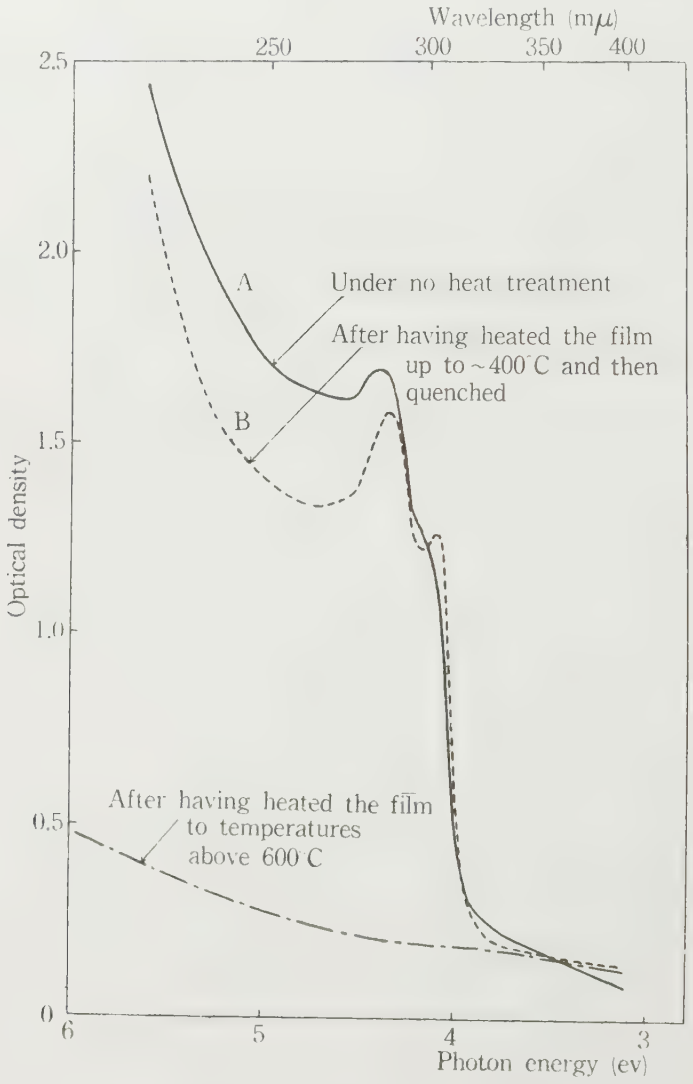

Fig. 4. Optical absorption curves for BaO film in vacuum observed at room temperature.

Fig. 5 shows the change in the absorption bands occurred when the film was exposed to dry oxygen gas with pressure of about 1 mmHg at room temperature. It was observed that a broad absorption band in the region of wavelengths longer than 320 mμ vanished out suddenly, notwithstanding that the magnitude of the band varied, as shown in Fig. 6, with the film thickness as far as its optical densities were concerned. It was found, however, that the absorption bands in the region of wavelengths shorter than 320 mμ was not remarkably affected even when the film had been exposed for a day to oxygen gas whose pressure was about 80 mmHg.

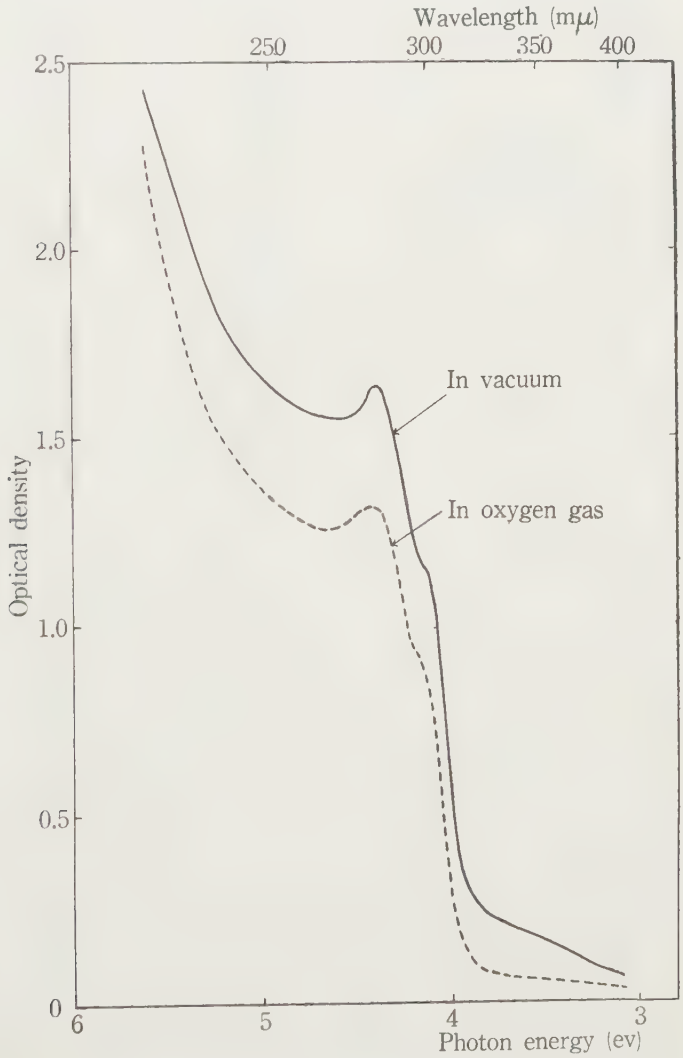

Fig. 5. Absorption curves for BaO film observed at room temperature.

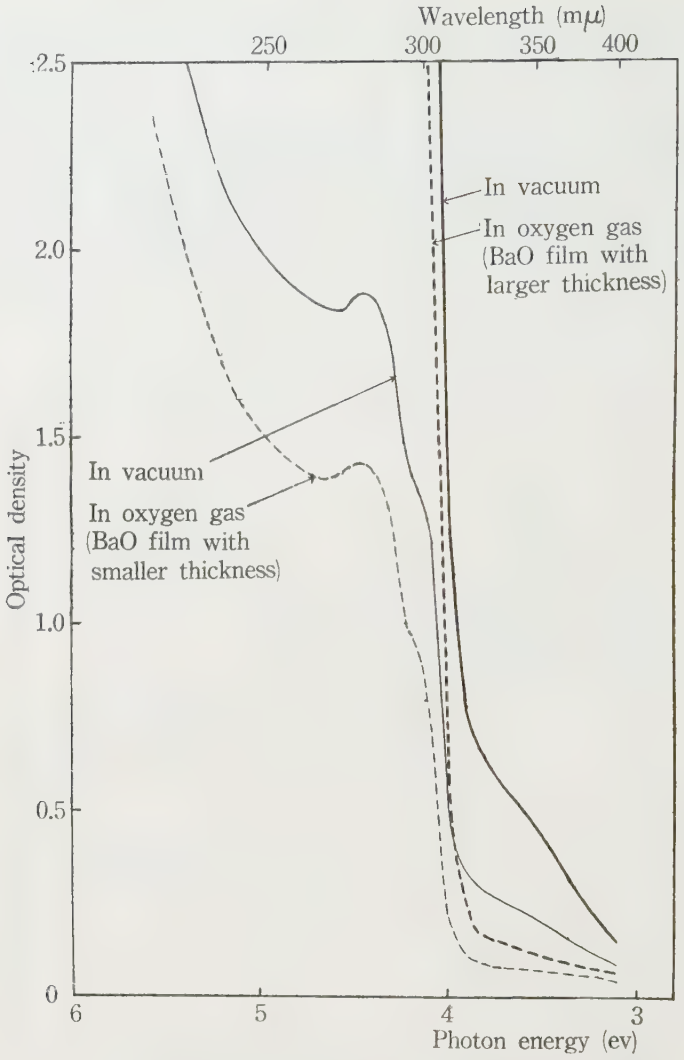

Fig. 6. Absorption curves for BaO films with different thicknesses, observed at room temperature.

Next, by heating the BaO film in oxygen gas with pressure of about 1 mmHg, it was observed that the two absorption bands between 320 mμ and 250 mμ began to decrease at about 200°C as the oxygen gas pressure in the cell decreased and that after both the magnitude of the absorption bands and the oxygen gas pressure had reached their respective minimum values, the magnitude of the bands began to increase at about 400°C as the oxygen gas pressure increased, as shown in Fig. 7. Such a reaction is similar to the well-known chemical reaction $BaO \underset{800°C}{\overset{500°C}{\rightleftharpoons}} BaO_2$, which occurs when BaO is heated in the air, the only difference being that the

temperature at which the reaction in the present experiment occurred is much lower than that at which the above-mentioned chemical reaction occurs.

It can be seen from Fig. 7, however, that the absorption band beginning at about 250 mμ in BaO is not affected under the present heat treatment. Thus, in order to decide whether this reaction might be the chemical reaction $BaO \rightleftarrows BaO_2$ or not, a quantitative measurement was carried out more precisely in the following way.

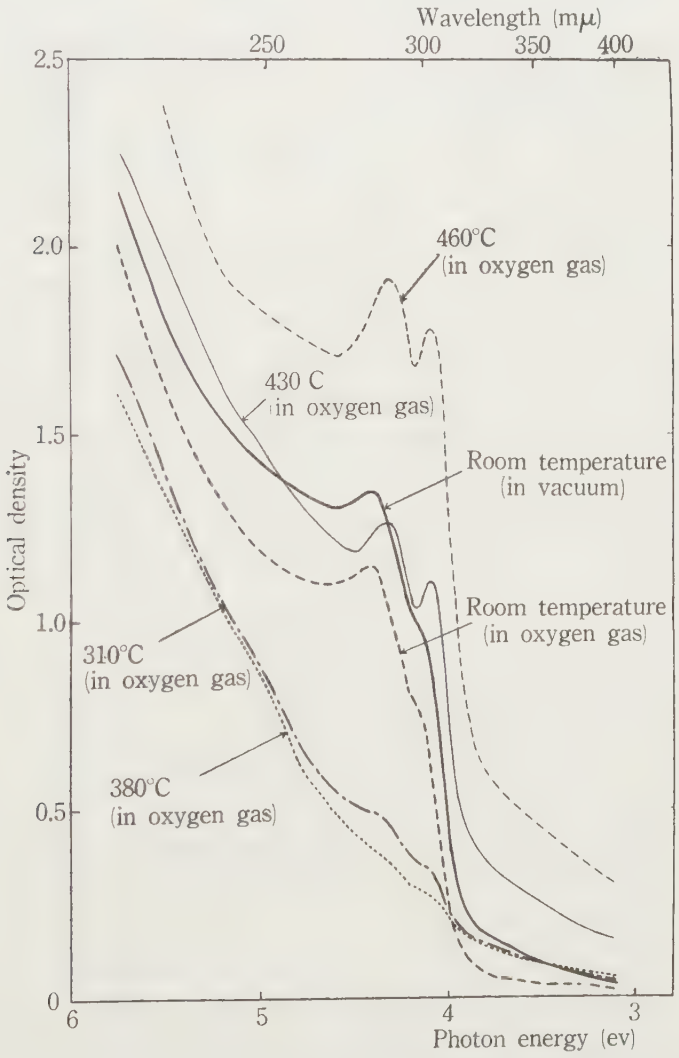

Fig. 7. Changes occurred in the absorption bands of BaO film observed at room temperature, after having heated the film in oxygen gas at various temperatures indicated.

First, under such a condition that BaO on the platinum filament had all evaporated, the amount of BaO film was calculated from the amount of $BaCO_3$ pasted on the filament which was measured by a steelyard, and dry oxygen gas whose pressure had been measured by an oil manometer was stored beforehand in a small region of about 2 cc to which a thermistor bead was attached. Then, after having measured the optical absorption of BaO film in vacuum, the stored oxygen gas was diffused into the cell and the relation between the magnitudes of the bands and oxygen gas pressure was observed under various heat treatments. It was thus found that the magnitudes of the bands in the region from 320 mμ to 250 mμ generally decreased linearly with the decrease of the oxygen gas pressure and that the amount of decrease of oxygen which was calculated from the decrease of oxygen gas pressure in the cell was of the same order of magnitude as the stoichiometric amount of oxygen in the BaO film.

Similar experiments were also carried out for the BaO film heated up to 400°C ~500°C in vacuum beforehand and then quenched, and the results as shown in Fig. 8 were obtained. In this case, the influence of oxygen gas upon the absorption bands in the ultraviolet region was not observed at room temperature. By heating the film in oxygen gas, however, it was observed that the magnitudes of the two absorption bands in the region of 320 mμ~250 mμ began to decrease at about 300°C and after the magnitudes of these bands had reached their respective minimum values, they began to increase at about 500°C. As shown in Fig. 9, an exactly linear relationship was observed between the optical density at one of the peaks of the bands and the oxygen gas pressure in the cell.

In case when the amount of oxygen in the cell was less than the stoichiometric amount of oxygen in the BaO film, the decrease of the magnitude of the bands was stopped at intermediate values as shown in Fig. 10.

Judging from these results it may be concluded that the change of the magnitudes of the absorption bands between 320 mμ and 250 mμ due to oxygen gas should be attributed to the chemical reaction $BaO \rightleftarrows BaO_2$ and that a large absorption band which was still observed after the bands in BaO in the region of 320 mμ and 250 mμ vanished out should be due to BaO_2.

Whenever BaO film was heated to temperatures above 600°C in vacuum as well as in oxygen gas for about twenty minutes and then quenched, the film became transparent in the ultraviolet region as shown in Figs. 4 and 8; in other words, all the bands in the ultraviolet region vanished out. In such a film, the optical absorption bands could not appear again by any heat treatment.

Next, we have investigated the effect of H_2O vapour upon the absorption bands in BaO. Pure H_2O vapour was prepared in such a way that after having exhausted the vacuum chamber, H_2O frozen beforehand in the cold trap was evaporated in the chamber. After the optical absorption of BaO in vacuum had been measured, an appropriate amount of H_2O vapour was introduced into the cell.

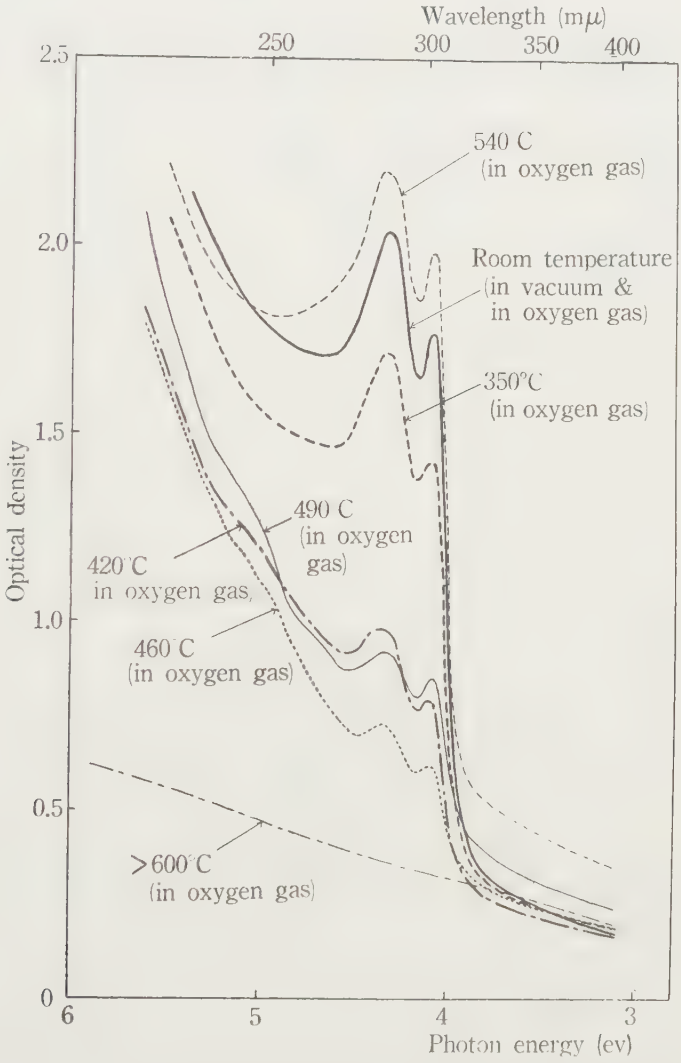

Fig. 8. Changes occurred in the absorption bands of BaO film which was heated in vacuum up to 400°C~500°C beforehand and then quenched. The obvervations were done at room temperature, after having heated the film in oxygen gas at various temperatures indicated.

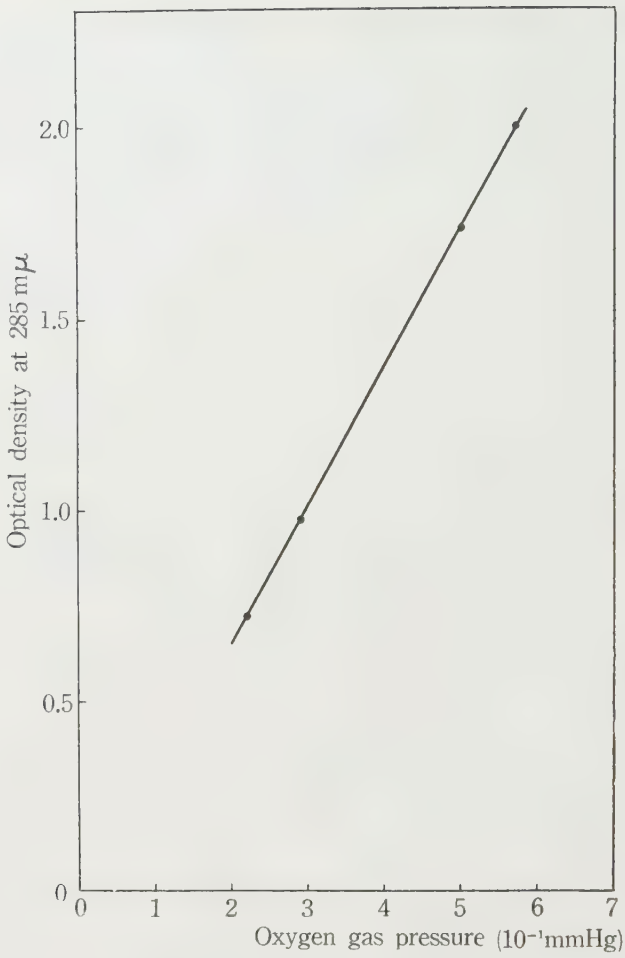

Fig. 9. Relationship between the optical density at one of the absorption peaks (285 mμ) and oxygen gas pressure in the experiment shown in Fig. 8.

It was thus observed at room temperature that the magnitudes of all the absorption bands in the ultraviolet region were decreased in approximately proportion to the amount of H_2O vapour as shown in Fig. 11. When an amount of H_2O vapour which is enough to cause such a reaction that all BaO's $\rightarrow Ba(OH)_2$ was introduced into the cell, it was observed that the two bands in the region between 320 mμ and 250 mμ vanished out at room temperature, while the band in the region of wavelengths shorter than 250 mμ still remained, as shown also in Fig. 11. This phenomenon is fairly similar to a phenomenon occurred when BaO film was exposed to oxygen gas, which was observed by Takazawa and the present writer some years ago (8). The above-described results of our present experiment seem to suggest

that oxygen gas used in our previous experiment had contained H_2O vapour to some extent.

Further additional experiments were carried out in case when BaO film was irradiated by AH-6 mercury lamp for ten hours, and it was observed that no change occurred in the absorption bands.

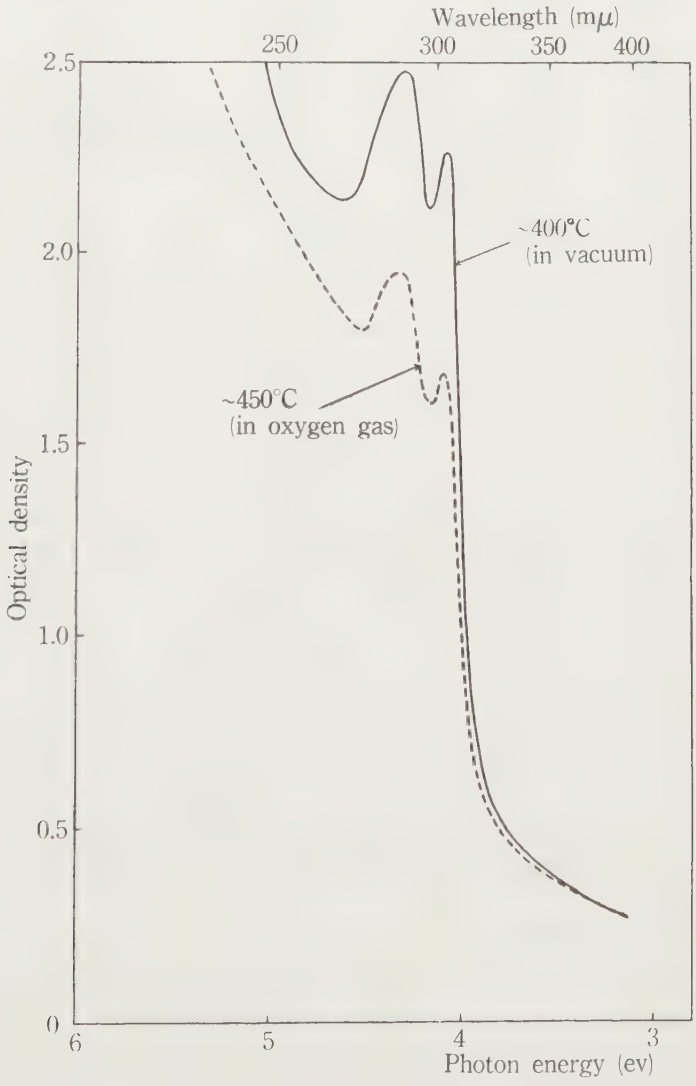

Fig. 10. Changes in the absorption bands of BaO film, after having heated the film in a small amount of oxygen gas, observed at room temperature.

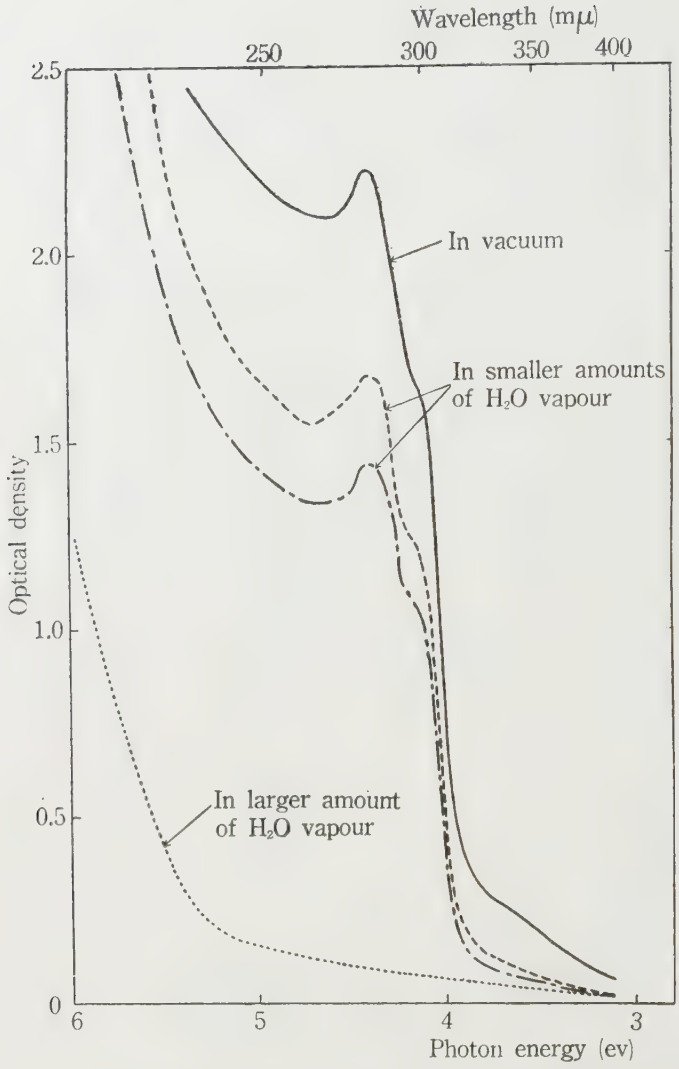

Fig. 11. Curves of optical density *versus* photon energy for BaO film when various amounts of H_2O vapour were introduced into the cell.

4. Summary and conclusion

In the present experiment, the optical absorption of BaO film evaporated in vacuum has been measured and it has been first observed at room temperature that there are two absorption bands in the region of wavelengths between 320 mμ and 250 mμ, a large band in the region of wavelengths shorter than 250 mμ and presumably a broad band in the region of wavelengths longer than 320 mμ. Secondly, it has been found that the positions of the absorption peaks are shifted to longer

wavelength side under heat treatments in vacuum and at the same time the sharpening of the band shape takes place.

The absorption bands in the region of 320 mμ~250 mμ have been assumed by Tyler to be exciton bands and the exciton characteristics of these bands have been investigated by other experimenters.

In our laboratory, the influence of oxygen gas upon the absorption bands in the region of wavelengths between 320 mμ and 250 mμ has been previously investigated. In the first place, the high concentration of the absorption centres responsible for these bands was confirmed by the order estimation of absorption constant at the absorption peak. On the other hand, it has been observed by Takazawa and the present writer that when BaO film was exposed to oxygen gas at room temperature, the absorption bands in the region between 320 mμ and 250 mμ vanished out.

In the present experiment, the influence of oxygen gas upon the absorption bands of BaO film has been quantitatively investigated by the use of a thermistor vacuum gauge in order to decide whether the bands in the region of 320 mμ~250 mμ are exciton bands, as assumed by Tyler, or not.

It has thus been found that a broad band in the region of wavelengths longer than 320 mμ vanished out suddenly when the BaO film has been exposed to oxygen gas at room temperature, while the absorption bands in the region of wavelengths shorter than 320 mμ is not remarkably affected even when the film has been exposed for a day to oxygen gas with pressure fairly higher than 1 mmHg.

By heating the BaO film in a definite amount of oxygen gas, it has been observed that the magnitudes of the absorption bands in the region of wavelengths between 320 mμ and 250 mμ decrease almost linearly till about 400°C with the decrease of oxygen gas pressure in the cell, and it has been shown by a quantitative measurement that this phenomenon should be attributed to the chemical reaction $BaO \rightarrow BaO_2$. If defects or impurities in BaO lattice were the cause of the absorption bands between 320 mμ and 250 mμ, it would perhaps be most likely that these bands are due to the presence of oxygen vacancies. If so, it would be expected that the magnitudes of these bands are changed by heating the film in oxygen gas without being accompanied by the chemical reaction $BaO \rightarrow BaO_2$. The above-mentioned fact that the vanishing out of these bands associated with the heating of the BaO film in oxygen gas is accompanied by the chemical reaction $BaO \rightarrow BaO_2$ seems to show, however, that these bands are inherent in BaO lattice itself, but not due to defects in BaO lattice.

Further, we have observed that whenever the BaO film was heated to temperatures above 600°C in vacuum as well as in oxygen gas and then quenched, all the bands in the ultraviolet region vanished out, and it is presumable that this phenomenon is associated with a large change in crystal perfection in the BaO film.

Next, the influence of H_2O vapour upon the absorption bands has been investigated and it has been observed that the change occurred in the bands when the BaO film had been exposed to H_2O vapour at room temperature is fairly similar to the results obtained by us some years ago (**8**).

Lastly, it has been found that no change in the absorption bands in the region of 320 mμ~250 mμ occurs by irradiation of light with wavelengths covering their absorption peaks.

Thus, we are finally led to the conclusion that, in conformity with the results by Tyler and others, the absorption bands of the BaO film in the region of wavelengths between 320 mμ and 250 mμ are due to the production of excitons.

Acknowledgments

The writer wishes to express his cordial thanks to Professor Y. Uchida for his kind guidance throughout the present experiment. The writer's thanks are also due to Drs. K. Fukuda and Y. Nakai for their encouragement.

REFERENCES

1. W. W. Tyler, Optical absorption in barium oxide films. Phys. Rev., **76** (1949), 1887.
2. E. Taft and J. Dickey, Optical absorption edge for BaO as determined by the method of Ives and Briggs. Phys. Rev., **78** (1950), 625.
3. W. W. Tyler and R. E. Sproull, Optical absorption and photoconductivity in barium oxide. Phys. Rev., **83** (1951), 548.
4. L. Apker, E. Taft and J. Dickey, On the photoelectric emission and energy structure of BaO. Phys. Rev., **84** (1951), 508.
5. R. J. Zollweg, Structure in optical absorption of barium oxide films. Phys. Rev., **97** (1955), 288.
6. F. C. Jahoda, Fundamental absorption of barium oxide from its reflectivity spectrum. Phys. Rev., **107** (1957), 1261.
7. A. W. Overhauser, Multiplet structure of excitons in ionic crystals. Phys. Rev., **101** (1956), 1702.
8. K. Takazawa and T. Tomotika, On the optical absorption of thin BaO film in the ultraviolet region. J. Phys. Soc. Japan, **9** (1954), 996.

Memoirs of the College of Science, University of Kyoto, Series A,
Vol. XXIX, No. 1, Article 8, 1958.

ULTRASONIC VELOCITY AND ADIABATIC COMPRESSIBILITY OF MIXTURE OF SULFURIC ACID AND WATER*

BY

Yoshio ISHIDA**

(*Received June 18, 1958*)

1. Introduction

Ultrasonic velocities in various liquid mixtures have been measured by several experimenters. We have carried out a measurement on mixtures of sulfuric acid and water at 5 Mc/sec. After finishing it, the author was informed of Prosorow's result (**1**) and was very glad to have an opportunity to make comparison. In the present research, the ultrasonic velocity in aqueous solution of the sulfuric acid was measured by use of the rotary grating method (**2, 3, 4**) which is a variation of the Debye-Sears light diffraction method (**5**).

The rotary grating method is, in principle, a method to measure, by rotating an optical grating, the distance between diffraction lines which are generated by ultrasonic waves in liquid. It has a higher accuracy than the method to measure directly the diffraction angle.

Moreover, since the present apparatus has not any metallic parts in its sample container, it has become easy to measure ultrasonic velocity in strong acids such as sulfuric acid.

2. Experimental arrangement

The experimental arrangement is shown in Fig. 1. Since a new apparatus has been improved a little as compared with the old one used in the previous research (**4**), a brief description of it will be given here.

A light beam is obtained from a sodium lamp by a collimator having a horizontal slit. It is diffracted doubly by ultrasonic waves in a sample and a rotary grating. The diffraction images generated can be observed by a telescope. In order to observe the diffraction image at its weakest intensity, the plate voltage of power amplifier is made adjustable by means of a slidac. The sample container is provided with a

* Communicated by Professor I. Takahashi. A short account of the present paper was already given in J. Phys. Soc. Japan, **13** (1958), 636.

** Department of Physics, Faculty of Education, Shimane University, Matsue.

water-jacket around it in order to control the temperature of sample liquid. The water from a constant temperature bath flows through the water-jacket and the wave generating tank and enters a reservoir, from which the water is returned again to the constant temperature bath by a circulation pump. The temperature of water in the bath is kept constant by a mercury regulator and a heater. The optical grating is fixed in a cylinder which can be rotated with an angle measuring disk attached, to serve as a rotary grating. The proper constant of the grating is chosen to be 2.000×10^{-3} cm. The circumference of the disk is divided into 360 equal parts, and the angle of rotation can be measured correct to two minutes by an attached vernier.

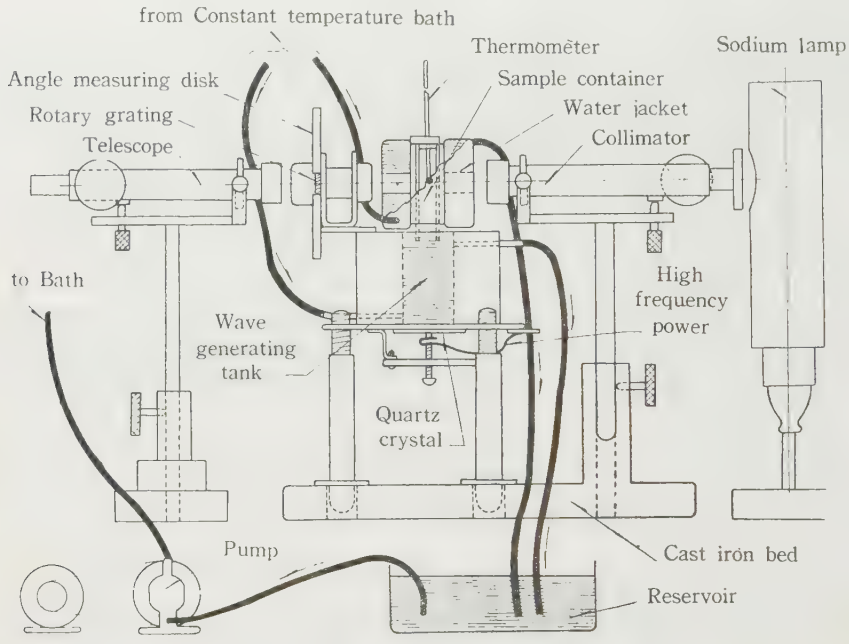

Fig. 1. Experimental arrangement.

3. Method of measuring ultrasonic velocity

Various images seen in the visual field of telescope are shown in Fig. 2. The method of measurement is explained in connection with them. Figure (a) shows an image seen when there are no ultrasonic waves and the lines of rotary grating are perpendicular to the slit. Only the image of slit appears which may be called *the main line*. Figure (b) shows an appearance when the grating is rotated from there. The first order diffraction lines by the grating appear on both sides of the main line and move with the rotation of the grating. They may be called *the rotary main line*.

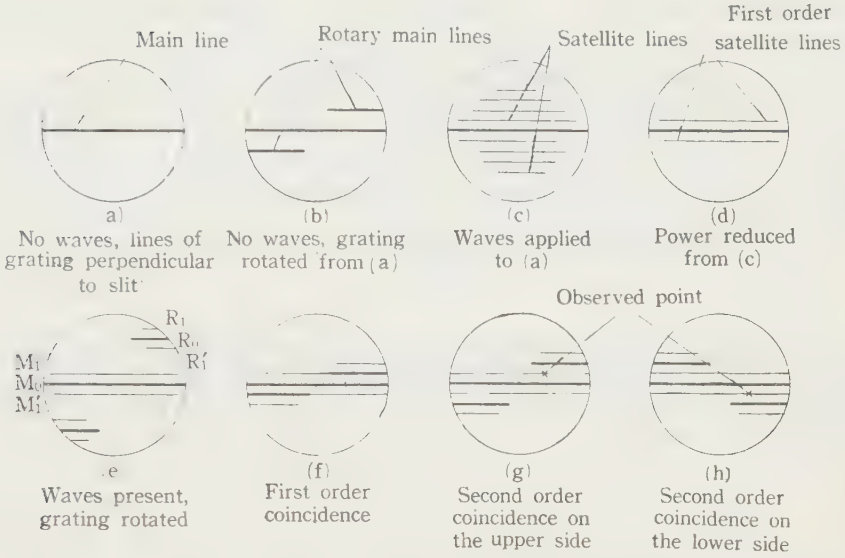

Fig. 2. Diffraction images seen by telescope.

The distance between the main line and the rotary main line becomes maximum when the line of grating is made parallel to the slit. By measuring the distance and the angle of rotation of the grating, it was experimentally ascertained (**1**) that the formula

$$d = \frac{d_0}{\sin\theta} \qquad (1)$$

should hold between the effective constant of the grating d and its proper constant d_0.

When the ultrasonic waves are applied to the state of figure (a), several diffraction lines by the waves appear as shown in figure (c). They may be called *the satellite lines.* Since it is preferable to make measurement with possibly weakest power, the power is reduced to such an extent that only the first order satellite lines remain in the visual field as shown in figure (d). When the grating is rotated from the state of figure (d), the rotary main lines move, being accompanied by their respective first order satellite lines as shown in figure (e). On the way of rotation, the diffraction lines make some coincidence with each other. Figure (f) shows the case in which the rotary main lines coincide with the satellites of the main line. The case may be called *the first order coincidence.* Figure (g) shows the case in which the lower satellite of the rotary main line coincides with the upper satellite of the main line. The case may be called *the second order coincidence on the upper side.* Similarly, figure (h) shows the case of *the second order coincidence on the lower side.* Since the main lines are thick and the satellites fine, it gives more

accurate result to observe the coincidence between satellites themselves than to observe that between the rotary main line and the satellite. Therefore, the second order coincidence was used in the measurement.

Now, if θ_U is the reading of the coincidence angle in figure (g) and θ_L is that in figure (h), $\theta=\frac{1}{2}(\theta_U-\theta_L)$ should serve as θ in the formula (1). Considering that diffraction lines coincide with each other when the wavelength of the ultrasonic wave becomes an integral multiple of the effective constant of the grating d, we obtain

$$\Lambda = nd\,, \tag{2}$$

where Λ is the wavelength of the ultrasonic wave and n a positive integer.

If f is the frequency of the ultrasonic wave, we get, from (1) and (2), the formula for the velocity V as:

$$V = f\Lambda = \frac{nd_0 f}{\sin\theta}\,. \tag{3}$$

In the present case, putting $d_0=2\times10^{-3}$ cm, $f=5\times10^6$ c/s and $n=2$ we obtain

$$V = \frac{200}{\sin\theta}\ [\mathrm{m/sec}]. \tag{4}$$

The error of the measurement is considered as follows. The readings of the coincidence angle are generally different according as the grating is rotated clockwise or counter-clockwise. In figure (e), if

θ_{U1} is the reading when R_1' line approaches M_1 from above and coincides with it,

θ_{U2} the reading when R_1' line approaches M_1 from below and coincides with it,

θ_{L1} the reading when R_1 line approaches M_1' from above and coincides with it,

θ_{L2} the reading when R_1 line approaches M_1' from below and coincides with it,

the required angle readings θ_U, θ_L and θ are obtained by

$$\theta_U = \theta_{U2}+\frac{1}{2}(\theta_{U1}-\theta_{U2}) = \theta_{U2}+\Delta\theta_U\,,$$

$$\theta_L = \theta_{L2}+\frac{1}{2}(\theta_{L1}-\theta_{L2}) = \theta_{L2}+\Delta\theta_L\,,$$

and

$$\theta = \frac{1}{2}(\theta_U-\theta_L) = \frac{1}{2}(\theta_{U2}-\theta_{L2})+\frac{1}{2}(\Delta\theta_U-\Delta\theta_L)\,.$$

Therefore, $\Delta\theta=\frac{1}{2}(|\Delta\theta_U-\Delta\theta_L|)$ is considered as a measure for determining the accuracy of the apparatus.

If we repeat the measurements very many times, $<\Delta\theta_U>$ will become equal to $\Delta\theta_L>$, but $<|\Delta\theta_U-\Delta\theta_L|>$ will take a definite value. An example of the measurements is given below.

Example: Sample:— Distilled water (30°C)

Upper coincidence $\begin{cases}\theta_{U1} & 222^\circ\ 46' \\ \theta_{U2} & 222^\circ\ 34'\end{cases}$

Difference $12' \cdots \Delta\theta_U = 6'$

Lower coincidence $\begin{cases}\theta_{L1} & 207^\circ\ 30' \\ \theta_{L2} & 207^\circ\ 20'\end{cases}$

Difference $10' \cdots \Delta\theta_L = 5'$

and $\theta = 7^\circ\ 38'$.

Calculating with the values of $\Delta\theta_U$, $\Delta\theta_L$ and $|\Delta\theta_U - \Delta\theta_L|$ which were obtained in the series of 967 measurements during the period of the present research, we get

$$<\Delta\theta_U> = 8.31', \quad <\Delta\theta_L> = 7.11' \quad \text{and} \quad <|\Delta\theta_U - \Delta\theta_L|> = 4.54'.$$

Thus, putting $\Delta\theta = \frac{1}{2}<|\Delta\theta_U - \Delta\theta_L|> = 2.27'$ in the error formula:

$$\Delta V \quad \cdot nd_0 f \frac{\cos\theta}{\sin^2\theta} \frac{\pi}{180} \Delta\theta,$$

which can be derived from the formula (3), we get $\Delta V = 2.97$ [m/sec], for the distilled water under consideration.

This error corresponds to the accuracy of about 2/1,000 and may be called *the proper error* of the apparatus. And $<\Delta\theta_U>$, $<\Delta\theta_L>$ may be called *the angular line width*, and $\frac{1}{2}<|\Delta\theta_U - \Delta\theta_L|>$ *the proper error angle*. These values will serve as criterions for the purpose of reducing the error when the apparatus will be improved in a future. It is considered that the angular line width depends principally upon the width of slit, the light intensity, the ultrasonic intensity, etc. And, on the other hand, the proper error angle depends upon the deviation from symmetry of the light and ultrasonic system.

Since the proper error 2/1,000 is a little too large for our purpose of the experiment, the mean value from fifteen measurements was taken as the significant value of the velocity in the sample with a certain concentration and temperature. Therefore, the probable error of the final value was calculated to be ± 0.54 m/sec.

4. Experimental results

1. *Comparison with Prosorow's data*

The ultrasonic velocity in the aqueous solution of the sulfuric acid was measured *versus* concentration. After finishing it, the author was informed of the publication of Prosorow's data. So the author's data are shown in Fig. 3 in comparison with his ones. The concentration is expressed in weight percentage, following Prosorow.

From the curves in Fig. 3, it will readily be seen that in the lower concentration region, both curves coincide fairly well, while in the medium concentration region, the two curves are quite similar, the author's curve lying by about 10 [m/sec] below Prosorow's, and the positions of maxima coincide, situated at 45%. In the higher concentration region, the difference between the two curves becomes larger and ultimately attains the values of 29 [m/sec] at 91%. In this region, however, the

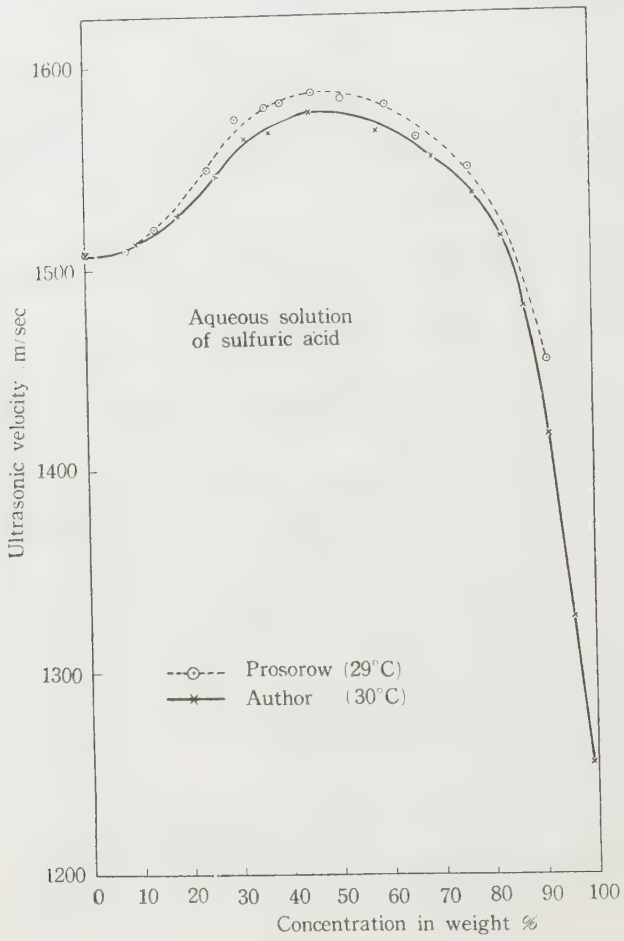

Fig. 3. Comparison with Prosorow's data.

difference of this order of magnitude might be inevitable, since the velocity decreases very rapidly with the increasing concentration—the velocity decrease of 20 [m/sec] corresponding to 1% increase in concentration. The sulfuric acid of the special class was used as a sample, and especially in order to prepare a sample of high concentration of 99.3%, the sulfuric acid was mixed with fuming sulfuric acid.

2. *Velocity and compressibility versus concentration characteristics at two temperatures*

The author measured the ultrasonic velocity *versus* concentration at two different temperatures. The results, together with the adiabatic compressibility calculated from them, are shown in Fig. 4. The concentration is expressed in this case in mole fraction of sulfuric acid which is considered to be more convenient for the consideration of the molecular structure of the liquid than in weight percentage. To get the value of concentration, the normality of the solution is measured by acidimetry. It is possible to obtain from tables the values of density of the solution at 15°C and 30°C corresponding to the values of normality at which measurements were done. We can calculate the mole fraction of the sulfuric acid from the normality and the density. The adiabatic compressibility can be computed by $1/\rho V^2$, where V is the measured velocity and ρ the density.

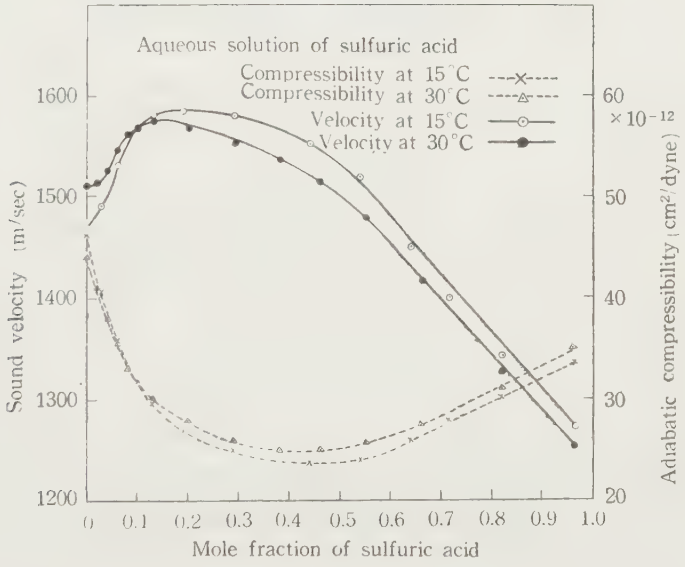

Fig. 4. Velocity and compressibility *versus* concentration, with temperature as parameter.

From Fig. 4 it will readily be seen that the velocity-curves have maxima, while the compressibility-curves minima. The position of maximum of the velocity-curve shifts to the higher concentration as the temperature decreases. The position of minimum of the compressibility curve does not shift appreciably, but the value of minimum decreases with the temperature. The results will be discussed in the next section.

3. *Velocity-temperature characteristic at several concentrations*

The ultrasonic velocity in the solution was measured in the temperature range covering from 6°C to 46°C, with concentration as parameter. The result is shown in Fig. 5. In the higher concentration, the curves become straight with negative gradient. From the straight lines V, VI and VII, the velocity-temperature coefficient is calculated to be −1.61m/sec/deg at 0.437 mf, −1.53 m/sec/deg at 0.715 mf,

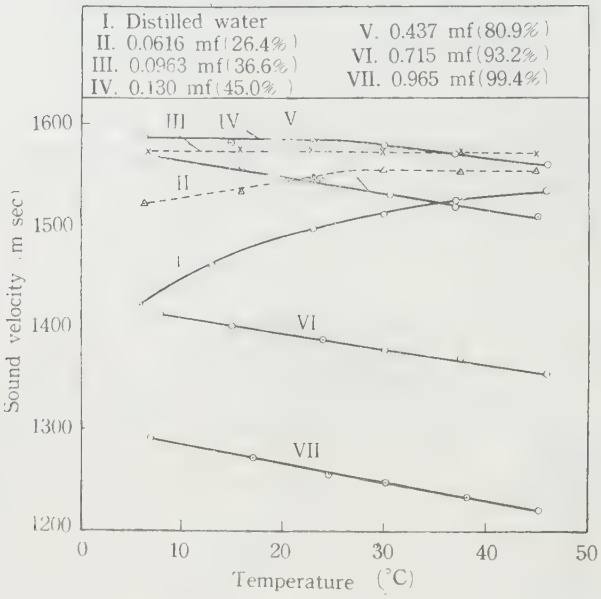

Fig. 5. Velocity *versus* temperature, with concentration as parameter.

and −1.80 m/sec/deg at 0.965 mf. It should be noted that as seen from the straight line III, the velocity is independent of the temperature at the concentration of 0.0963 mf. The curve I is the characteristic of the distilled water which is measured for comparison and found to be parabolic as known already. The discussion about the results will be given in the next section.

5. Discussion

1. *Regarding the compressibility-concentration characteristic*

The phenomenon that the velocity-curve has maximum as shown in Fig. 4 is common to all of the mixtures of methyl alcohol–water (**6**), ethyl alcohol–water (**7**), acetone–water (**7**), pyridine–water (**6**), formic acid–water (**8**), acetic acid–water (**6**, **9**), nitric acid–water (**1**), carbon tetrachloride–liquid paraffin (**10**) and others. We ascertained as shown in Table I that the volume contraction always takes place when these mixtures are prepared, including the mixture of sulfuric acid and water.

Table I. Index of volume contraction and heat of dilution in liquid mixture.

Mixture	Index of volume contraction		Heat of dilution	
	t°C	$-\Delta V/V\times 100$*	t°C	Q**
Methyl alcohol–Water	10.0	4.00	10	8.38
Ethyl alcohol–Water	12.0	4.52	13	10.63
Aceton–Water	14.5	3.92	10	10.50
Pyridine–Water	11.0	2.40	22	8.87
Formic acid–Water	12.0	2.26	7	0.33
Acetic acid–Water	9.0	2.68	23	1.00
Nitric acid–Water	12.0	3.26	—	—
Sulfuric acid–Water	30.0	7.60	—	—
Carbon tetrachloride–Liquid paraffin	12.0	3.20	—	—

* ΔV is the volume contraction when component liquids are mixed in equal volumes. V is the sum of volumes of component liquids.

** When water is considered as solvent, Q is expressed in kilo-joules per mole solute at infinite dilution (*International Critical Tables*, Vol. 5, p. 148).

Therefore, there exists a relation between the volume contraction and the existence of maximum in the velocity-curve and of minimum in the compressibility-curve. Ernst (**10**) has pointed out that the solutions which show this characteristic do not obey Raoult's law. We want to examine the idea more closely. The solutions which do obey Raoult's law are the so-called ideal solutions and they have no heat of dilution and there is no volume change when the components are mixed in liquid state. The pairs of liquids listed in Table I are all considered to make non-ideal solutions, as they have heat of dilution* and there occur volume changes when mixed.

It is well known that there are two types of non-ideal solution in connection with the deviation from Raoult's law. One is a positive deviation type as shown in Fig. 6 (a)**. This is the case when the escaping tendency of A molecules is increased by the presence of B molecules, since the attraction between B molecules is much greater than that between A molecules. The other is a negative deviation type as shown in Fig. 6 (b)**. The case occurs when there exists the strong attraction between A and B molecules. In both figures, dotted-line curves show ideal behaviors.

When we observe the compressibility characteristic of the non-ideal solutions cited above, keeping the theory in mind, we become aware of a similarity between both characteristics of compressibility and total vapor pressure. It is certain that the

* The approvable data of heat of dilution concerning the last three mixtures in Table I could not be found. But its existence is evident from our simple experiences.

** These figures are quoted from: S. Glasstone: *Elements of Physical Chemistry* (1954), p. 356.

existence of the compressibility minimum which is, more generally, the negative deviation from the ideal behavior, comes from the attraction between the component molecules. Therefore, they are expected also to show the negative deviation from Raoult's law.

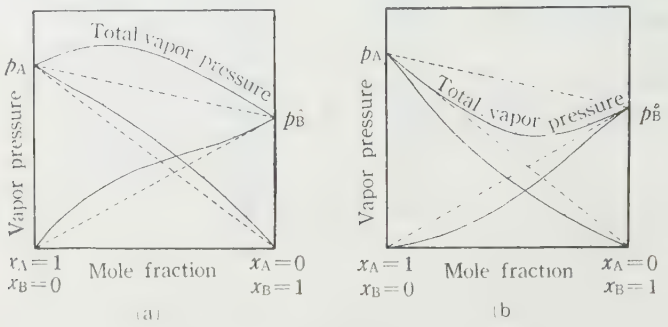

Fig. 6. Total vapor pressure *versus* concentration of non-ideal solutions.

In the case of the aqueous solution of sulfuric acid, the hydronium ion $(H_3O)^+$ and sulfuric acid ion $(SO_4)^{--}$ produced when the acid dissociates in water, compress the water molecules by their electrostatic attraction and reduce the compressibility of the solution. On the other hand, the curves of total vapor pressure *versus* concentration shown in Fig. 7*, indicate negative deviations from their ideal behaviors.

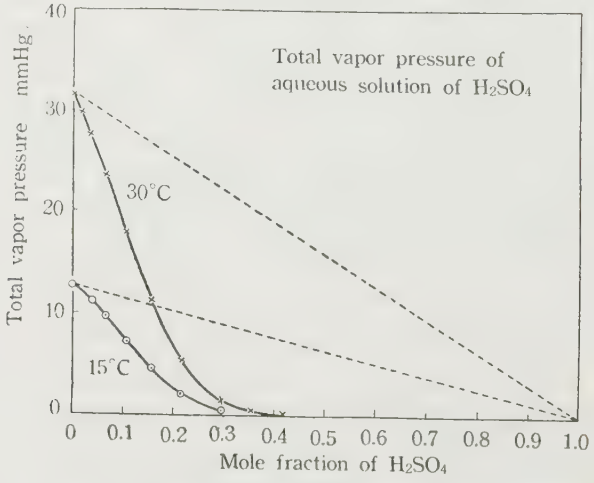

Fig. 7. Total vapor pressure *versus* concentration of aqueous solution of H_2SO_4.

* This figure was drawn from the data given in *International Critical Tables*, Vol. 3 (McGraw-Hill, 1928).

In a special case when one component is water in non-ideal solution, the problem becomes more complicated on account of the abnormality of water. If we seek the cause for negative deviation of compressibility of aqueous solution of sulfuric acid only in the intermolecular forces, including ionic attraction, it might be natural that the curves corresponding to two temperatures shift parallel to each other. And, since the compressibility is reduced at the lower temperature on account of the increase in intermolecular force, the entire curve at 15°C would lie below the curve at 30°C. But, in fact, both curves intersect in the neighborhood of the concentration of 0.1 mf and the curve at 15°C rises above the curve at 30°C within the concentration of less than 0.1 mf, as already seen in Fig. 4.

The fact can be explained by the association of water molecules. That the compressibility of pure water at 15°C is greater than that at 30°C is accounted for by the fact that the degree of association of water molecules is larger at the lower temperature. And the compressibility of the solution falls rapidly on account of the depolymerization of water molecules by the sulfuric acid added.

Hereupon, we must assume both the intermolecular forces and the depolymerization of water molecules to be causes for decrease in the compressibility in the lower concentration region. We try to evaluate the respective degree of contributions of these two to the decrease in the compressibility.

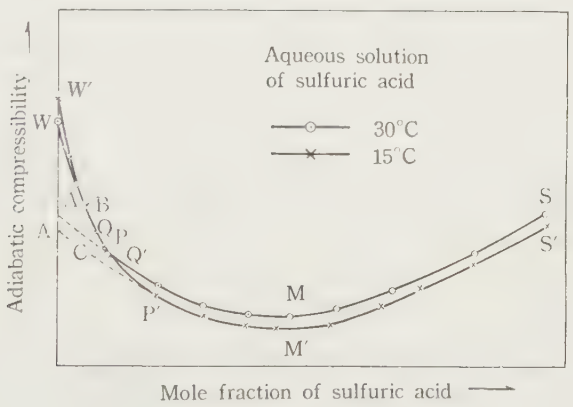

Fig. 8. Extrapolation of compressibility *versus* concentration curves.

The compressibility-curves have large gradients at the concentration lower than 0.1 mf. We extrapolate naturally the parts of the curves higher than 0.1 mf and obtain the curves SMPA, S′M′P′A′ shown in Fig. 8. The curves are considered to show the negative deviation originating from the intermolecular force. Therefore, if water would be a non-associated liquid, the points A and A′ might give the values

of compressibility of pure water at 30°C and 15°C respectively. Accordingly, the lowering of compressibility by the depolymerization can be estimated to be

$$WA = 9\times10^{-12}\ [cm^2/dyne] \quad \text{at} \quad 30°C,$$

and

$$W'A' = 13\times10^{-12}\ [cm^2/dyne] \quad \text{at} \quad 15°C.$$

Next, we will determine the concentration at which the association of water molecules are completely broken by the sulfuric acid added. In order to get the value at 30°C, we draw in Fig. 8 a straight line parallel to the abscissa from point A as far as point B at which it intersects the curve WPM, and then draw a straight line parallel to the ordinate from B till point C at which it intersects the curve APM, and finally, draw a straight line parallel to the abscissa from C till point Q at which it intersects the curve WPM again. The concentration of 0.085 mf corresponding to the point Q is the desired one, because at the point B which corresponds to the decrease WA, the decrease BC by the effect of intermolecular force must be added and the point Q which corresponds to the sum CW should be a desired point. Similarly, we get the concentration of 0.11 mf which corresponds to the point Q'.

There are two evidences as given below which support the deduction that the association of water molecules in aqueous solution of sulfuric acid is completely broken up to the concentration of 0.085 mf at 30°C and up to 0.11 mf at 15°C.

The first evidence: The velocity-temperature characteristic shown in Fig. 5 can be rewritten into the compressibility-temperature characteristic shown in Fig. 9. In this figure, the straight line III at the concentration of 0.0963 mf shows that the compressibility increases with temperature. In almost all liquids except water, it is known that the compressibility increases with temperature. The feature shows that the liquid is non-associated. Therefore, it can be deduced that the association of water molecules has been broken by the sulfuric acid added until the concentration becomes 0.0963 mf.

The second evidence: Studies on ice (**11**) show that the associated water molecules form tetrahedra, each molecule having four neighbors, and such tetrahedra connected form lattice. In water, the X-ray measurements offer the strong evidence in favor of widespread local tetrahedral arrangement at room temperature and below. On the other hand, at the concentration of 0.1 mf which is approximately the mean of 0.085 mf and 0.11 mf, the ratio of water molecules to H_2SO_4 molecules is 9 : 1. Since a molecule of H_2SO_4 emits two protons, the ratio of H_2O molecules to protons is 9 : 2. As the mechanism by which the association of water molecules is broken, we assume that when a proton from sulfuric acid catches a water molecule to form a hydronium ion $(H_3O)^+$, the associated group is broken down to sub-groups or to

isolated molecules. From the above ratio, the number of water molecules assigned to a proton is 4.5. Since the minimum size of regular group of associated molecules is considered to be a tetrahedron consisting of five molecules, there exist almost sufficient protons to destroy all groups of associated molecules at the concentration of 0.1 mf.

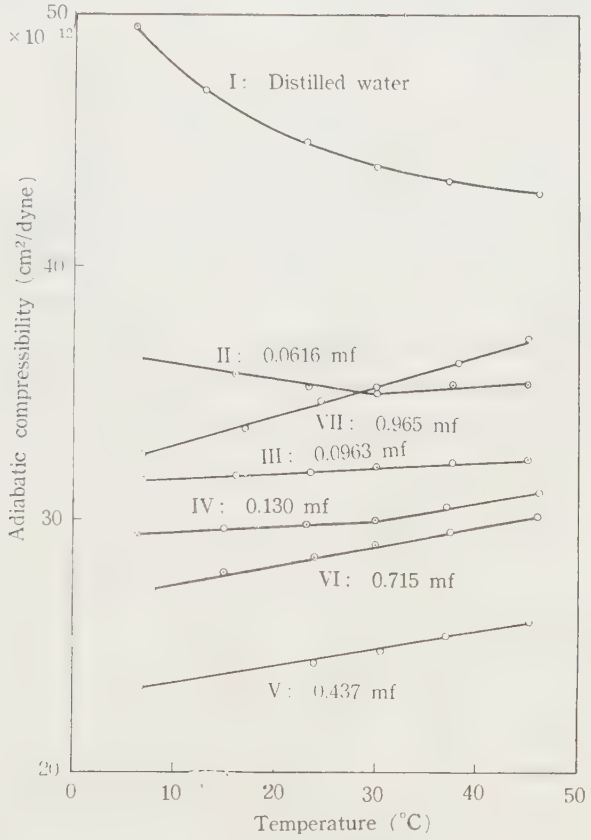

Fig. 9. Compressibility *versus* temperature, with concentration as parameter.

2. *Regarding the compressibility-temperature characteristic*

The characteristics are shown in Fig. 9. The curve I shows that the compressibility of the distilled water falls with temperature. This is a well-known fact. On the contrary, the compressibility of the aqueous solution of sulfuric acid of higher concentration rises almost linearly with temperature, as known from straight lines V, VI, VII. The aqueous solution is said to be a normal liquid. Water is an abnormal liquid. The abnormality rises from the association of the molecules. An interesting fact is seen in curve II. The curve consists of two straight lines, one of which has a negative gradient below the temperature 30°C and the other has a positive gradient

above 30°C. The part of negative gradient means that the association of water molecules remains, while the part of positive gradient means that association has vanished, that is, 30°C is a critical temperature of the solution of the concentration of 0.0616 mf. As already mentioned, all of the associations are considered to be destroyed in the solution of concentration of 0.0963 mf, as known from the positive gradient of the straight line III.

3. *Regarding the pattern of the velocity-temperature curves*

Returning to Fig. 5, we want to point out a feature which can be seen in the family of curves. Since the curve III is a straight line parallel to the abscissa, the curve II a combination of a straight line parallel to the abscissa and a straight line of positive gradient, and the curve IV a combination of a straight line parallel to the abscissa and a straight line of negative gradient, the hypothetical velocity-temperature curves shown in Fig. 10 occurs to us. If the measurement would be done in the wider temperature range, the curve III would be a straight line of negative gradient in the higher temperature, and a straight line of positive gradient in the lower temperature, and it would become trapezoidal as a whole. All of the

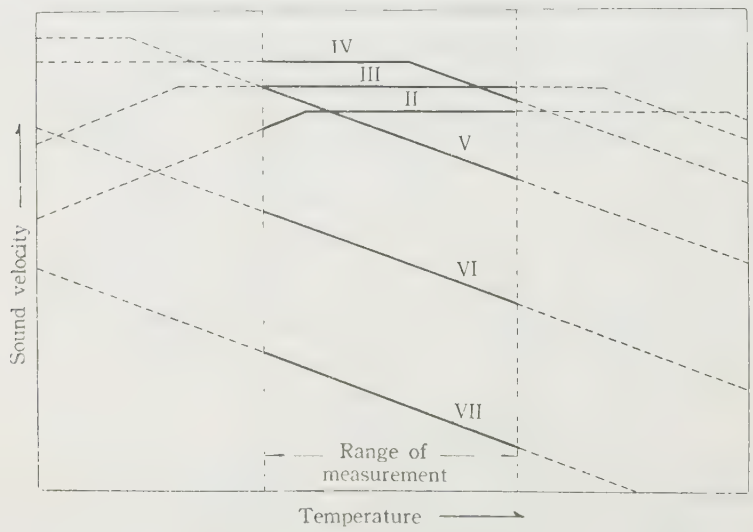

Fig. 10. Hypothetical velocity *versus* temperature curves.

straight lines which appear in Fig. 5 are imagined to be parts of a trapezoid which is the hypothetical entire curve. And it is seen that the trapezoid shifts to the lower temperature as the concentration increases. Willard (**12**) has stated that such a hypothetical velocity-temperature curve is parabolic in the mixtures of water–ethanol and of water–other organic liquids. But, by the author's measurement, the curve is trapezoidal but not parabolic in the mixture of sulfuric acid and water.

6. Acknowledgement

Having been supported by a scholarship of the Ministry of Education in 1957, the present research was performed in Department of Physics, Faculty of Science, Kyoto University. The author wishes to thank Professor I. Takahashi for his continual encouragement and valuable discussions. His thanks are also due to Professor M. Ishibashi and Mr. Y. Yamamoto of the same university for their kind guidance in the technique of acidimetry.

REFERENCES

1. P. Prosorow: Zh. Fiz. Kim. **14** (1940), 391. (See B. B. Kudrjawzew: *Anwendung von Ultraschallverfahren bei Physikalisch-Chemischen Untersuchungen*, (Deutscher Verlag der Wissenschaften, Berlin, 1955, translated from the Russian edition (1952)).
2. I. Takahashi, Y. Ishida and M. Ota: Mem. Coll. Sci. Univ. Kyoto, A **27** (1953), 41.
3. I. Takahashi and Y. Ishida: J. Appl. Phys. Japan, **25** (1956), 247 (in Japanese).
4. Y. Ishida: Sci. Report, Shimane Univ., **7** (1957), 30.
5. P. Debye and F. W. Sears: Proc. Nat. Acad. Sci., **18** (1932), 409.
6. I. G. Mikhailov: C. R. (Doklady) URSS **31** (1941), 324.
7. I. G. Mikhailov: *Ibid.* **26** (1940), 147.
8. I. G. Mikhailov: *Ibid.* **31** (1941), 550. (Concerning the last three, see O. Nomoto: *Chôonpa*, (Kawade-Shobô, Tokyo, 1948)).
9. A. W. Smith and L.M. Ewing: J. Chem. Phys., **7** (1939), 632.
10. P. J. Ernst: J. Acous. Soc. America, **19** (1947), 372.
11. R. W. Gurney: *Ionic Processes in Solutions*, (McGraw-Hill) p. 48.
12. G. W. Willard: J. Acous. Soc. America, **19** (1947), 235.

CONTENTS

On the Periods of Seismic Waves observed in Local Earthquakes.

By *T. Mikumo* 1

On the Seismic Waves reflected at the Mohorovičić Discontinuity (II).

By *A. Kamitsuki* 19

On the Materials in the Earth's Mantle.

By *T. Nishitake* 37

Elasticity of Solids at High Pressure and the Earth's Mantle.

By *T. Nishitake* 47

Precise Measurement of Frequency Shift of Ammonia Inversion Spectrum.

By *M. Yamano* 57

Center Frequency of Ammonia Inversion Spectrum in Low Pressure Region.

By *M. Yamano* 67

On the Influence of Oxygen Gas upon the Optical Absorption Bands of Evaporated Barium Oxides in the Ultraviolet Region.

By *T. Tomotika* 75

Ultrasonic Velocity and Adiabatic Compressibility of Mixture of Sulfuric Acid and Water.

By *Y. Ishida* 91

Printed by NIPPON INSATSU SHUPPAN

Fukushima, Osaka

7 MAY 1959